# A Closely Coupled Experimental and Numerical Approach for Hypersonic and High Enthalpy Flow Investigations Utilising the HEG Shock Tunnel and the DLR TAU Code

**Klaus Hannemann, Jan Martinez Schramm, Alexander Wagner,**

**Sebastian Karl, Volker Hannemann**

German Aerospace Center, DLR
Institute of Aerodynamics and Flow Technology, Spacecraft Department
37073 Göttingen, Bunsenstraße 10, Germany

Klaus.Hannemann@dlr.de, Jan.Martinez@dlr.de, Alexander.Wagner@dlr.de,
Sebastian.Karl@dlr.de, Volker.Hannemann@dlr.de

## *ABSTRACT*

*The High Enthalpy Shock Tunnel Göttingen (HEG) of the German Aerospace Center (DLR) is one of the major European hypersonic test facilities. It was commissioned for use in 1991 and was utilised since then extensively in a large number of national and international space and hypersonic flight projects. Originally, the facility was designed for the investigation of the influence of high temperature effects such as chemical and thermal relaxation on the aerothermodynamics of entry or re-entry space vehicles. Over the last years its range of operating conditions was subsequently extended. In this framework the main emphasis was to generate test section conditions which allow investigating the flow past hypersonic flight configuration from low altitude Mach 6 up to Mach 10 in approximately 33 km altitude. The studies performed focused on the external as well as internal aerodynamics including combustion of hydrogen in complete supersonic combustion ramjet configurations. The complexity of these flows requires that experiments in ground based facilities are strongly linked with computational fluid dynamics (CFD) investigations. These common activities range from the calibration process of the facility and the study of basic aerodynamic configurations, which are well suited to look at fundamental aspects of high enthalpy flow fields, to the investigation of complex re-entry configurations. In the DLR Spacecraft Department the research programs conducted in HEG are closely linked with numerical studies using the DLR TAU code.*

## 1.0 INTRODUCTION

In hypersonics, the high cost and risk of designing complex vehicles precludes extensive experimental prototype flight testing. Therefore, ground based testing facilities were developed and they played an important role since the early era of hypersonic flight. Later, as computing resources became more advanced, computational fluid dynamics (CFD) tools were developed and utilised. Recent approaches undertaken in the framework of projects such as HyShot [66] or SHEFEX [52] show that coupling of the three main tools of hypersonic flight vehicle design, namely hypersonic ground based testing, CFD and flight testing, are becoming economically achievable (Figure 1). The means to arrive at this goal is to perform hypersonic flight tests of new technologies based on sounding rocket technology which can be realized with an order of magnitude lower budget compared to flying complex X-vehicles. This development will lead in the near future to more frequent flight tests.

The objectives of the present article is the discussion of the closely coupled experimental and numerical approach for hypersonic and high enthalpy flow investigations utilising the DLR High Enthalpy Shock Tunnel Göttingen, HEG and the DLR TAU Code. While flight testing is the ultimate goal and required to close the loop shown in Figure 1, it is only briefly addressed here.

# Report Documentation Page

*Form Approved*
*OMB No. 0704-0188*



| 1. REPORT DATE | 2. REPORT TYPE | 3. DATES COVERED |
|---|---|---|
| **APR 2010** | **N/A** | **-** |

4. TITLE AND SUBTITLE
**A Closely Coupled Experimental and Numerical Approach for Hypersonic and High Enthalpy Flow Investigations Utilising the HEG Shock Tunnel and the DLR TAU Code**

5a. CONTRACT NUMBER
5b. GRANT NUMBER
5c. PROGRAM ELEMENT NUMBER

6. AUTHOR(S)

5d. PROJECT NUMBER
5e. TASK NUMBER
5f. WORK UNIT NUMBER

7. PERFORMING ORGANIZATION NAME(S) AND ADDRESS(ES)
**German Aerospace Center, DLR Institute of Aerodynamics and Flow Technology, Spacecraft Department 37073 Göttingen, Bunsenstraße 10, Germany**

8. PERFORMING ORGANIZATION REPORT NUMBER

9. SPONSORING/MONITORING AGENCY NAME(S) AND ADDRESS(ES)

10. SPONSOR/MONITOR'S ACRONYM(S)
11. SPONSOR/MONITOR'S REPORT NUMBER(S)

12. DISTRIBUTION/AVAILABILITY STATEMENT
**Approved for public release, distribution unlimited**

13. SUPPLEMENTARY NOTES
**See also ADA569031. Aerothermodynamic Design, Review on Ground Testing and CFD (Conception aerothermodynamique, revue sur les essais au sol et dynamique des fluides informatisee).**

14. ABSTRACT
**The High Enthalpy Shock Tunnel Göttingen (HEG) of the German Aerospace Center (DLR) is one of the major European hypersonic test facilities. It was commissioned for use in 1991 and was utilised since then extensively in a large number of national and international space and hypersonic flight projects. Originally, the facility was designed for the investigation of the influence of high temperature effects such as chemical and thermal relaxation on the aerothermodynamics of entry or re-entry space vehicles. Over the last years its range of operating conditions was subsequently extended. In this framework the main emphasis was to generate test section conditions which allow investigating the flow past hypersonic flight configuration from low altitude Mach 6 up to Mach 10 in approximately 33 km altitude. The studies performed focused on the external as well as internal aerodynamics including combustion of hydrogen in complete supersonic combustion ramjet configurations. The complexity of these flows requires that experiments in ground based facilities are strongly linked with computational fluid dynamics (CFD) investigations. These common activities range from the calibration process of the facility and the study of basic aerodynamic configurations, which are well suited to look at fundamental aspects of high enthalpy flow fields, to the investigation of complex re-entry configurations. In the DLR Spacecraft Department the research programs conducted in HEG are closely linked with numerical studies using the DLR TAU code.**

15. SUBJECT TERMS

| 16. SECURITY CLASSIFICATION OF: | | | 17. LIMITATION OF ABSTRACT | 18. NUMBER OF PAGES | 19a. NAME OF RESPONSIBLE PERSON |
|---|---|---|---|---|---|
| a. REPORT<br>**unclassified** | b. ABSTRACT<br>**unclassified** | c. THIS PAGE<br>**unclassified** | **SAR** | **66** | |

**Standard Form 298 (Rev. 8-98)**
Prescribed by ANSI Std Z39-18

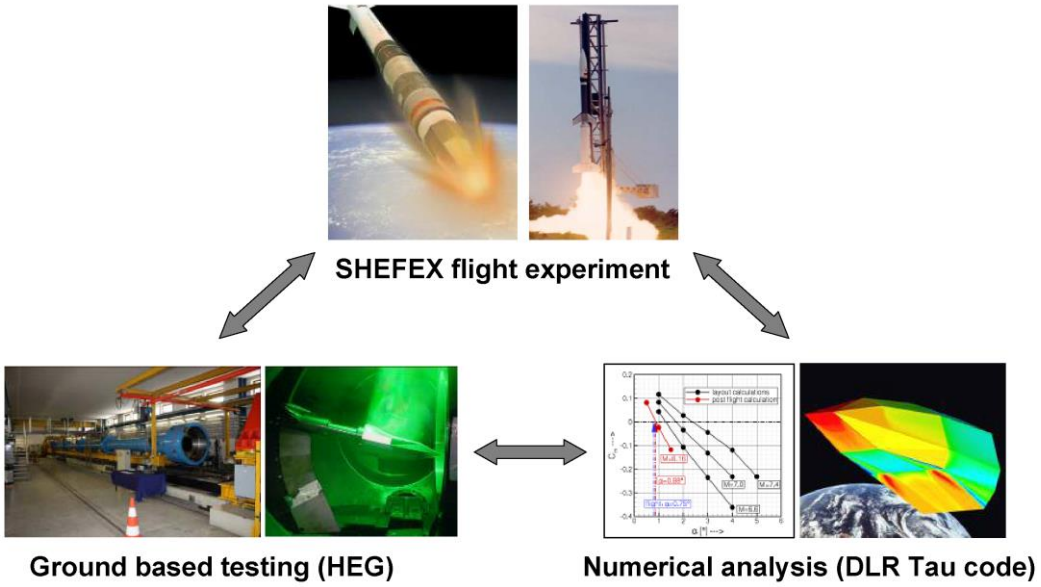


**Figure 1: Three major sources of aerothermodynamic data – ground based testing, numerical analysis and flight experiment**

The article is structured such that after a description of the HEG facility (chapter 2) and the applied measurement techniques (chapter 3), the DLR TAU code is presented in chapter 4. Finally in chapter 5, examples of combined experimental and numerical flow field investigations are presented. These comprise the calibration of the HEG free stream flow, high enthalpy cylinder shock layer investigations, free jet testing and CFD analysis of the HyShot II scramjet flight experiment and the HEG post flight analysis of the DLR SHEFEX-I flight experiment.

# 2.0 EXPERIMENTAL TOOLS

## 2.1 Hypersonic and High Enthalpy Ground Based Testing

In hypervelocity flows the speed of the considered fluid is much larger than the speed of sound. Commonly the hypersonic flow regime is considered to start above a Mach number of M=5. Ground based testing of such flows is performed in many different types of facilities. The reason for this is the large range of flow conditions and phenomena encountered in hypersonic flight and the fact that no single facility can simulate all relevant flow parameters simultaneously. Therefore, in hypersonic testing, partial simulation of different flow phenomena is performed in different types of facilities. Examples are Mach-Reynolds number simulations in cold hypersonic ground based test facilities, verification and qualification of hot structures of space vehicles in arc-heated test facilities or the investigation of the influence of the chemically reacting flow past an entry or re-entry vehicle on its aerodynamic behaviour in shock tunnels or shock expansion tunnels. Comprehensive overviews of ground based testing of hypersonic flows are given by e.g. Lukasiewicz [50] and Lu & Marren [49].

One possibility to increase the Mach number in ground based facilities is by reducing the free stream temperature, i.e. the free stream speed of sound. In this case, high Mach numbers can be achieved while the free stream velocity is significantly lower than the actual flight velocity. However, characteristic of high Mach number hypersonic flight with M ≈10 and higher is that the kinetic energy of the flow is large enough that high temperature effects such as vibrational excitation or dissociation of the fluid molecules occur in the flow past hypersonic vehicles. The high flow velocities and subsequently the high temperature

effects are not duplicated in cold hypersonic ground based test facilities. During the re-entry flight of a space vehicle in the earth's atmosphere or during the interplanetary atmospheric entry of space vehicles or meteorites, speeds in excess of 6 km/s are achieved. Considering a flow with this speed in a wind tunnel test section with an area of 1 $m^2$ and a density of 0.003 $kg/m^3$, a power requirement of already 300 MW results. Therefore, continuous flow facilities are not a practical way to generate such high enthalpy, hypersonic flows. Additionally, the correct simulation in ground based testing of the chemical relaxation length of the dissociation reactions of the fluid molecules occurring for example behind the strong bow shock in front of the nose of a re-entry vehicle, requires the duplication of the flight binary scaling parameter, the product of the free stream density $\rho$ times a characteristic flow length L (see e.g. Stalker [85]). Consequently, the smaller the scale of the wind tunnel model is chosen, the higher the free stream density or pressure needs to be. Considering the flight trajectory range of a re-entry vehicle in about 70 km altitude, where typically the highest heat flux occurs, the atmospheric density is approximately $10^{-4}$ $kg/m^3$. Using a geometrical scaling factor of 30, a free stream density in the ground based facility of 0.003 $kg/m^3$ is required. If a flow with this free stream density and a velocity of 6 km/s is generated by expansion in a convergent / divergent hypersonic nozzle from a reservoir at rest without adding energy, a total specific enthalpy of about 23 MJ/kg and a nozzle reservoir pressure in the order of 90 MPa is required. This results in a nozzle reservoir temperature of about 10000 K. It is clear that such conditions can only be achieved in impulse facilities with short flow duration. The most successful facility types which are able to generate high enthalpy and high pressure hypersonic flows are shock tunnels and shock expansion tunnels with typical test times of approximately 5 milliseconds and less. It should be emphasised here that the test time scales with the size of the facility. The number quoted here is typical for facilities with shock tube diameters in the order of 100 – 200 mm and nozzle exit diameters of less than approximately 1 m. The principle of these facilities is to store the energy over a long period of time, therefore reducing the necessary power requirement and subsequently releasing the stored energy rapidly. Due to the high flow speeds, test times in the order of a few milliseconds are still sufficient for the development of a steady flow over a model. According to Hornung [38], a reasonable, conservative correlation of the necessary test time to establish a steady flow is $\tau = 20\ L/u_\infty$, where L is the model length and $u_\infty$ is the free stream velocity. For a test using the above mentioned flow condition and a 0.3 m long wind tunnel model, the required test time would be 1 ms. The high pressure, high velocity flows which can be generated in shock tunnels and shock expansion tunnels makes these facilities not only suitable for the investigation of space vehicle aerothermodynamics but also for studying complete airbreathing propulsion systems, particularly supersonic combustion ramjets (scramjets) at flight Mach numbers of M = 8 and above. In this framework it is important that in addition to the free stream Mach and Reynolds number, the correct static pressure and temperature are established at the combustor inflow. Further, if hypersonic flight configurations are considered which can be tested at 1:1 scale, the flight free stream conditions can be duplicated in these facilities generating the same pressure and similar heat flux loads as experienced in flight. In the subsequent sections, the operating conditions realised in the High Enthalpy Shock Tunnel Göttingen, HEG will be presented.

## 2.2 High Enthalpy Shock Tunnel Göttingen, HEG

The HEG is a free piston driven shock tunnel ([28], [32]) which was developed and constructed in the framework of the European HERMES program over the period 1989 – 1991. It was commissioned for use in 1991, at that time being the largest facility of its type worldwide. Since then it was extensively used in a large number of national and international space and hypersonic flight projects. The research activities which were always strongly linked with CFD investigations range from the calibration process of the facility and the study of basic aerodynamic configurations, which are well suited to investigate fundamental aspects of high enthalpy flows to the investigation of complex entry, re-entry, hypersonic flight and integrated scramjet configurations.

In a free piston driven shock tunnel, the conventional driver of a shock tunnel is replaced by a free piston driver. This concept was proposed by Stalker [84]. A schematic and wave diagram of this type of facility is shown in Figure 2.

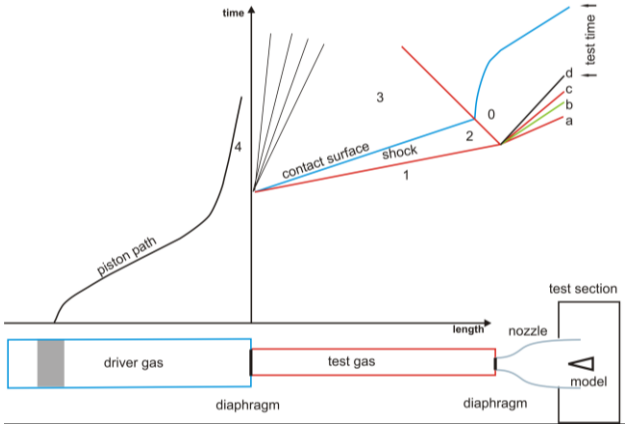


**Figure 2: Schematic and wave (x-t) diagram of a free piston driven shock tunnel**

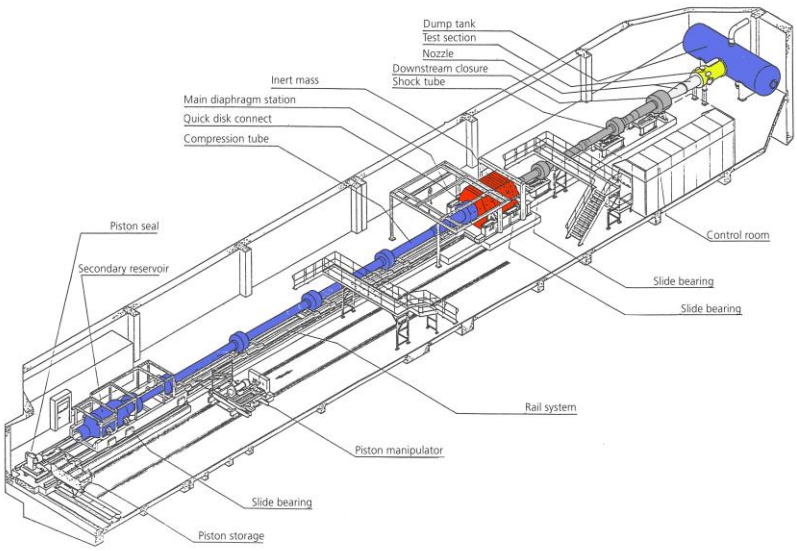


**Figure 3: Schematic of the High Enthalpy Shock Tunnel Göttingen, HEG**

Free piston driven shock tunnels consist of a secondary reservoir, a compression tube, separated from an adjoining shock tube via the primary diaphragm, and a subsequent nozzle, test section and dump tank. A schematic and photos of HEG are given in Figure 3 and Figure 4, respectively.

The high pressure air stored in the secondary reservoir is utilised to accelerate a heavy piston down the compression tube. During this quasi-adiabatic compression and heating of the light driver gas (typically helium or a helium argon mixture), the piston reaches a maximum velocity in the order of 300 m/s. The driver gas temperature increases with the driver gas volumetric compression ratio. When the main diaphragm burst pressure is reached it ruptures and the wave process as in a conventional reflected shock tunnel is initiated (see Figure 2). A shock wave is moving into the driven section and the head of a centred

expansion wave is moving into the high pressure region. The numbers used in Figure 2 denote distinct regions of the flow. Region 1 contains the test gas at the initial shock tube filling conditions and region 4 contains the hot, compressed driver gas after piston compression. Region 2 contains the shock compressed test gas, while in region 3, the driver gas processed by the unsteady expansion wave is contained. The test and driver gas are separated by a contact surface.

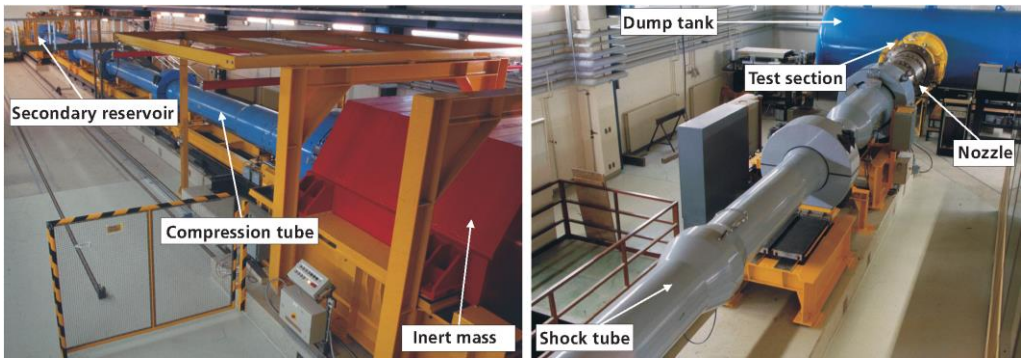


**Figure 4: Photographic views of the High Enthalpy Shock Tunnel Göttingen, HEG**

After reflection of the incident shock wave at the right end wall of the shock tube, the test gas is brought to rest in region 0. Subsequently, the reflected shock wave penetrates the contact surface. Depending on the local conditions, three types of shock wave / contact surface interaction can be differentiated. Due to the fact that the shock compressed and heated slug of gas in region 0 is used in reflected shock tunnel operation as the reservoir driving the flow in the nozzle and test section, shock tube operation in tailored interface mode is most desirable (Figure 5). At this condition the pressure in region 0 remains constant.

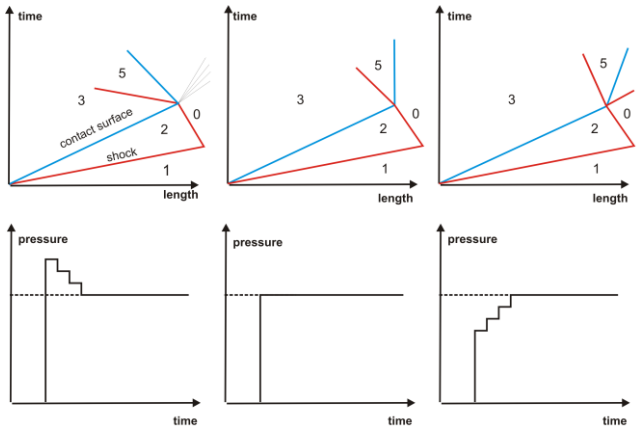


**Figure 5: Shock wave / contact surface interactions for undertailored (left), tailored (middle) and overtailored (right) interface condition; wave (x-t) diagram (upper row) and time history of pressure in region 0 (lower row)**

For undertailored or overtailored interface conditions, the pressure in region 0 is decreasing or increasing, respectively after interaction of the reflected shock with the contact surface (Figure 5). Reflected shock tunnels are characterised by a convergent - divergent nozzle which is attached to the end of the shock tube. A thin secondary diaphragm is placed at the nozzle entrance in order to allow evacuation of the nozzle, test section and dump tank before the run. The nozzle entrance diameter is chosen sufficiently small such that the incident shock wave is almost completely reflected. The stagnant slug of test gas, generated by the shock reflection in region 0 is subsequently expanded through the hypersonic nozzle. The nozzle flow

starting process is characterised by a wave system which passes through the nozzle before a steady flow is established (see Figure 2). The incident shock wave (a) is followed by a contact surface (b), an upstream facing secondary shock wave (c) and the upstream head of an unsteady expansion (d). The trajectory of the piston is chosen in a way that after main diaphragm rupture, the pressure and temperature of the driver gas in region 4 is maintained approximately constant. This is achieved by selecting the velocity of the piston at diaphragm rupture, and therefore the subsequent movement of the piston such that it compensates for the loss of the driver gas flowing into the shock tube. For that reason, in contrast to the constant volume driver of conventional shock tunnels, the free piston driver is a constant pressure driver. Due to the large forces occurring during the operation of the free piston driver, the compression tube, shock tube, nozzle assembly is allowed to move freely in axial direction. An inert mass placed at the compression tube / shock tube junction can significantly reduce the recoil motion of the facility during operation. The test section and the dump tank remain stationary. A sliding seal is used at the nozzle / test section interface.

The overall length of HEG is 62 m and it weighs 280 t. Approximately a third of its weight is contributed by the inert mass (see Figure 3 and left picture of Figure 4). The compression tube is closed by a hydraulic oil system (quick disk connect) at the main diaphragm station. The shock tube is connected to the nozzle of the tunnel at the downstream closure, which is also driven by oil hydraulics to close and seal the tunnel. The compression tube has a length of 33 m and a diameter of 0.55 m. The shock tube is 17 m long with a diameter of 0.15 m. The HEG was designed to provide a pulse of gas to a hypersonic convergent - divergent nozzle at stagnation pressures of up to 200 MPa, and stagnation enthalpies of up to 23 MJ/kg. Regarding the test gas, no basic limitations exist. The operating conditions presented in the present article are related to the test gas air. Additionally, operating conditions using nitrogen and carbon dioxide exist.

### 2.2.1 HEG Operating Conditions

Originally, HEG was designed for the investigation of the influence of high temperature effects such as chemical and thermal relaxation on the aerothermodynamics of entry or re-entry space vehicles. As discussed above, in order to correctly model the chemical relaxation occurring behind the bow shock of a re-entry vehicle, the flight binary scaling parameter must be reproduced in ground based testing. Further, for high enthalpy testing an additional driving parameter which must be reproduced is the flow velocity. Therefore, the operating conditions of HEG are first discussed in Figure 6 in terms of the binary scaling parameter $\rho L$ and the flow velocity u. Here L represents the length of the considered configurations. In addition to the HEG operating conditions, the most important fluid mechanical and chemical processes occurring during re-entry of a spacecraft in the Earth's atmosphere are depicted in Figure 6. Further, as reference, the flight trajectories of a lifting body re-entry from low Earth orbit (IXV), a ballistic super orbital re-entry (Apollo 11) and a hypersonic flight experiment (SHEFEX) are provided. An indication of the corresponding flight altitudes is given in the right diagram of Figure 6 showing the temperature variation of the Earth's atmosphere. The transitions between regimes of different physical and chemical properties shown in Figure 6 depend on the chosen reference length and vary when different configurations are considered. Further, the boundaries shown have only symbolic character. In reality, no clear-cut dividing lines between the different regimes exist. The Knudsen number given in Figure 6 shows that the HEG operating conditions are located in the continuum flow regime. The high energy content of re-entry flows leads to strong heating of the air in the vicinity of a spacecraft. Depending on the temperature level behind the shock wave (i.e. the flight velocity), the vibrational degrees of freedom of the air molecules are excited and dissociation reactions of oxygen- and nitrogen molecules may occur. Further, ionisation of the air constituents occurs. The high temperature effects described here are enabled by energy transfer from the translational energy stored in the random motion of the air particles, which is increased by the gas heating, to other forms of energy. Because this energy transfer is realised by air particle collisions, it requires a certain time period to develop. The time required to reach an equilibrium condition, is e.g. defined by the local temperature and density. Therefore, depending on the ratio of the relaxation time to a characteristic timescale of the flow, the chemical and thermal relaxation processes can be either in non-equilibrium or in equilibrium. Further, along a re-entry trajectory, the Reynolds number

varies over several orders of magnitude. In high altitude flight the wall boundary layer of a re-entry vehicle is initially laminar. After exceeding a critical Reynolds number (shown exemplarily for the IXV configuration in Figure 6), the transition from a laminar to a turbulent boundary layer takes place. This process is linked with an increase of the skin friction and the wall heat flux.

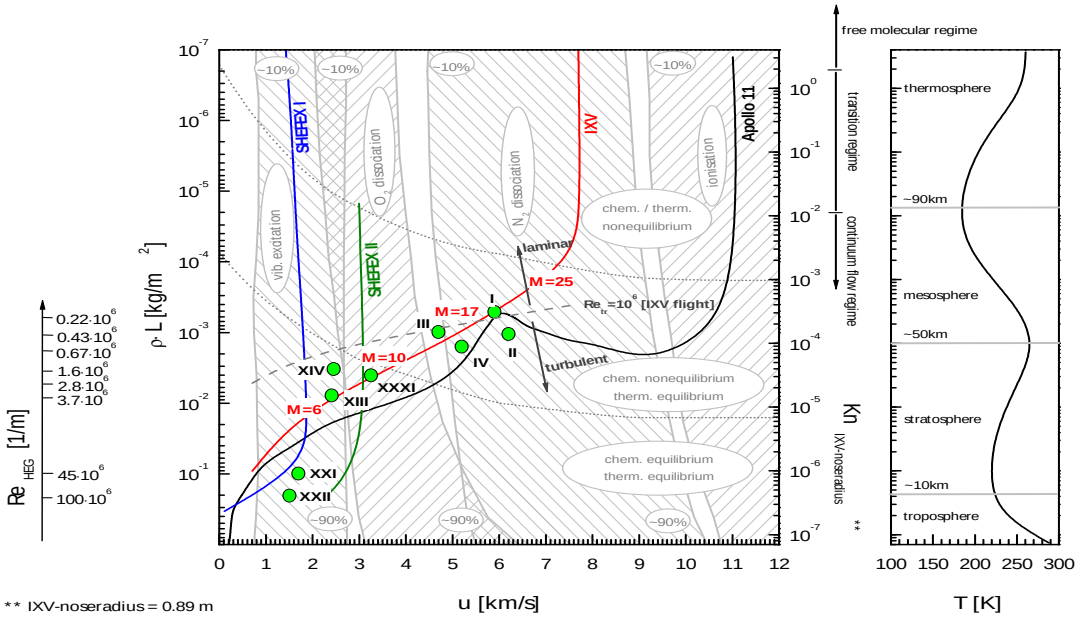


**Figure 6: HEG operating conditions in terms of the binary scaling parameter ρL and the flow velocity u**

The HEG operating conditions I – IV are the original high enthalpy conditions covering a total specific enthalpy range from 12 – 23 MJ/kg. A detailed discussion of these conditions is given in Hannemann et al. [28]. They have e.g. been used for the investigation of several re-entry configurations including ARD, X-38 [32] or Pre-X / IXV.

Over the last years the HEG operating range was subsequently extended. In this framework the main emphasis was to generate test section conditions which allow investigating the flow past hypersonic configurations at low altitude Mach 6 up to Mach 10 flight conditions in approximately 33 km altitude. These low enthalpy conditions cover the range of total specific enthalpies from 1.5 – 6 MJ/kg. For 1:1 scale wind tunnel models, conditions XIII and XIV duplicate M = 7.4 flight conditions in 28 km and 33 km, respectively. They were used for the ground based testing of the HyShot II [53] and IV supersonic combustion flight experiment configurations. Condition XXI is related to M = 6 flight conditions in 15 km flight altitude and condition XXII represents the HEG operating condition with the highest unit Reynolds number. Condition XXI was e.g. used in the framework of the SHEFEX I post flight analysis and the investigation of the intake of the LAPCAT (EC project "Long Term Advanced Propulsion Concepts and Technologies") M = 8 aircraft. Condition XXXI focuses on M = 10 flight conditions in 33 km altitude. It will be used in the framework of the DLR SHEFEX II flight experiment and was applied for the ground based testing of a 1:1 scale scramjet flight experiment configuration.

With reducing flight velocity or i.e. total specific enthalpy, the binary scaling parameter becomes less important. However, for 1:1 scale models of hypersonic flight configurations, the ρL versus u diagram gives an indication of the dynamic pressure range which can be reproduced in HEG. In particular for airbreathing propulsion driven hypersonic vehicles this quantity is of interest. Typically they fly at dynamic pressures between 50 and 100 kPa and in order to model the combustion process in e.g. a

scramjet engine correctly, the dynamic pressure is one of the quantities which must be duplicated [42]. In Figure 7, the low enthalpy HEG operating conditions are also given in terms of Mach and Reynolds number. As reference length, a fixed wind tunnel model length of 0.3 m and the lengths of the considered flight configuration were used.

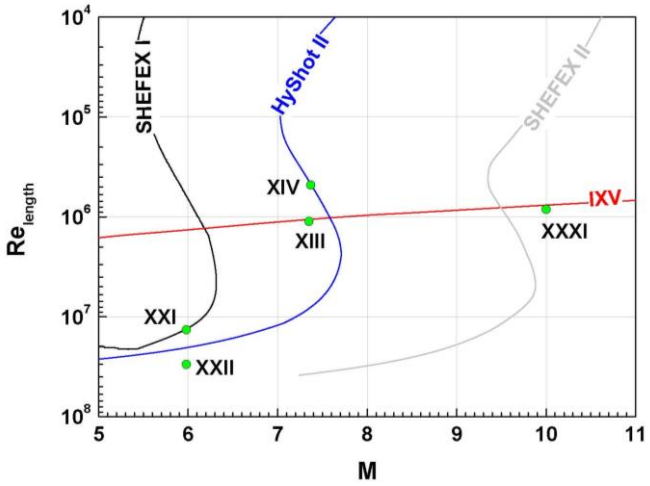


**Figure 7: HEG operating conditions in terms of Mach and Reynolds number**

Details of the HEG operating conditions discussed above are provided in Table 1. The test time for the high enthalpy conditions I – IV is up to 1 ms. For the low enthalpy conditions, the test time ranges from 3 – 6 ms.

| **Nozzle** | **2** | | | | **3** | | **4** | | **5** |
|---|---|---|---|---|---|---|---|---|---|
| **Condition** | **I** | **II** | **III** | **IV** | **XIII** | **XIV** | **XXI** | **XXII** | **XXXI** |
| $p_0$ [MPa] | 35 | 85 | 44 | 90 | 17 | 8 | 37 | 54 | 70.0 |
| $T_0$ [K] | 9100 | 9900 | 7000 | 8100 | 2740 | 2810 | 1640 | 1200 | 4400 |
| $h_0$ [MJ/kg] | 22 | 23 | 12 | 15 | 3.3 | 3.4 | 1.5 | 1.3 | 6.0 |
| $M_\infty$ [-] | 8.2 | 7.8 | 8.1 | 7.9 | 7.4 | 7.4 | 6.0 | 6.1 | 10.3 |
| $Re_m$ [1/m· $10^6$] | 0.20 | 0.42 | 0.39 | 0.67 | 3.70 | 1.60 | 45.0 | 100.0 | 2.8 |
| $p_\infty$ [Pa] | 660 | 1700 | 790 | 1680 | 1990 | 880 | 20100 | 29400 | 930 |
| $T_\infty$ [K] | 1140 | 1450 | 800 | 1060 | 266 | 277 | 221 | 152 | 253 |
| $\rho_\infty$ [g/$m^3$] | 1.7 | 3.5 | 3.3 | 5.3 | 25.9 | 11.0 | 327.0 | 682.0 | 12.6 |
| $u_\infty$ [m/s] | 5900 | 6200 | 4700 | 5200 | 2410 | 2450 | 1750 | 1510 | 3270 |

**Table 1: Summary of HEG nozzle reservoir and test section flow conditions**

In order to realise the operating conditions of Table 1, a series of different Laval nozzles had to be designed, constructed and implemented in HEG. The nozzles used to generate the corresponding test conditions are given in Table 1. Details of the four operational HEG nozzles are provided in the following section. Further, different pistons are utilised on HEG for generating different operating conditions. In order to allow a large flexibility in tuning new operating conditions, four pistons (without brakes) with different weight (275 kg, 481 kg, 700 kg and 815 kg) are available. One additional 848 kg piston with brakes is utilised.

### 2.2.2 Set of HEG Nozzles

The set of HEG nozzles comprises of a conical nozzle used for the high enthalpy conditions I-IV and three contoured nozzles for the low enthalpy conditions. Their nominal design Mach number, area ratio and length are given in Figure 7. Please note that for nozzle 2 the Mach number is lower than the corresponding flight Mach number (see also Figure 6) due to chemical and thermal freezing effects during the nozzle expansion [28]. However, for high enthalpy testing the Mach number is of less importance and the flight velocity must be reproduced correctly.

Due to the different nozzle length, a second test section was built for nozzle 3. When utilising nozzle 4, an additional adapter ring is used between the second and the main test section. The length and diameter of the original test section is 1.6 m and 1.2 m, respectively. The second test section is a copy of the original test section with slightly reduced dimensions (1.0 m length and 1.0 m diameter). The adapter ring has a length of 0.8 m and a diameter 1.0 m. The nozzle – test section assembly using the four HEG nozzles is shown in Figure 9. Depending on the used operating condition and the angle of attack, model configurations with a typical length between 0.4 m and 1.0 m and a width of up to 0.4 m can be mounted in the test sections. In case the major emphasis of the tunnel testing is on the investigation of internal flow paths (e.g. scramjet combustors), models of up to 2.0 m length can be used. The weight of the models is typically less than 200 kg.

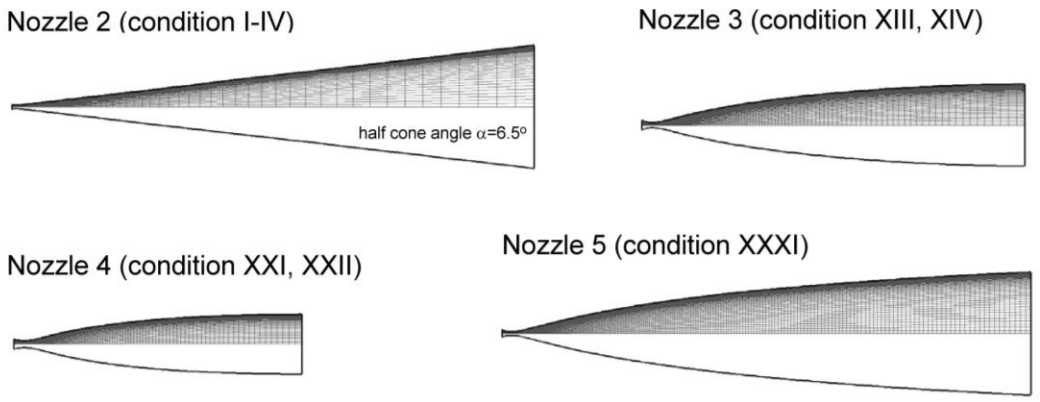


| Nozzle | 2 | 3 | 4 | 5 |
|---|---|---|---|---|
| nominal M | 8 | 8 | 6 | 10 |
| d*[mm] | 22 | 40 | 50 | 26 |
| $d_{Exit}$[mm] | 880 | 590 | 430 | 880 |
| $A_{Exit}/A^*$ | 1600 | 218 | 74 | 1146 |
| L [mm] | 3780 | 2710 | 2015 | 3780 |

**Figure 8: Geometry of operational HEG nozzles**

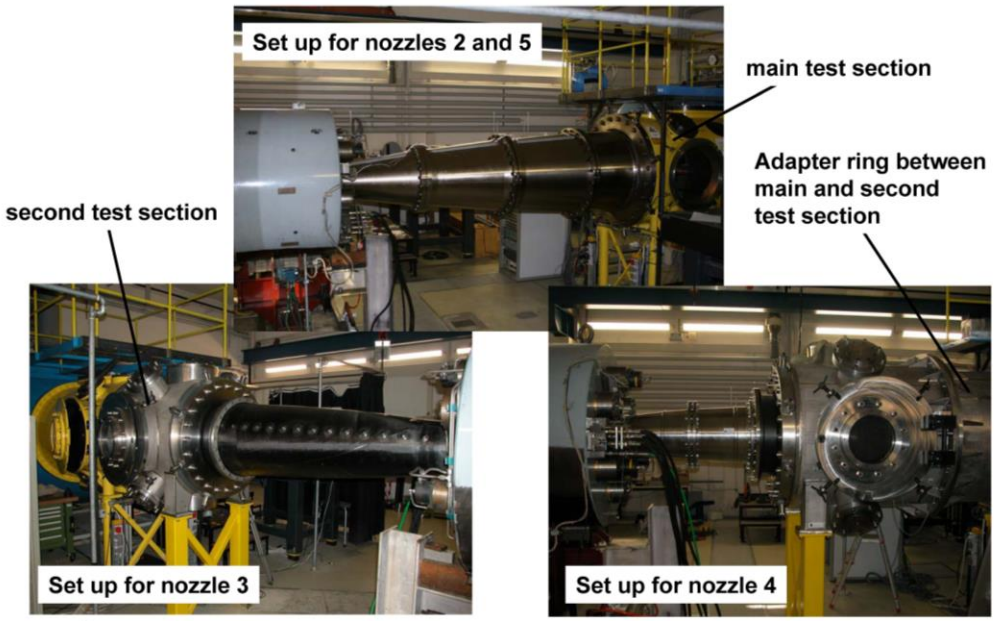


**Figure 9: HEG nozzle – test section assembly**

### 2.2.3 Recent HEG Infrastructure Upgrades

The data acquisition system of HEG consists of a total of 180 channels. Two different types of transient recorders are currently used. The original KRENZ System from Eckelmann Industrie Automation with 60 channels is characterised by 1 MHz sampling rate and 0.1 Mega samples per channel at 14 Bit resolution. The new SATURN System from AMO GmbH provides 120 channels. Its sampling rate is 50 MHz and 10 Mega samples per channel can be recorded at 16 Bit resolution.

A gaseous hydrogen injection system was installed at HEG in order to allow the delivery of hydrogen fuel to wind tunnel models for the investigation of scramjet combustion. The fuel system consists of a 12 mm diameter and 38.4 m long Ludwieg tube, and a fast acting solenoid valve. The maximum filling pressure of the Ludwieg tube is 15 MPa and it can deliver a pulse of fuel with constant pressure for up to 50 ms.

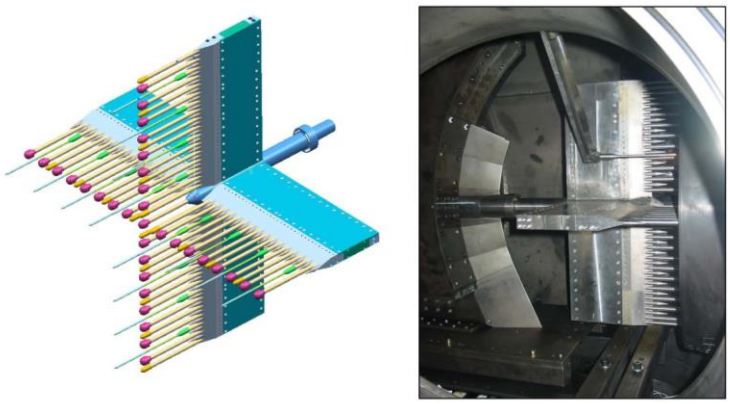

**Figure 10: HEG calibration rake – design drawing (left) and rake installed in the test section (right)**

A new modular cross arm calibration rake was designed and manufactured which can be used for the detailed calibration of the test section free stream flows generated by nozzles 2 – 5. Pitot pressure, static pressure and stagnation point heat transfer gauges can be mounted on this rake (see Figure 10).

# 3.0 MEASUREMENT TECHNIQUES FOR SHORT DURATION HYPERSONIC GROUND BASED TESTING

In this section an overview of measurement techniques, which are suitable for short duration hypersonic ground based testing, is given. The emphasis is put on those techniques which are applied in the High Enthalpy Shock Tunnel Göttingen, HEG.

## 3.1 Pressure Measurements

Surface pressure measurements in short duration facilities require different approaches compared to continuously running facilities. Because the measurement time is short, pressure transducers with fast response time have to be used. Additionally, the susceptible area of the transducer must be installed close to the surface to minimise the filling time of the tubing system in front of the susceptible area. The most commonly used pressure gauges in short duration hypersonic ground based testing are based on the piezoelectric and on the piezoresistive effect. The piezoelectric effect leads to the generation of a voltage in a crystal and the piezoresistive effect leads to an increase of the resistance of a semiconductor when a pressure load is applied. Optical fibre pressure transducers based on different principles including intensity modulation, interferometry, polarization effects, refractive index changes, reflectometry and fibre Bragg grating are currently under development. A review of micromachined pressure gauges is given e.g. in [14]. The development of an optical pressure gauge based on a Fabry-Pérot interferometer with a natural frequency above 1 MHz, enables data capture over a bandwidth exceeding 100 kHz ([93]). This results in response times which are suitable for short duration hypersonic testing.

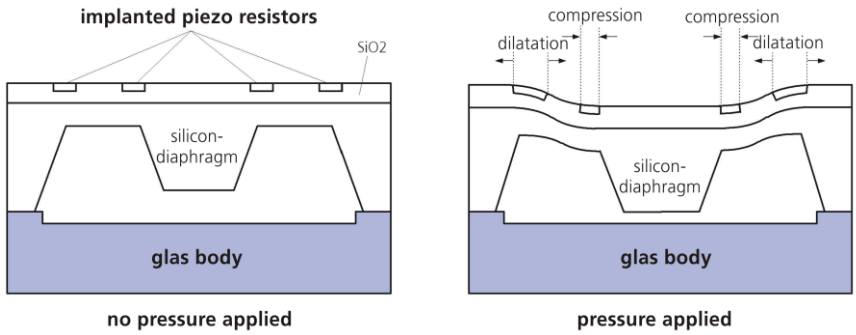


**Figure 11: Schematic of a Kulite piezoresistive pressure transducer**

Miniaturised fast piezoresistive pressure transducers are e.g. manufactured by Kulite. Depending on the pressure range, the Kulite XCEL-100 pressure gauge with a diameter of 2.4 mm has a natural frequency between 240 kHz and 1 MHz and a bandwidth of 20 kHz. Figure 11 shows the schematic of a Kulite pressure transducer. A silicon element is used as mechanical diaphragm and the sensing element itself is an integral part of this silicon element. The piezoresistors are formed within the silicon diaphragm by either diffusion or implantation of atoms. Two of these resistors are positioned on the silicon diaphragm such that they experience a compressive strain, and two are positioned such that they experience a tensile strain. They are connected to form a fully active Wheatstone bridge. These transducers may be manufactured very small-sized: diameters of the housing can be in the range of 1 to 2 mm.

To achieve fast response times, it is necessary to position the susceptible area of the transducer as close as possible to the model surface. As shown in Figure 12, small holes are drilled in the model which act as pressure tappings. The gauge is placed directly behind these tappings. In Figure 12, the schematic of two different types of pressure gauge installations as used in HEG is shown.

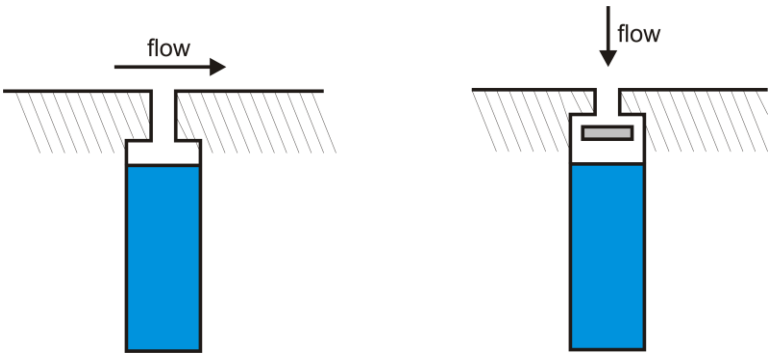


**Figure 12: Installation of pressure transducers into a model wall (transducers shown in blue)**

Typical tapping diameters range from 0.5 to 1.5 mm. The schematic on the left side of Figure 12 shows an installation suited for tappings perpendicular to the flow. This installation is not suited for stagnation regions, where the flow may directly stagnate on the pressure transducer, leading to a high heat flux on the susceptible area. A stagnation point installation is shown on the right side of Figure 12. Here the susceptible area of the transducer is protected by a stagnation plate. Examples of pressure measurements using both configurations are given in Figure 13. One pressure transducer was mounted in the side wall of a shock tube and two transducers were installed in the end wall, measuring the pressure rise caused by the reflection of the incident shock wave. It is clear that the stagnation plate leads to an increase of the rise time. For the applied tapping diameter and cavity size, the resulting increase amounts to about 0.15 ms.

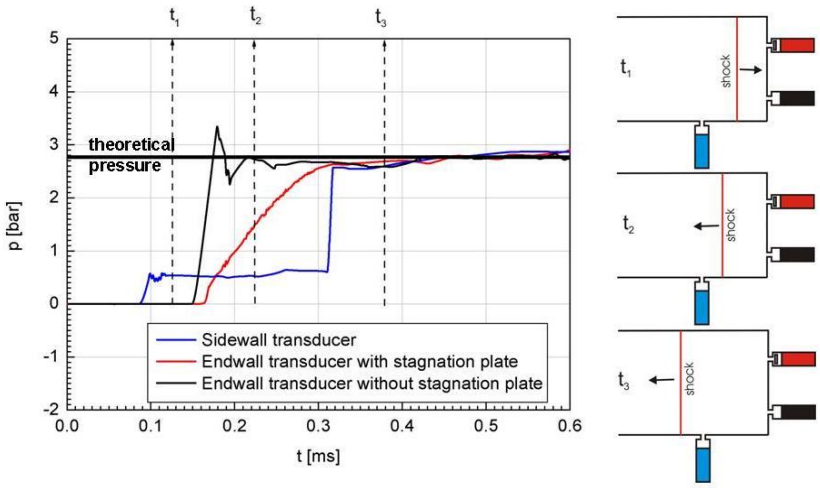


**Figure 13: Rise time investigation for different pressure gauge installations in shock tube walls**

## 3.2 Surface Heat Flux Measurements

In short duration high enthalpy, hypersonic ground based test facilities the most common way to measure wall heat flux is by utilising thin film gauges or thermocouples. Due to the harsh environment in these facilities with high wall shear stresses during the starting process of the flow, the most robust and reliable

technique to measure heat flux is the application of surface mounted coaxial thermocouples. The principle of operation of thermocouples is the Peltier-Seebeck or thermoelectric effect ([48]).

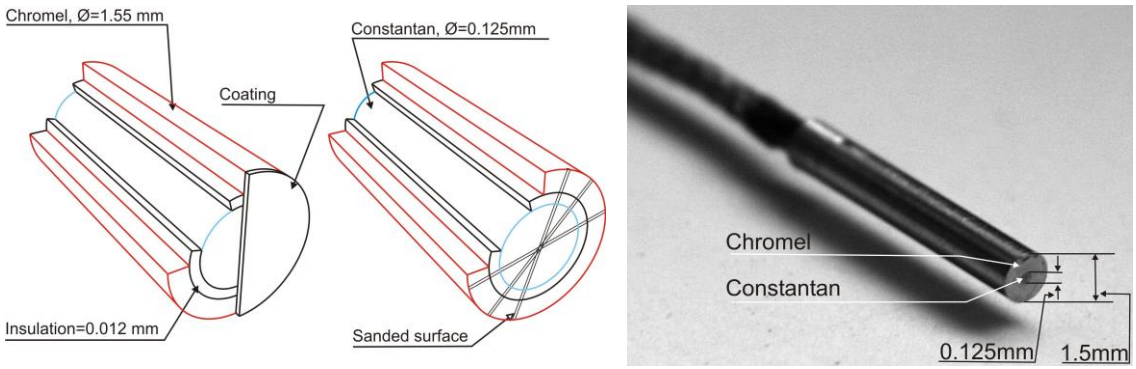


**Figure 14: Schematic of MedTherm type E thermocouple (left) and photograph (right)**

In order to allow a detailed instrumentation of wind tunnel models, miniaturized thermocouples with diameters as small as 0.4 mm are used. Figure 14 shows a schematic view of a miniaturized coaxial ultra fast thermocouple manufactured by Medtherm Corporation ([56]). Coaxial thermocouples are built with a core consisting of one conductive material separated by insulation from the outer ring made of a different material. Possible material combinations and their official ISA (Instrument Society of America) code are given in Table 2 together with their application range. The electrical connection on the top surface is realized either by coating the surface with one of the materials or simply by sanding of the transducer surface. In either case the mass of the electrical connection in comparison to the mass of the transducer body is small leading to response times of thermocouples in the order of a few µs. Additionally, the heat flux into the transducers is dominated by the thermocouple body and the junction itself is negligible due to its low mass. The sensitivity of thermocouples range from 1 µV/K to 70 µV/K. The thermocouple inherits the advantage, that the shape of the transducer can be adapted to any wall curvature by sanding. Further, in case of transducer failure, it can also be repaired in situ by sanding the surface.

| ISA code | Material A (+) | Material B (-) | Application Range |
|---|---|---|---|
| B | Platinum 30% Rhodium | Platinum 6% Rhodium | 1640K to 1970K |
| C | 95% W5Re Tungsten 5% Rhenium | W26Re Tungsten 26% Rhenium | 1920K to 2585K |
| E | Chromel | Constantan | 365K to 1170 |
| J | Iron | Constantan | 365K to 1030K |
| K | Chromel | Alumel | 365K to 1530K |
| N | Nicrosil | Nisil | 920K to 1530K |
| R | Platinum 13% Rhodium | Platinum | 1140K to 1720K |
| S | Platinum 10% Rhodium | Platinum | 1250K to 1720K |
| T | Copper | Constantan | 70K to 620K |
| Chromel* | 90% Nickel 10% Chromium | | |
| Alumel* | 95% Nickel 2% Manganese 2% Alumimnium 1% silicon | | |
| Constantan | 55% Copper 45% Nickel | | |
| Nisil+ | 95.6% Nickel 4.4% Silicon | | |
| Nicrosil+ | 84.1% Nickel 1.3% Silicon 14.6% Chromium | | |
| *Trademarks of Hoskins Manufacturing Company, +Trademarks of Harrison Alloys, Inc. | | | |

**Table 2: Possible material combinations and application ranges of thermocouples**

Alternatively to thermocouples, in areas with less harsh flow environments such as wake flows or surfaces at small angles of attack, thin film gauges can be used to measure the temperature history in order to evaluate the heat flux (e.g. [62] or [60]). Thin film gauges consist of a nonconductive substrate on which a

metallic film with a typical thickness of less than 1 µm is metallised. The working principle of these gauges is based on the dependence of the electrical resistance of the metallic film on temperature. For the metallic film noble metals are used because they exhibit the largest sensitivity. Again, the mass of the susceptible area is very small compared to the body in which the heat is conducted. Therefore, similar response times as for thermocouples are obtained.

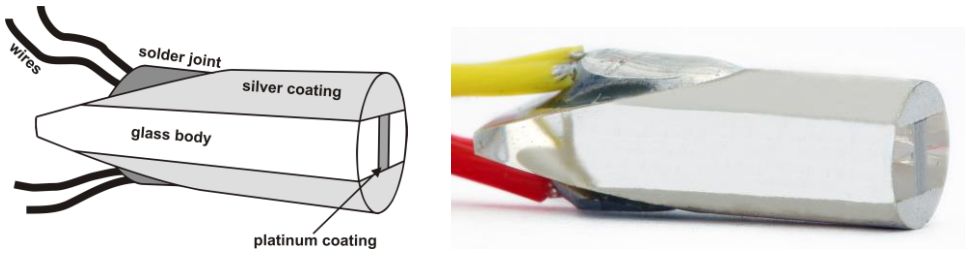


**Figure 15: Schematic of ISL thin film gauge (left) and photograph (right); (diagram and photograph courtesy ISL)**

As an example, in Figure 15, a thin film gauge as manufactured by the French-German Research Institute of Saint-Louis (ISL) is shown. The measuring point is a thin platinum film, which is metallised on a glass body. The electrical connection to the measurement wires is realized by a silver coating of the upper and lower third of the glass body. The typical diameter of these gauges is in the order of millimetres. The temperature sensitivity and signal to noise ratio of thin film gauges are superior to thermocouples. However, disadvantages are the missing robustness in harsh flow environment as usually found in short duration facilities, the large effort of adapting the susceptible area to curved surfaces and the missing possibility to repair the gauge in situ.

Two assumptions are used to evaluate the heat flux from the measured temperature traces using coaxial thermocouples or thin film gauges. The first assumption is that the measurement is dominated by one dimensional heat conduction in the sensor body, and the second is that the gauge itself acts as a semi infinite body ([77]). To ensure that the first assumption is valid, only the transducer face should be exposed to the flow, and the combination of wind tunnel model wall material and transducer material has to be chosen in an appropriate way. The validity of the semi infinite body assumption requires $x \geq \sqrt{\alpha \cdot t}$ ([15]), where $x$ is the length of the transducer, $\alpha$ the diffusivity and $t$ the time. The diffusivity, $\alpha$, is defined as the ratio of the heat conductivity, $\kappa$, and the product of density, $\rho$, and specific heat capacity, $c$, $\alpha = \kappa / \rho \cdot c$. For thermocouples of ISA code E with a length of 10 mm the time before the heat reaches the end of the transducer is approximately 3 s. This period of time is orders of magnitude higher than the typical test time in short duration facilities of a few milliseconds. If the two assumptions mentioned above can be regarded as valid, the heat conduction problem in the transducer body is described by the following differential equation:

$$\frac{\partial^2 T}{\partial x^2} = \frac{1}{\alpha}\frac{\partial T}{\partial t}. \tag{1}$$

Here, T is the temperature, x the coordinate normal to the wind tunnel model wall and t the time. With the boundary conditions that the heat flux into the model wall, $\dot{q}_w(x=0) = -\kappa(\partial T / \partial x)$ and $T(x=\infty) = 0$, the following equation can be derived for the evaluation of the heat flux as shown by Schultz & Jones [77]:

$$\dot{q}_W(t) = \sqrt{\frac{\rho c \kappa}{\pi}} \left[ \frac{T(t)}{\sqrt{t}} + \frac{1}{2} \int_0^t \frac{T(t) - T(\tau)}{(t-\tau)^{3/2}} d\tau \right]. \tag{2}$$

For the evaluation of the wall heat flux by numerical integration of digitally stored temperature data, the above relationship is replaced by a discretised form such as

$$\dot{q}_W(t_n) = 2\sqrt{\frac{\rho c \kappa}{\pi}} \sum_{j=1}^{n} \frac{T_j - T_{j-1}}{\sqrt{t_n - t_j} + \sqrt{t_n - t_{j-1}}}, \tag{3}$$

proposed by Cook and Felderman [13] or an alternative scheme described by e.g. Kendall et al. [44].

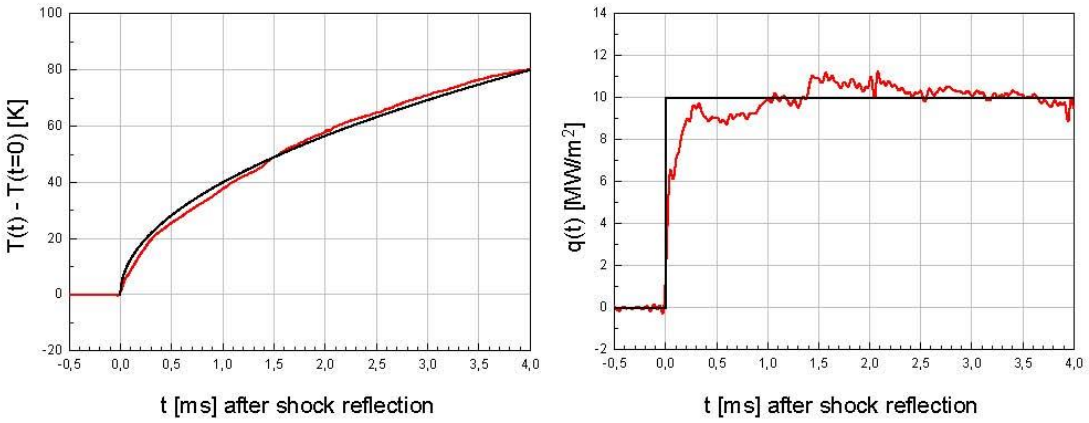


**Figure 16: Heat flux evaluation of a temperature recording in a shock tunnel (red) compared with the temperature evolution based on a stepwise heat transfer load (black)**

In Figure 16 an example obtained with the data evaluation method of Cook and Felderman [13] is presented. On the left side of Figure 16, the temperature development measured by a type E thermocouple installed in the stagnation point of a sphere positioned in a hypersonic flow with total specific enthalpy of $h_0$ = 15 MJ/kg is indicated by the red line. On the right hand side of Figure 16, the resulting heat flux over time (red line) is shown. If the heat flux into the wall is given by an ideal step function, the exact solution for the temperature rise at $x = 0$ resulting from equation (1) is:

$$T_W(x=0,t) = \frac{2\dot{q}_W}{\sqrt{\pi}} \sqrt{\frac{t}{\rho \cdot c \cdot \kappa}}. \tag{4}$$

Using a constant heat flux into the transducer body of $\dot{q}_W$ = 10 MW/m$^2$ as approximation of the measured heat flux evolution (the black line in the right part of Figure 16), the parabolic temperature history profile shown as black line in the left part of Figure 16 is obtained.

To ensure that the measurement is not affected by conduction in wall tangential direction, the thermocouple type should be chosen in such a way, that the material properties of the model wall match those of the thermocouple at the measurement position. The influence of different thermocouple / model wall material combinations on the measured temperature distribution is shown in Figure 17 and Figure 18. These results were obtained by numerical investigation of the unsteady heat conduction process in a type E thermocouple with 1.5 mm diameter and a length of 15 mm, installed in model walls of different materials, using Ansys (CAD-FEM GmbH). The thermocouple is modelled as a solid cylinder consisting of chromel. At the top surface a constant heat flux of $q_w$ = 10 MW/m$^2$ is applied. The temperature

evolution at the contact point between the thermocouple and the model wall is given in Figure 17 for three different model wall materials. Dependent on the material, large differences of the temperature evolution are obtained.

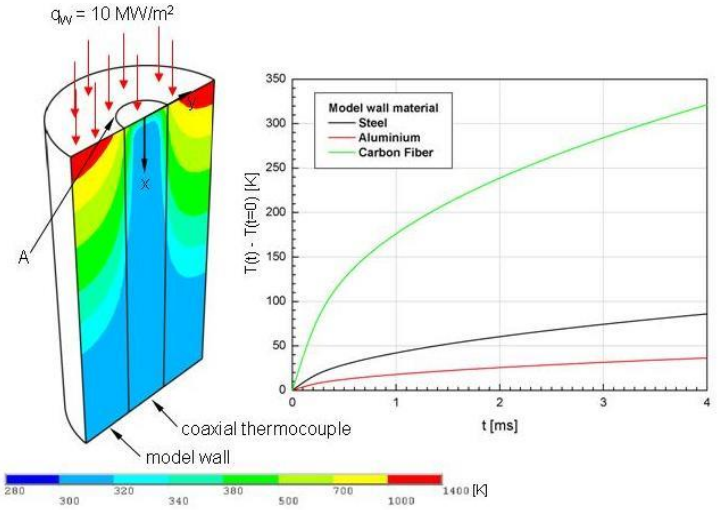


**Figure 17: Unsteady finite element analysis of the heat conduction process in a type E thermocouple and the adjacent model wall for a wall heat flux of 10 MW/m$^2$; axisymmetric temperature distribution at t=4 ms for a carbon fibre model wall (left) and time evolution of the temperature at the interface (A) between the thermocouple and the model wall for different wall materials (right)**

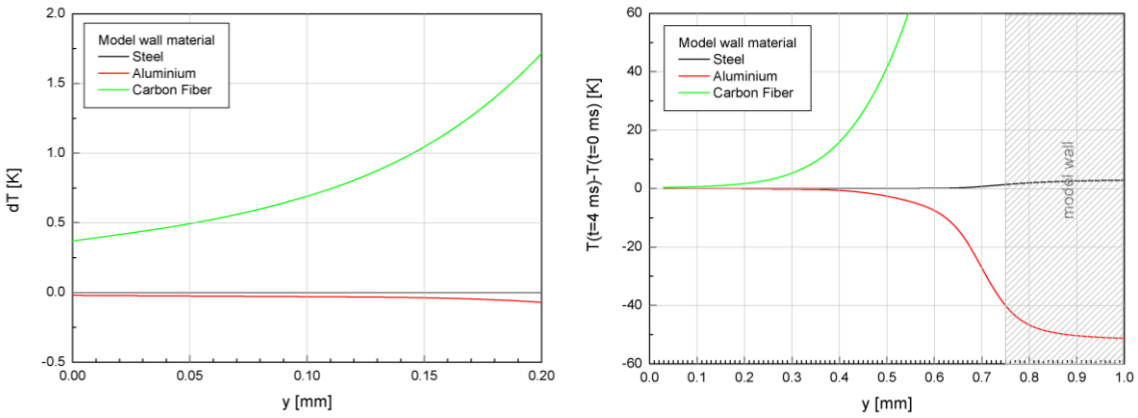


**Figure 18: Difference of radial computed temperature distribution at the model wall and thermocouple surface obtained for different thermocouple / wall material combinations compared to the combination chromel / chromel for which no temperature difference between thermocouple and wall exists**

The difference of the radial temperature distribution at the model wall and thermocouple surface obtained for the thermocouple / wall material combination chromel / chromel, i.e. a combination for which no temperature difference between the thermocouple and the model wall exists, and the material combinations chromel / steel, chromel / aluminium and chromel / carbon fibre are plotted in Figure 18. On the left side of Figure 18, a zoom of the core region of the thermocouple is shown. The right side of Figure 18 shows the distribution up to a radius of 1 mm. In case of a coated thermocouple with dimensions as shown in Figure 14, the temperature measurement takes place at y = 0 - 0.0625 mm, the location of the

chromel / constantan junction. For a thermocouple which is adapted to a three dimensional surface or repaired in situ by sanding, the chromel / constantan junction is not precisely defined and the complete thermocouple surface may act as the measurement location. As can be seen from Figure 18, depending on the thermocouple / wall material combination the assumption of one dimensional heat conduction can be violated.

From equation (2) it becomes evident, that the error in the estimation of the heat flux is directly proportional to the error resulting from the determination of $\sqrt{\rho c \kappa}$. To accurately measure this value two procedures may be applied. The contact procedure is used for thermocouples and thin film gauges and is based on the fact that under the assumption of one dimensional heat conduction, the contact temperature of two media is only dependent on their temperature before contact and on the thermal properties ($\sqrt{\rho c \kappa}$) of both media. Knowing the thermal properties of one media allows to determine the gauge properties. A possible setup is a mechanically driven device that generates an instantaneous contact between the gauge and a liquid surface. Such a method is discussed by Jessen and Grönig [41]. The electric discharge calibration can only be applied for thin film gauges. It utilizes the effect that with an electric discharge, the thin film itself can be heated with a known and constant heat flux. Following equation (3), the measurement of the temperature of the thin film gauge results in the determination of $\rho c \kappa$.This procedure is described by e.g. Skinner [81].

## 3.3 Force and Moment Measurements

The ability to perform integrated force and moment measurements in ground based testing facilities is an important part of the design and development of hypersonic vehicles. For a force balance to operate in short duration ground based test facilities with test times of the order of milliseconds or less, it would become necessary for the balance to have an extremely short response time. However, given the short test times and the response times of force measurement techniques for convential wind tunnels (see e.g. Ewald [17]), static equilibrium between the model and support structure is rarely established, i.e. it may only be obtained using unrealistically small models. Therefore, it becomes necessary to use specialised measurement methods that account for the dynamic response of the system. An overview of the basic force measurement techniques that have been applied in short duration flows is given e.g. by Robinson [72].

In HEG a stress wave force balance was implemented [73]. This technique relies on the ability to measure the dynamic response of the model and supporting structure. Consequently, any effects such as model flexibility and mass distribution are accounted for (see e.g. Robinson [72]). Stress wave force balances require a dynamic calibration of the complete model, balance and support structure assembly.

Upon flow arrival, stress waves propagate through the model at the speed of sound of the material and subsequently enter a stress bar that is instrumented with a strain gauge to record the time history of strain. If the system is linear, the resulting strain signal, y(t), can be related to the applied aerodynamic load, u(t), via an impulse response function, g(t), as described by the convolution integral,

$$y(t) = \int_0^t g(t-\tau)u(\tau)d\tau \,. \tag{5}$$

The aerodynamic force in an experiment can be determined by the deconvolution of the strain signal with the impulse response function. The impulse response function is determined either through experimental calibration or through finite element analysis. However, in order to reduce errors due to modelling approximations it is usually preferable to determine the impulse response function experimentally.

Sanderson and Simmons [75] first demonstrated the technique by measuring the drag force on a 15º conical model, 200 mm in length in a reflected shock tunnel. The model was made from aluminium and attached to a 2 m long hollow brass bar. This stress bar or sting, was instrumented with strain gauges to record the axial strain time history. The test time was approximately 1 ms and the aerodynamic load was subsequently found through a numerical deconvolution process. The measured drag was found to be in good agreement with theoretical calculations.

The technique was then extended to measure multiple components of force by Mee et al. [57]. This was done on a 15º cone with an internal balance arrangement. The lift, drag and pitching moments were measured by short, stiff stress bars instrumented with strain gauges. The technique has subsequently been applied to a wide variety of models, including models with simultaneous measurements of pressure and heat flux. The major disadvantage with this technique is that aerodynamic shielding and vibration isolation of the support structure is required in order to separate the stress waves generated in the model from that of the test section environment. Calibration of the model is usually performed using an instrumented impact hammer or via a cut-weight technique. In order to maximise the performance of stress wave force balances, an individual design for each configuration to be tested is recommended.

Stress wave force balances have been developed with external as well as internal stress bar arrangements. The internal three component force balance applied by Robinson and Hannemann [73] in HEG, is shown in Figure 19. Four short stiff stress bars are mounted on a sting and each bar is instrumented with semiconductor strain gauges to measure the time history of strain. The balance is able to measure forces (approximately 50 to 5000 N) within 1 – 5 ms on instrumented models at angles of attack from -40 - 20°. The accuracy of the force balance is estimated at approximately ±5% for the axial component and ±4% for the normal and pitching moment components.

Additional force measurement techniques based on external stress wave force balances, accelerometer based and free flight based force measurement techniques are currently under development in HEG.

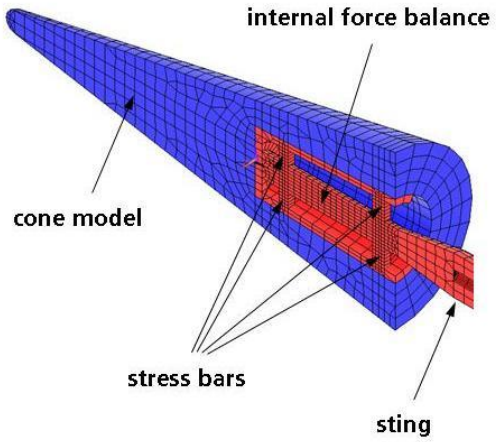


**Figure 19: Finite element discretisation of the internal stress wave force balance - cone model set up used in the HEG shock tunnel**

## 3.4 Optical Measurement Techniques

### 3.4.1 Phase Step Holographic Interferometry

Interferometry may be used as a technique to measure the variation of the refractive index in a gaseous flow in the test section of a short duration facility. This information can be used to evaluate the density

distribution of the investigated flow field. In particular, holographic interferometry does not require machining or manufacturing of test section windows, mirrors or lenses with high precision, because parasitic effects caused by imperfections of these components cancel out when applying the holographic two step procedure. Therefore, related to the application in short duration ground based test facilities, this technique has replaced the classical and labour intensive Mach-Zehnder interferometry. In the subsequent paragraphs, a brief introduction of the phase step holographic interferometry technique is given and the set up used at HEG is described.

The absolute speed, $c_0$, at which light propagates in vacuum is a constant. In any kind of gaseous media the speed of light, $c$, will be lower. The ratio of the two speeds defines the refractive index:

$$n(\rho) = \frac{c_0}{c} = 1 + K^{\lambda}\rho \,. \tag{6}$$

The Gladstone-Dale relation describes that in a gaseous media, consisting of one species, the refractive index depends on the density, $\rho$, and the Gladstone-Dale constant $K^{\lambda}$ (see e.g. Merzkirch [59]). The latter is weakly dependent on the wavelength and is specific for each gas. For gas mixtures the refractive index is given by:

$$n(\rho) = 1 + \rho \sum_{i=1}^{S} K_i^{\lambda} \xi_i \,, \tag{7}$$

where $K_i^{\lambda}$ are the Gladstone-Dale coefficients for the single gas species, $\xi_i$ are the species mass fractions, S is the number of species and $\lambda$ is the wavelength of the laser light source. The definition of a linearly composed Gladstone-Dale constant applies not only to air and other neutral gas mixtures but also, in high temperature gas dynamics, to chemically homogenous gases where the molecules are either in different excited states, dissociated, or even ionized.

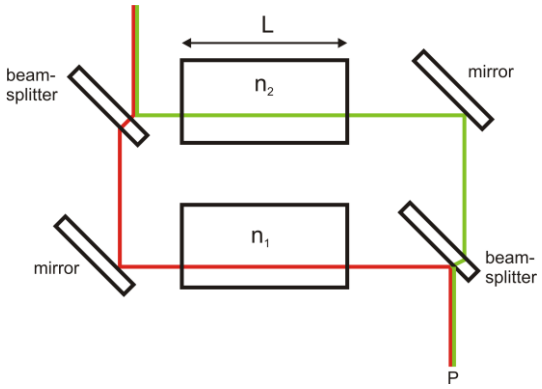


**Figure 20: Schematic of interference experiment**

The basic principle of interferometry is sketched in Figure 20. Two rays of coherent light interfere in point P. Each ray passes a zone with different refractive index, which leads to a time shift, $\Delta t$, due to the different propagation speeds of the light in the two zones:

$$\Delta t = \frac{L}{c_2} - \frac{L}{c_1} = \frac{L}{c_o}\left(n_2 - n_1\right). \tag{8}$$

If the resulting difference in the optical path length equals the wavelength, the phase shift $\phi$ between both rays is equal to $2\pi$. Therefore, the following relationship can be derived:

$$\frac{\phi}{2\pi} = \frac{L}{\lambda}(n_2 - n_1) = \frac{K_\lambda L}{\lambda}(\rho_2 - \rho_1). \quad (9)$$

The light intensity measured in point P is proportional to the phase shift between the two rays. Consequently, the measurement of the intensity or phase shift in point P is directly related to the density difference in regions 1 and 2 in Figure 20.

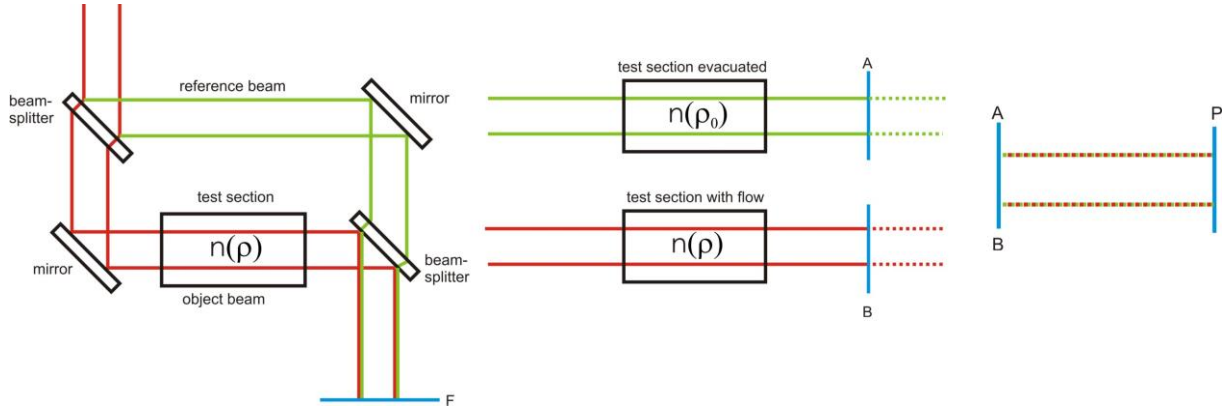


**Figure 21: Principle of Mach-Zehnder (left) and holographic interferometry (middle, right)**

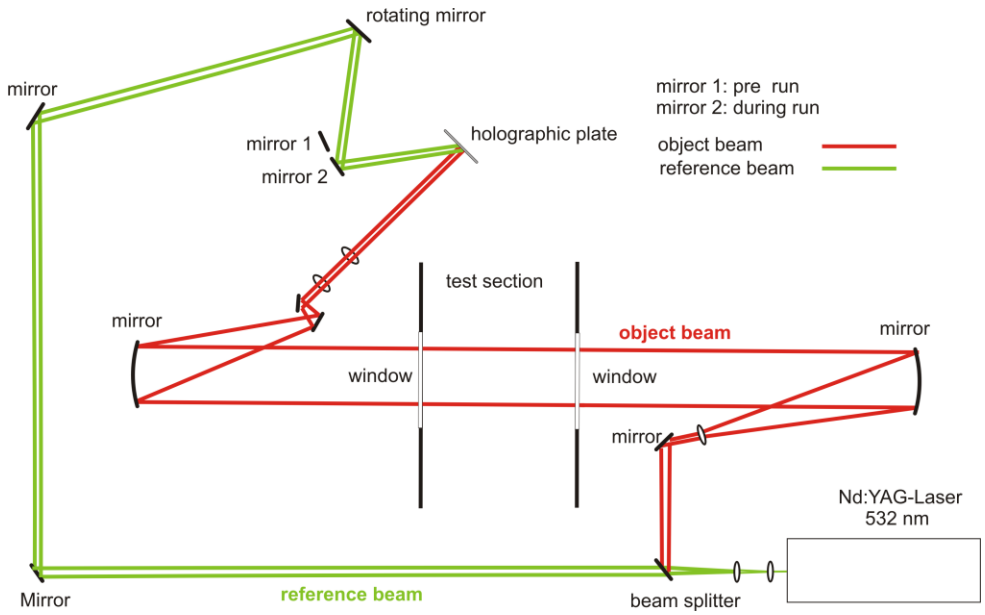


**Figure 22: Schematic setup of the HEG holographic interferometry system**

Using a Mach-Zehnder interferometer, which is shown schematically on the left side of Figure 21, the density in the test section can be evaluated if the density distribution is known at a reference point. The schematic emphasises that any imperfection which leads to a modification of the light path, disturbs the interference measurement in plane F. To avoid this, the measurement can be performed in two steps (see

middle sketch of Figure 21). In the first step, the light beam (green) passing through the evacuated test section is recorded and in the second step the light beam (red) passing through the test section with flow is recorded. Subsequently, both beams are reconstructed resulting in an interference pattern in the measurement plane, P (see right sketch of Figure 21). The advantage of this technique is that any imperfection of the optical setup modifies the path of both light beams. Therefore, they cancel out and do not influence the reconstructed interference measurement. To store and reconstruct both beams, a holographic storage technique has to be used. Therefore, this two step measurement technique is called holographic interferometry. A more detailed discussion of this technique can be found e.g. in [89].

A schematic of the holographic interferometry setup used at HEG is shown in Figure 22. The green line shows the light path of the reference beam and the red line shows the light path of the object beam. The object light beam passes through the test section and is brought to interference with the reference beam on the holographic plate. Here the interference pattern between both beams is recorded. To achieve interference between the object and the reference beam, a light source with sufficient coherence length is needed. A seeded Innolas Nd:YAG Laser (Model Spitlight 300), emitting light at 532 nm is used because it has a coherence length larger than 1 m. The optical path length of one of the beams is approximately 15 m and the successful set up of the optical system is facilitated by aligning the path length difference between the two beams to the coherence length of the laser.

The first exposure of the holographic plate with one reference beam is performed prior to a run in HEG and a second exposure with the second reference beam is obtained during the test time. After the chemical treatment of the holographic plate, two reconstruction waves are created in a separate reconstruction unit. These reference waves used in the reconstruction unit are identical to the reference waves used for both exposures.

### 3.4.2 High Speed Flow Visualization

To visualise the flow during experiments in HEG, a high speed flow visualisation system is utilised. It uses a Z-path layout for the object light path with spherical mirrors (Halle SDH4300) having a diameter of 300 mm and a focal length of 1500 mm. A schematic of the optical setup is shown in Figure 23. Two different light sources are used. The diode pulsed Nd:YAG laser from Lightwave Electronics (Model 612) emits light at 532 nm and has the capability to operate at pulse rates up to 50 kHz. Based on the specifications of the manufacturer, the HSPS (High-Speed Photo-Systeme) NANOLITE KL-K sparcflash lamp allows repetition rates up to 20 kHz with fixed pulse duration of 8 ns. If the distance of the electrodes is reduced and the sparc gap is operated in an argon atmosphere instead of air, the repetition rate can be increased up to 32 kHz. The light is widened by a telescope system (L1 and L2) and subsequently expanded by a lens (L3) onto the spherical main mirror (H1) which generates a parallel light-bundle of diameter 300 mm through the test section. On the opposite side of the test section the beam is collimated by the second spherical main mirror (H2) onto the plane mirror S3. With lens L4, the test section image is focused onto the film plane (A). In order to record Schlieren images, a razor blade (R) is positioned at the focal point of the spherical mirror H2. For flow visualisation using the shadowgraph technique, the razor blade is removed and the image plane in the test section is slightly shifted by moving lens L4 thus generating a shadowgraph effect. Image recording is performed with two different cameras. If a Cordin rotating drum camera (Model 318) is used, the images are recorded on black and white film (Kodak TMAX 100). The camera consists of a rotating drum, which is equipped with 35 mm film stripes of 1 m length. Alternatively, a Shimadzu HPV-1 digital high speed camera can be applied. This camera is able to record up to 100 frames at a maximum imaging rate of 1 MHz. Using the HPV-1 camera, the effective exposure time is defined by the pulse length of the laser of approximately 60 ns for a pulse rate of 16 kHz and 119 ns for 32 kHz. The shutter of the drum camera remains open during the experiments. Therefore, the pulse rate of the laser defines the framing rate and its narrow pulse width the exposure time. Typical laser pulse rates of 9 kHz, 10 kHz and 15 kHz result in exposure times of approximately 45 ns, 48 ns and 56 ns, respectively. Therefore, for both cameras, the high speed flow visualisation system relies on the

short duration of the laser light pulse to record a still image during the significantly larger exposure times of the cameras.

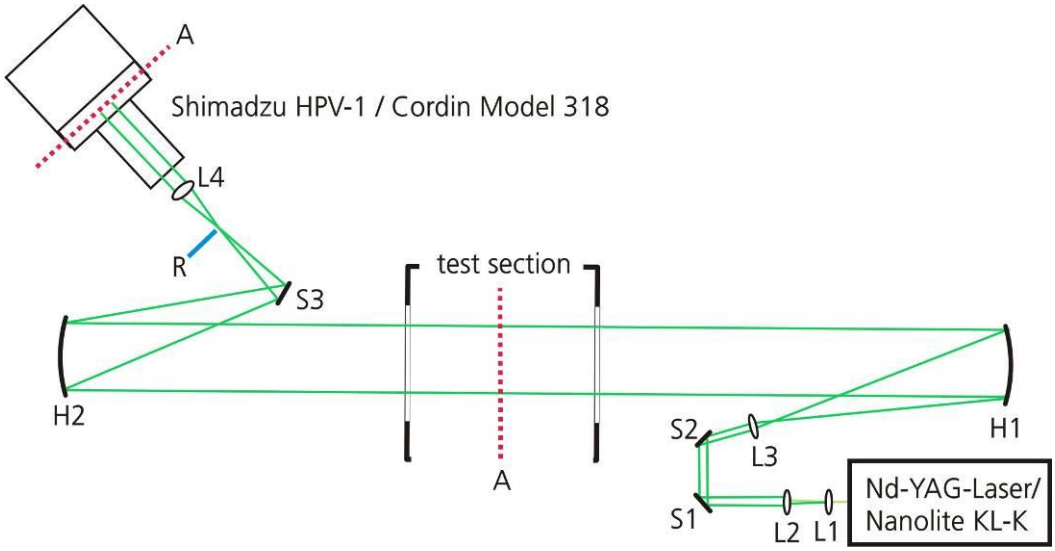


**Figure 23: Schematic of the optical setup for the high speed flow visualisation in HEG. H: Parabolic mirrors, S: Plane mirrors, L: Lenses, A: Focal plane, R: Razor blade**

# 4.0 NUMERICAL TOOL – DLR TAU CODE

## 4.1 General Overview

At DLR, the development and utilisation of CFD schemes which are able to model hypersonic and high enthalpy flows was started some 20 years ago. In a first step, the physico-chemical models necessary to compute high enthalpy flows were implemented in the implicit, upwind, Total Variation Diminishing (TVD) Thin-Layer Navier-Stokes code, NSHYP [7],[8],[9]). NSHYP was extensively used for the computation of steady two-dimensional and axisymmetric high enthalpy flow fields (see e.g. [10], [28],[29]). In order to achieve efficient steady state high enthalpy flow field computations past complex three-dimensional configurations the DLR CEVCATS-N code was developed ([68],[11]). The physico-chemical models which were tested in NSHYP were included into the DLR CEVCATS code, a block-structured, three dimensional finite-volume scheme ([45][46]). It uses multigrid strategies with residual averaging and local time-stepping to accelerate convergence to a steady state.

Finally, the DLR TAU-code [21], [79], [71] was developed. It is a CFD platform for the computation of viscous and inviscid flows which is suitable for the investigation of steady and unsteady flows past complex geometries. It covers the low subsonic up to the hypersonic flow regime. TAU comprises several means for grid modification, namely the adaptation and the deformation module. Both (block-) structured and hybrid unstructured grids composed of hexahedrons, prisms, tetrahedrons and pyramids can be utilised. The first two element types of unstructured grids are usually used in semi-structured layers above surfaces allowing for a better resolution of boundary layers. Tetrahedrons are used to fill the computational domain in a flexible way, allowing for local refinement without hanging nodes while the pyramids are needed for the transition between elements with quadrilateral faces and elements with triangular faces.

For parallel computations the grids are partitioned into a given number of domains before the start of the computation. Load balancing is performed on edge- and point weights which are adjusted to the specifications of the solver. After the grid partitioning, all other modules of TAU run on a single domain per process. Grid re-partitioning is performed either if the grid was locally (de-)refined or if the number of domains is changed.

The standard solver module uses an edge-based dual-cell approach based on a vertex-centered scheme. The pre-processing module computes the required dual grid composed of general control volumes from the primary elements. They are stored in an edge based data structure, which makes the solver independent of the element types of the primary grid. All metrics are given by normal vectors, representing size and orientation of the faces, the geometric coordinates of the grid nodes and the volumes of the dual grid cells. The connectivity of the grid is given by linking the two nodes on both sides of each face of the dual grid to the corresponding edge from the primary grid elements. In order to enable the use of a multi-grid technique an agglomeration approach is employed to obtain coarse grids by fusing fine grid control volumes together.

In the solver module, inviscid terms are computed employing either a second-order central scheme or a variety of upwind schemes using linear reconstruction (of the left and right states of a dual grid face) for second-order spatial accuracy. Viscous terms are generally computed with a second-order central scheme.

Various explicit Runge-Kutta schemes and an implicit approximate factorization scheme (Lower-Upper Symmetric Gauss-Seidel) can be used for time integration. Additional convergence acceleration is achieved by the application of full multi-grid and residual smoothing algorithms.

For time accurate computations a Jameson-type dual time stepping approach [39] is employed. Both, grid deformation as well as bodies in arbitrary motion can be simulated in this framework.

The RANS turbulence models implemented in the TAU code include linear as well as non-linear eddy viscosity models originating from both, the one- as well as the two-equation model families. The standard turbulence model in TAU is the Spalart-Allmaras model yielding highly satisfactory results for a wide range of applications while being numerically robust. Additionally, a number of two-equation models based on a k-ω formulation are available. Also nonlinear explicit algebraic Reynolds stress models (EARSM) have been integrated. The implementation and validation of Reynolds stress models is ongoing work. Further, options exist to perform Detached Eddy Simulations (DES) based on the Spalart-Allmaras [83] or the Menter SST [58] models or the so-called Extra-Large Eddy Simulation (XLES). In order to allow the modelling of transitional flows, the turbulent production terms are suppressed in regions which are flagged in the grid as being of laminar flow type.

Detailed descriptions of the modelling capabilities, solution algorithms and auxiliary tools of the TAU CFD platform are given in [78],[79] and [20].

## 4.2 Modelling of compressible and reacting high enthalpy flows

The DLR Tau code includes extensions for chemical and thermal non-equilibrium flows in high enthalpy aerothermodynamics. The flow is considered to be a reacting mixture of thermally perfect gases. A dedicated transport equation is solved for each individual species. The chemical source term in this set of transport equations is computed from the law of mass action by summation over all participating reactions. The forward reaction rate is computed from the modified Arrhenius law and the backward rate is obtained from the equilibrium constant which is computed directly from the partition functions of the participating species.

The thermodynamic properties (energy, entropy, specific heat) are calculated from the partition functions or external lookup tables for each individual species in the reacting gas mixture. The advantage of this approach is its high flexibility. Extensions such as multi temperature models to handle thermal non-equilibrium effects are easily possible. Having determined the mixture composition and the thermodynamic state of the individual species, the properties of the reacting gas mixture are then computed using suitable mixture rules such as proposed by Wilke [95] for the viscosity and by Herning and Zipperer [35] for the heat conductivity.

For fully catalytic wall boundaries, a Dirichlet condition for the species mass fractions is set according to the local equilibrium composition. Non-catalytic walls are modeled using a von Neumann boundary condition imposing vanishing wall-normal gradients of the species mass fractions.

The species diffusion fluxes are modeled using Fick's law applying an averaged diffusion coefficient for all species. This approximate diffusion coefficient is computed using the mixture viscosity and constant laminar Schmidt numbers, *Sc*. Turbulent diffusion is modeled in an analog way by computing a turbulent diffusion coefficient, $D_T$, from the eddy viscosity, $\mu_T$, and the turbulent Schmidt number, $Sc_T$. The eddy viscosity is derived from the applied turbulence model (e.g. computed from the turbulent kinetic energy and the length scale when applying a $k$-$\omega$ model).

Thermal non-equilibrium flows are computed by solving an additional transport equation for the vibrational energy of each molecule in non-equilibrium. The relaxation of vibrational energy is modeled according to the Landau-Teller [47] approach and the vibrational relexation times are obtained from the correlation of Millikan and White [61].

An assumed Probability-Density-Function (PDF) model as described by Gerlinger [24] is implemented to model the influence of turbulent fluctuations on the species source terms for detailed chemistry mechanisms. Point statistical PDF methods in conjunction with a detailed chemistry scheme have a very wide range of application and have been successively applied to e.g. turbulent supersonic combustion phenomena (Gerlinger [24], [22], Gaffney [19]). There are no limitations concerning their applicability for premixed and non-premixed combustion and for different Damköhler numbers. The averaged turbulent chemical source term is computed by PDF-weighted integration over the parameter space (temperature, species concentration). Two major approaches can be distinguished: Assumed-PDF methods prescribe the mathematical shapes and the PDF function is usually defined by its 1st and 2nd moments. In the transport equation PDF approach the evolution of the complete PDF function is computed which is computationally much more expensive but offers the advantage of more physical PDF shapes.

### 4.2.1 Navier-Stokes equations of a mixture of reacting gases

The Navier-Stokes equations for a reacting mixture of compressible ideal gases can be written in their integral form as:

$$\frac{\partial}{\partial t}\int_V \underline{U} dV + \int_S \underline{\underline{F}}^{Eu}\,\underline{n} dS = \int_S \underline{\underline{F}}^{NS}\,\underline{n} dS + \int_V \underline{Q} dV \tag{10}$$

The vector of the conservative variables in the case of thermal equilibrium (only one overall energy equation is needed) is:

$$\underline{U} = \left(\rho_S, \rho\underline{u}^T, \rho E\right)^T \tag{11}$$

The matrix of the inviscid (Euler) fluxes is:

$$\underline{\underline{F}}^{Eu} = \begin{bmatrix} \rho_S \underline{u}^T \\ \rho \underline{u}\underline{u}^T \\ \rho E \underline{u}^T \end{bmatrix} + \begin{bmatrix} 0 \\ p\underline{\underline{I}} \\ p\underline{u}^T \end{bmatrix} \tag{12}$$

And the matrix of the viscous (Navier-Stokes) fluxes reads:

$$F^{NS} = \begin{bmatrix} \left(\frac{\mu}{Sc}\right)\underline{\nabla}^T \frac{\rho_S}{\rho} \\ \underline{\underline{P}} \\ \kappa \underline{\nabla}^T T + \left(\frac{\mu}{Sc}\right)\sum_S h_S \underline{\nabla}^T \frac{\rho_S}{\rho} + \left(\underline{\underline{P}}\underline{u}\right)^T \end{bmatrix} \tag{13}$$

Note that the diffusion flux, $\rho_S \underline{u}_S^d$, of species $S$ is modelled using Fick's law and an averaged diffusion coefficient $D$ for all species:

$$\rho_S \underline{u}_S^d = -\rho D \underline{\nabla}\left(\frac{\rho_S}{\rho}\right) = -\left(\frac{\mu}{Sc}\right)\underline{\nabla}\frac{\rho_S}{\rho} \tag{14}$$

This approximate diffusion coefficient is computed using the viscosity and a constant Schmidt number, $Sc$. The viscous stress tensor, $\underline{\underline{P}}$, is modelled using the Boussinesq approximation:

$$\underline{\underline{P}} = \mu\left[\underline{\nabla}\underline{u}^T + \left(\underline{\nabla}\underline{u}^T\right)^T\right] - \frac{2}{3}\mu\left(\underline{\nabla}^T \underline{u}\right)\underline{\underline{I}} \tag{15}$$

The source vector $\underline{Q}$ includes the chemical source term $\omega_S$:

$$\underline{Q} = \begin{bmatrix} \omega_S \\ \underline{0} \\ 0 \end{bmatrix} \tag{16}$$

### 4.2.2 Computation of the chemical source term

In addition to solving the set of transport equations that describe the evolution of the different species $S$ in the reacting flow field, the computation of the chemical source term which determines the rate of production or destruction of a species due to chemical reactions is a key part of the reacting flow model. Chemical sources $\omega_s$ are produced by sets of chemical reactions involving the species $X_S$ and the stoichiometric coefficients $\alpha_S$ and $\beta_S$:

$$\sum_S \alpha_S^r X_S \xleftrightarrow[k_r^f ; k_r^b]{} \sum_S \beta_S^r X_S \tag{17}$$

The source term $\omega_s$ can be computed from the law of mass action by summation over all participating reactions:

$$\omega_S = M_S \sum_r \left(\beta_S^r - \alpha_S^r\right)\left[k_r^f \prod_S \left(n_S\right)^{\alpha_S^r} - k_r^b \prod_S \left(n_S\right)^{\beta_S^r}\right] \tag{18}$$

The forward reaction rate is obtained from the modified Arrhenius law:

$$k_r^f = \left(a_r^f\right)\left(\frac{T}{1\mathrm{K}}\right)^{b_r^f} \exp\left(-\frac{c_r^f}{T}\right) \tag{19}$$

The reaction rate of the backward reaction is obtained from the equilibrium constant:

$$k_r^b = \frac{k_r^f}{K_r^{eq}} \tag{20}$$

The equilibrium constant can be directly computed from the partition functions of the participating species:

$$K_r^{eq} = \prod_S \left(\frac{Q_S}{VN_A}\right)^{\beta_S^r - \alpha_S^r} \tag{21}$$

### 4.2.3 Thermodynamic properties and partition functions

The calculation of the thermodynamic properties and equilibrium constants for the individual chemical reactions is based on either partition functions or external lookup tables. The partition function approach facilitates the application of multi temperature models to account for thermal non-equilibrium.

If the assumption of a harmonic oscillator and rigid rotator with no interdependencies between the energy modes is made, the partition function of a species, *S*, can be written as the product of the individual translational, rotational, vibrational, electronic and zero point contributions:

$$Q_S = Q_S^t Q_S^{rot} Q_S^{vib} Q_S^e Q_S^0 \tag{22}$$

The translational partition function reads:

$$Q_S^t = \left(\frac{2\pi M_S kT}{N_A h^2}\right)^{\frac{3}{2}} V \tag{23}$$

The electronic partition function is computed by summing up the contribution from each excited state:

$$Q_S^e = \sum_m g_{S,m}^e \exp\left(-\frac{\theta_{S,m}^e}{T}\right) \tag{24}$$

The zero point partition function is given by:

$$Q_S^0 = \exp\left(-\frac{\theta_s^0}{T}\right) \tag{25}$$

The rotational partition function for rigid rotation of a linear molecule ($N_2$, $H_2$, $O_2$ and OH) is:

$$Q_S^{rot} = \frac{1}{\sigma}\frac{T}{\theta_S^{rot}} \tag{26}$$

The rotational partition functions for nonlinear molecules ($H_2O$, $HO_2$, $H_2O_2$) is given by:

$$Q_S^{rot} = \frac{1}{\sigma}\sqrt{\frac{\pi T^3}{\theta_S^{rot,1}\theta_S^{rot,2}\theta_S^{rot,3}}} \tag{27}$$

The vibrational partition function of the harmonic oscillator is computed from the individual contributions of each mode:

$$Q_S^{vib} = \prod_{v=1}^{n_{VIB}} \frac{1}{1-\exp\left(-\frac{\theta_S^{vib,v}}{T}\right)} \tag{28}$$

The derivation of the relationship between the partition function $Q$ and the thermodynamic properties is straightforward ([1], [91]) and not repeated here. For example, the internal energy is given by:

$$e_S = RT^2 \frac{\partial \ln Q_S}{\partial T}, \tag{29}$$

resulting in:

$$e_S = \frac{3}{2}RT + K_{ROT}\frac{RT}{2} + R\sum_v \frac{\theta_S^{vib,v}}{\exp(\theta_S^{vib,v}/T)-1} + R\frac{\sum_e g_e^{el}\theta_e^{el}\exp(-\theta_e^{el}/T)}{\sum_e g_e^{el}\exp(-\theta_e^{el}/T)} \tag{30}$$

With $K_{ROT}$ expressing the number of rotational degrees of freedom (=2 for linear molecules and 3 for the nonlinear ones).

The specific heat at constant volume of species S is given by:

$$c_{V,S} = \frac{de_S}{dT}, \tag{31}$$

resulting in:

$$\begin{aligned} c_{V,S} &= \frac{3}{2}R + \frac{K_{ROT}}{2}R + R\sum_v \left(\frac{\theta_S^{vib,v}/2T}{\sinh(\theta_S^{vib,v}/2T)}\right)^2 + c_V^{el} \\ c_V^{el} &= \frac{R}{T^2}\frac{\sum_e g_e^{el}\left(\theta_e^{el}\right)^2\exp(-\theta_e^{el}/T)}{\sum_e g_e^{el}\exp(-\theta_e^{el}/T)} - \frac{R}{T^2}\left(\frac{\sum_e g_e^{el}\theta_e^{el}\exp(-\theta_e^{el}/T)}{\sum_e g_e^{el}\exp(-\theta_e^{el}/T)}\right)^2 \end{aligned} \tag{32}$$

Finally, the entropy can be expressed as:

$$s_S = R\left(1+\ln\frac{kQ}{R}\right)+RT\frac{\partial \ln Q}{\partial T} \tag{33}$$

The energy, entropy or specific heat of the mixture is obtained by the mass fraction weighted average:

$$\Phi = \sum_S Y_S \Phi_S \tag{34}$$

### 4.2.4 Laminar transport coefficients

The laminar viscosity of each individual species is calculated using the curve fits given by Blottner [26]:

$$\mu_S = 1\frac{\mathrm{Ns}}{\mathrm{m}^2}\exp(C_S)T^{(A_S\ln(T)+B_S)} \tag{35}$$

The laminar viscosity of the gas mixture is subsequently computed using the mixture rule of Wilke [95] which is suitable for reacting gas mixtures without ionisation [64], [6]:

$$\mu = \sum_S \frac{n_S\mu_S}{\sum_s n_S\Phi_{S,s}} \;;\; \text{where } \Phi_{S,s} = \frac{1}{\sqrt{8}}\left(1+\frac{M_S}{M_s}\right)^{-\frac{1}{2}}\left[1+\left(\frac{\mu_S}{\mu_s}\right)^{\frac{1}{2}}\left(\frac{M_s}{M_S}\right)^{\frac{1}{4}}\right]^2 \tag{36}$$

The thermal conductivity of the individual species is computed by the Eucken correction utilizing the modified version of Hirschfelder [16], [36]:

$$\kappa_S = \mu_S\left(\frac{5}{2}(c_V)_S^t + \frac{(c_V)_S^{rot}+(c_V)_S^{vib}+(c_V)_S^e}{Sc}\right) \tag{37}$$

The heat conductivity of the mixture is computed using the mixture rule of Herning and Zipperer [35]:

$$\kappa = \sum_S \frac{n_S\kappa_S}{\Phi_S} \;;\; \text{where } \Phi_S = \sum_s n_s\sqrt{\frac{M_s}{M_S}} \tag{38}$$

### 4.2.5 Turbulence modelling and Favre averaged conservation equations

Turbulent boundary and shear layers are present in flows which are characterized by large Reynolds numbers. The modelling of turbulent flows is a crucial part of the CFD analysis of many reacting high enthalpy flow problems of practical interest. Because of the complex modelling needed to account for the chemistry and thermodynamics, the application of advanced turbulence modelling strategies such as large or detached eddy simulation result in very time consuming computations which are currently not feasible for design applications or comprehensive parametric studies. One and two equation eddy viscosity models combined with the Favre averaged conservation equations are well established and represent a method to model turbulent flows in a robust and computationally efficient way. The solution of the resulting set of equations represents a time average of the flow quantities. Turbulent fluctuations are not resolved.

The averaged equations as used in the TAU code can be derived from the laminar or instantaneous set of equations (10) to (16) by applying Reynolds decomposition to the total and partial densities and Favre decomposition to the remaining flow variables:

$$\rho = \bar{\rho} + \rho', \ \bar{\rho} = \frac{1}{\Delta t}\int_{t_0}^{t_0+\Delta t} \rho(t)\,\mathrm{d}t\,, \tag{39}$$

where $\bar{\rho}$ is the Reynolds average in the time domain of the density, $\rho$, and $\rho'$ is the fluctuating component of $\rho$.

The Favre decomposition of the remaining flow quantities $\phi = (u, E, h, T)$ uses a density weighted average in the time domain:

$$\phi = \tilde{\phi} + \phi'', \ \tilde{\phi} = \frac{1}{\bar{\rho}\Delta t}\int_{t_0}^{t_0+\Delta t} \rho(t)\phi(t)\,\mathrm{d}t \tag{40}$$

The integration time, $\Delta t$, must be significantly larger than the largest characteristic time of the considered fluctuating turbulent structures [94]. If this is not the case, the solution of the averaged equations is not unique and becomes dependant on $\Delta t$ [23]. The treatment of unsteady flows (URANS) therefore requires that the characteristic time scale of the bulk flow is sufficiently larger than the characteristic time scales of the turbulent fluctuations.

The substitution of the decompositions (39) and (40) in the laminar or instantaneous set of conservation equations (10) to (16), results in the Favre averaged conservation equations for compressible, turbulent flows. The turbulent set of equations then contains first (e.g. $\tilde{u}_i$), second (e.g. $\overline{\rho u_i'' u_j''}$) and third (e.g. $\overline{\rho u_i'' u_j'' u_j''}$) moments of the decomposed fluctuating flow quantities. The derivation of transport equations for the additional terms and their introduction into the conservation equations would result in the generation of further unknowns [94]. Therefore, additional turbulence modelling is needed to close the averaged system of conservation equations. The basis of Boussinesq turbulence models is the introduction of an additional eddy viscosity, $\mu_t$, which is computed from auxiliary model equations. This eddy viscosity is used to model the a-priory unknown higher moments of the decomposed flow quantities.

- Species conservation equations: Turbulence increases the species diffusion velocities which are modelled by simply adding the turbulent contribution to the laminar diffusion coefficient:

$$\rho_S \underline{u}_S^d = -\rho D \underline{\nabla}\left(\frac{\rho_S}{\rho}\right) = -\left(\frac{\mu}{Sc} - \frac{\mu_T}{Sc_T}\right)\underline{\nabla}\frac{\rho_S}{\rho} \tag{41}$$

- Momentum equations: The second moments which are introduced by the averaging procedure ($\overline{\rho u_i'' u_j''}$) act as an additional turbulent stress tensor (Reynolds stress tensor) which is modelled using the Boussinesq hypothesis ($k$ is the turbulent energy, the last term represents an increase of the effective static pressure due to the presence of turbulent fluctuations and is neglected for the application of the Spalart-Allmaras one equation turbulence model):

$$\underline{\underline{P_T}} = \mu_T\left(\left[\underline{\nabla}\underline{u}^T + \left(\underline{\nabla}\underline{u}^T\right)^T\right] - \frac{2}{3}\left(\underline{\nabla}^T\underline{u}\right)\underline{\underline{I}}\right) - \frac{2}{3}\bar{\rho}k\underline{\underline{I}} \tag{42}$$

- Energy equation: The definition of the total energy changes due to the additional contribution resulting from the turbulence to: $\tilde{E} = \tilde{e} + 0.5\tilde{\underline{u}}\cdot\tilde{\underline{u}} + k$. The turbulent species diffusion is modeled according to equation (41) and the turbulent heat conductivity is computed assuming a ratio of laminar to turbulent Prandtl numbers of $\mathrm{Pr}/\mathrm{Pr}_T = 0.8$ using:

$$\kappa_T = \frac{\mathrm{Pr}}{\mathrm{Pr}_T}\frac{\mu_T}{\mu}\kappa \tag{43}$$

Introducing the additional modeled turbulent contributions from equations (41) to (43) into the laminar set of equations (10) to (16), leads to the modeled Favre averaged set of conservation equations.

The structure of the Navier Stokes equations in their integral form remains unchanged:

$$\frac{\partial}{\partial t}\int_V \underline{U}dV + \int_S \underline{\underline{F}}^{Eu}\underline{n}dS = \int_S \underline{\underline{F}}^{NS}\underline{n}dS + \int_V \underline{Q}dV \tag{44}$$

The vector of conservative variables now contains the averaged quantities:

$$\underline{U} = \left(\bar{\rho}_S, \bar{\rho}\underline{\tilde{u}}^T, \bar{\rho}\tilde{E}\right)^T \tag{45}$$

The matrix of the inviscid fluxes remains unchanged:

$$\underline{\underline{F}}^{Eu} = \begin{bmatrix} \bar{\rho}_S\underline{\tilde{u}}^T \\ \bar{\rho}\underline{\tilde{u}}\underline{\tilde{u}}^T \\ \bar{\rho}\tilde{E}\underline{\tilde{u}}^T \end{bmatrix} + \begin{bmatrix} 0 \\ \bar{p}\underline{\underline{I}} \\ \bar{p}\underline{\tilde{u}}^T \end{bmatrix} \tag{46}$$

The matrix of the viscous fluxes now contains the additional Reynolds stresses and contributions from the turbulent diffusion and heat conduction. Note that for practical computations the last term of the approximation of the Reynolds stress tensor (42) is added to the static pressure: $\bar{p}_{eff} = \bar{p} + 2/3\bar{\rho}k$ and is therefore treated as an inviscid flux contribution.

$$\underline{\underline{F}}^{NS} = \begin{bmatrix} \left(\frac{\mu}{Sc} + \frac{\mu_T}{Sc_T}\right)\underline{\nabla}^T\frac{\bar{\rho}_S}{\bar{\rho}} \\ \underline{\underline{P}} + \underline{\underline{P}}_T \\ \left(\kappa + \kappa_T\right)\underline{\nabla}^T\tilde{T} + \left(\frac{\mu}{Sc} + \frac{\mu_T}{Sc_T}\right)\sum_S \tilde{h}_S\underline{\nabla}^T\frac{\bar{\rho}_S}{\bar{\rho}} + \left(\left(\underline{\underline{P}} + \underline{\underline{P}}_T\right)\underline{\tilde{u}}\right)^T + \sigma_k\left(\mu + \mu_T\right)\underline{\nabla}^T k \end{bmatrix} \tag{47}$$

Here $\sigma_k$ is a constant of the applied two-equation turbulence model and $k$ denotes the turbulent kinetic energy. The source term vector now contains the averaged chemical source term $\bar{\omega}_S$. This can be estimated e.g. using an assumed PDF approach.

$$\underline{Q} = \begin{bmatrix} \bar{\omega}_S \\ \underline{0} \\ 0 \end{bmatrix} \tag{48}$$

The eddy viscosity, $\mu_T$, can be computed using a wide variety of one- and two equation turbulence models.

Many eddy viscosity turbulence models are known to over predict the spreading rate of compressible shear layers above convective Mach numbers of about 0.5 [94]. The convective Mach number, $M_c$, is related to the speed at which large turbulent structures are transported in a shear layer between two parallel flows with velocities $u_1$ and $u_2$ and the speeds of sound $a_1$ and $a_2$:

$$M_c = \frac{u_1 - u_2}{a_1 + a_2} \tag{49}$$

Several shear layer compressibility corrections exist for two-equation eddy viscosity models to remedy this problem. Sarkar et al. [76] and Zeeman [97] postulated corrections which are based on the effects of additional dilatation dissipation and eddy shocklets in highly compressible flow. Later, Vreman et. al [92] pointed out that these effects are not significant even in highly compressible mixing layers. Wilcox [94] constructed a model for shear layer compressibility correction based on an assessment of existing work and empirical considerations which is designed to minimize the adverse effects of the shear layer correction on the prediction of boundary layer flows.

### 4.2.6 Modelling of flows in thermal non-equilibrium

The numerical analysis of e.g. strongly expanding flows in nozzles of hypersonic high enthalpy test facilities requires the modeling of thermal non-equilibrium and the resulting freezing of the vibrational relaxation process of the molecules in the flow field. This is achieved in TAU by considering an additional transport equation for the vibrational energy of each molecule to be considered in thermal non-equilibrium ($N_2$, $O_2$, NO for air flows). In accordance with the nomenclature of equation (44), the additional fluxes and source terms can be written as:

$$\underline{\underline{F}}^{Eu} = \left[ \bar{\rho} e_S^{vib} \tilde{\underline{u}}^T \right], \quad \underline{\underline{F}}^{NS} = \left[ \kappa^{vib} \underline{\nabla}^T T_S^{vib} + \left( \frac{\mu}{Sc} + \frac{\mu_T}{Sc_T} \right) \varepsilon_S^{vib} \underline{\nabla}^T \frac{\rho_S}{\rho} \right], \quad \underline{Q} = \left[ \Omega_S^{vib,t} + \varepsilon_S^{vib} \omega_S \right] \tag{50}$$

Further, the viscous transport of vibrational energy by conduction has to be considered in the computation of the viscous fluxes in the transport equation of the total energy (47):

$$\underline{\underline{F}}^{NS}_{total\ energy} = \left[ \left( \kappa + \kappa_T \right) \underline{\nabla}^T \tilde{T} + \left( \frac{\mu}{Sc} + \frac{\mu_T}{Sc_T} \right) \sum_S \tilde{h}_S \underline{\nabla}^T \frac{\bar{\rho}_S}{\bar{\rho}} + \left( \left( \underline{\underline{P}} + \underline{\underline{P}}_T \right) \tilde{\underline{u}} \right)^T + \sum_S \kappa_S^{vib} \underline{\nabla}^T T_S^{vib} \right] \tag{51}$$

The mixture specific vibrational energy of a species, $e_S^{vib}$, can be computed from the specific vibrational energy using:

$$\bar{\rho} e_S^{vib} = \bar{\rho}_S \varepsilon_S^{vib} \tag{52}$$

The vibrational temperature, $T_S^{vib}$, is related to the vibrational energy e.g. through the set of equations (22) to (33) defining the species partition functions. The vibrational heat conductivity, $\kappa_S^{vib}$, is computed using the modified Eucken correction and applying turbulence and mixing rule factors similar those given in equations (53) and (54):

$$\kappa_S^{vib} = \left( 1 + \frac{\mathrm{Pr}}{\mathrm{Pr}_T} \frac{\mu_T}{\mu} \right) \frac{n_S}{\phi_S} \frac{(c_V)_S^{vib}}{Sc} \mu_S \tag{55}$$

The source term of the vibrational energy equations consists of the chemical contribution ($\varepsilon_S^{vib} \omega_S$) and the contribution from the vibration-translation relaxation ($\Omega_S^{vib,t}$).

The vibration-translation relaxation term, $\Omega_S^{vib,t}$, is computed using the Landau-Teller approach with the equilibrium energy set to the vibrational energy at the translational temperature, $T$:

$$\Omega_S^{vib,t} = \frac{\rho_S \varepsilon_S^{vib}(T) - \rho e_S^{vib}}{\langle \tau_S \rangle}, \quad \frac{1}{\langle \tau_S \rangle} = \sum_s \frac{1}{\tau_{S,s}} \tag{56}$$

The translation-vibration relaxation times of different pairs of species *s,S* are computed using the empirical relation of Millikan and White:

$$\begin{aligned} \tau_{S,s} &= \frac{1\text{Pa}1\text{s}}{p_S} \exp\left[ A_{S,s} \left( \left( \frac{T}{1\text{K}} \right)^{-1/3} - 0.84 \mu_{S,s}^{1/4} \right) - 6.894 \right] \\ A_{S,s} &= 0.0367 \mu_{S,s}^{1/2} \left( \frac{\theta_S^v}{1\text{K}} \right)^{4/3}, \quad \mu_{S,s} = \frac{M_S M_s}{M_S + M_s} \frac{1\text{mol}}{1\text{kg}} \end{aligned} \tag{57}$$

### 4.2.7 Modelling of weakly ionized flows

The assumptions of an independent harmonic oscillator and rigid rotator which are made for the calculation of the partition function of molecules are often questionable at large temperature levels. Improved modeling of the thermodynamic properties of molecular species can be achieved by considering a full coupling of the rotational, vibrational and electronic excitation as well as anharmonicity effects. A detailed description of this approach is given e.g. in reference [6]. Exemplary, the internal partition function of a diatomic molecule can be expressed as:

$$\begin{aligned} Q_{\text{int}} &= \sum_e g_e \exp\left(-\theta_e / T\right) \frac{T}{\sigma \theta_R} \frac{1}{1 - \exp\left(-\theta_v / T\right)} \\ &\times \left[ 1 + \frac{\theta_R}{3T} + \frac{\theta_R^2}{15T^2} + \frac{2D_e T}{B_0 \theta_R} + \frac{\alpha_e}{B_0 \left(1 - \exp\left(\theta_v / T\right)\right)} + \frac{x_0 \theta_v / T}{\left(\exp\left(\theta_v / T\right) - 1\right)^2} \right] \end{aligned} \tag{58}$$

The first terms in equation (58) are the harmonic contributions of the electronic, rotational and vibrational partition functions with the characteristic temperatures $\theta_e$, $\theta_R$ and $\theta_v$. The last term models the coupling between the internal energy modes and involves the additional coupling constants $\alpha_e$, $x_0$ and $B_0$. If polyatomic molecules are considered, the rotational term has to be modified and further vibrational terms for each additional vibrational mode have to be added (see e.g. Gurvich [27]).

Concerning the computation of transport coefficients, the Yos mixture rule is generally considered to be more accurate than the Wilke rule for high temperatures and the presence of ionizes species. It is an approximation of the Chapman-Enskog expansion for the transport coefficient which neglects off-diagonal terms (details and derivation in ref. [6]). Different relations exist for the viscosity and the translational and internal thermal conductivities. The computation procedure for the viscosity is repeated here from [6] as an illustrative example (*x* are the species mole fractions):

$$\mu = \frac{\sum_{i=1}^{species} \frac{x_i}{A_i + a_{av}}}{1 - a_{av} \sum_{i=1}^{species} \frac{x_i}{A_i + a_{av}}} \quad , \quad a_{av} = \frac{\sum_{i=1}^{species} \sum_{j=1}^{species} x_i x_j \left( \frac{1}{A_i} - \frac{1}{A_j} \right)^2 a_{ij}}{\sum_{i=1}^{species} \sum_{j=1}^{species} x_i x_j \left( \frac{1}{A_i} - \frac{1}{A_j} \right)^2} \tag{59}$$

$$a_{ij} = \frac{N_A}{M_i + M_j}\left(2\Delta_{ij}^{(1)} - \Delta_{ij}^{(2)}\right) \quad , \quad A_i = \sum_{j=1}^{species} x_j \frac{N_A}{M_i}\Delta_{ij}^{(2)} \tag{60}$$

$$\Delta_{ij}^{(1)} = \frac{8}{3}\Omega_{ij}^{(1,1)}\sqrt{\frac{2M_iM_j}{\pi RT(M_i+M_j)}} \quad , \quad \Delta_{ij}^{(2)} = \frac{16}{5}\Omega_{ij}^{(2,2)}\sqrt{\frac{2M_iM_j}{\pi RT(M_i+M_j)}} \tag{61}$$

The binary collision integrals in the set of equations (59) to (61) are obtained from curve fits. For neutral particles the curve fit function is given in equation (62):

$$\ln\Omega^* = D + \left(A\ln^2 T + B\ln T + C\right)\ln T \tag{62}$$

The coefficients *A*, *B*, *C* and *D* are needed for each pair of species (*ij*). Hence, the procurement of the required input data (especially for a large number of species) is significantly more complex than for the Wilke / Blottner approach.

The application of Fick's law to high temperature gas mixtures involving free electrons and ionized species leads often to inaccurate results for the diffusive mass fluxes. Ramshaw and Chang [69], [70] developed an appropriate ambipolar diffusion model for ionized mixtures. It was demonstrated in [25] that for re-entry applications this "Self Consistent Effective Binary Diffusion Method" (SCEBDM) leads to similar results as the solution of the full Stefan-Maxwell equations.

The diffusive mass flux of species *S* is computed according to:

$$J_S = \rho_S u_S^d = \begin{cases} -cM_S D_{Sm}\nabla\left(\frac{\rho_S}{M_S c}\right) + \left(\frac{\rho_S c}{\rho}\right)\sum_{j\neq e} M_j D_{jm}\nabla\left(\frac{\rho_j}{M_j c}\right) + A_S & \text{for } S \neq e \\ -\left(\frac{1}{q_e}\right)\sum_{j\neq e} q_j J_j & \text{for } S = e \end{cases} \tag{63}$$

$$A_S = \left(\frac{c}{q_e\rho_e}\right)\left[M_S q_S \rho_S D_{Sm} - \frac{\rho_S}{\rho}\sum_{j\neq e} M_j q_j \rho_j D_{jm}\right]\nabla\frac{\rho_e}{M_e c}$$

where *c* is the total molar concentration of the mixture and *q* are the species charges. The effective diffusion coefficient $D_{jm}$ for species *j* is computed from the set of binary diffusion coefficients $D_{ji}$ using:

$$D_{jm} = \left(1 - x_i\right) \Big/ \sum_{j=1,\, j\neq i}^{species} \frac{x_i}{D_{ij}} \tag{64}$$

### 4.2.8 Numerical solution procedure, applied spatial and temporal discretization schemes

The spatial discretization used in the TAU code is based on a cell-vertex scheme. The primary computational grid consists of tetrahedra, prisms, hexahedra and pyramids. The flow quantities are stored on the vertices of the primary grid. For the finite volume discretization, a dual grid cell is constructed around each vertex of the primary grid. A schematic of this arrangement is shown in Figure 24.

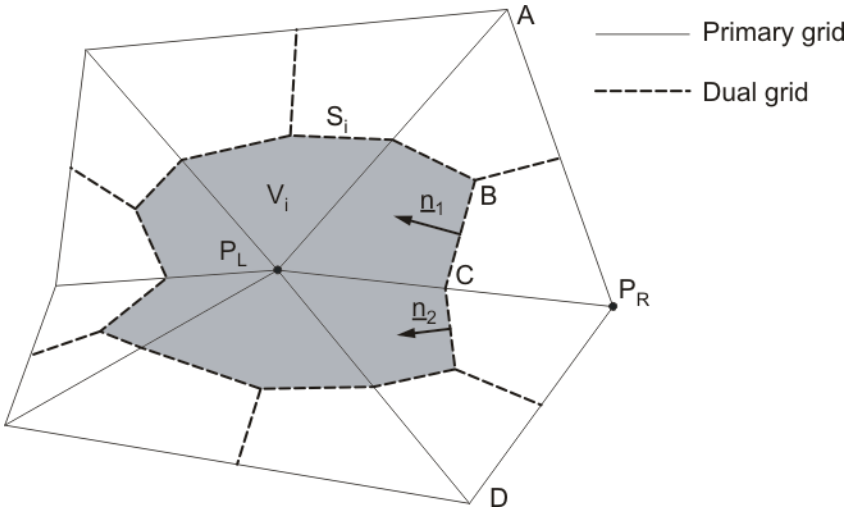


**Figure 24: Schematic of the dual cell structure applied for the spatial discretization in TAU**

The dual cell with volume, $V_i$, and surface, $S_i$, which is constructed around point $P_L$ in Figure 24 is marked in grey. The faces between two adjacent volumes are characterized by their normal vectors. They are grouped such that one face is always associated to two adjacent points in the primary grid. For the example in Figure 24, the normal vector, $\underline{n}$, of the face which connects the dual cells around the points $P_L$ and $P_R$ is computed from its components using:

$$\underline{n} = \underline{n}_1 + \underline{n}_2 \tag{65}$$

The boundary of the dual grid cells is constructed by connecting the centres of the primary grid cells (e.g. point *B*) with the centres of the primary grid faces (e.g. point *C*). The centres of the primary grid cells are derived from a weighted average of the vertices. For the two-dimensional example in Figure 24 the coordinates of point *B* are computed using:

$$\underline{B} = \frac{w_1 \underline{P}_L + w_2 \underline{A} + w_3 \underline{P}_R}{w_1 + w_2 + w_3} \tag{66}$$

The weighting functions represent the sum of the squared face areas or side lengths which are adjacent to a vertex point, i.e.:

$$w_1 = \left(\overline{P_L P_R}\right)^2 + \left(\overline{P_L A}\right)^2 \tag{67}$$

Subsequently, the discretized form of the set of conservation equations (44) can be written as:

$$\frac{\partial}{\partial t}\int_V \underline{U} dV := V \frac{\partial}{\partial t}\underline{U} \;,\; \int_{\partial V} \underline{\underline{F}}^{Eu/NS} \underline{n} dS := \sum_i \underline{\underline{F}}_i^{Eu/NS} n_i \;,\; \int_V \underline{Q} dV := \underline{Q} V \tag{68}$$

The discretized conservation equations for one control volume with the face segments, *i*, in the final form introducing the residual, *R*, are:

$$\frac{\mathrm{d}}{\mathrm{d}t}\underline{U} = -\underline{R}$$
$$\underline{R} = \frac{1}{V}\left(\sum_i \underline{\underline{F}}_i^{Eu}\,\underline{n}_i - \sum_i \underline{\underline{F}}_i^{NS}\,\underline{n}_i - \underline{Q}V\right) \tag{69}$$

The actual computation of the inviscid flux vector, $\underline{\underline{F}}_i^{Eu}\,\underline{n}_i$, across a cell face, *i*, is done using a variety of upwind or central schemes.

To increase the accuracy of the upwind discretization to second order in space, the flow quantities at the left and right side of each face, $\phi_L$ and $\phi_R$, are extrapolated assuming a piecewise linear distribution using:

$$\phi_L^{face} = \phi_L^{node} + \frac{1}{2}L\underline{\nabla}\phi_L\left(\underline{x}_R - \underline{x}_L\right)$$
$$\phi_R^{face} = \phi_R^{node} + \frac{1}{2}L\underline{\nabla}\phi_R\left(\underline{x}_L - \underline{x}_R\right) \tag{70}$$

The vectors $\underline{x}_L$ and $\underline{x}_R$ represent the coordinates of the dual cell centres of two adjacent volumes (points $P_L$ and $P_R$ in Figure 24). The limiter function, *L*, is introduced to prevent overshoots of the reconstructed quantities due to the presence of discontinuities. In the unstructured regions of the grid the Barth-Jespersen limiter [3] is used.

The gradients of the flow quantities which are needed for the piecewise linear reconstruction to achieve second order accuracy in space for the upwind discretization and for the computation of the viscous fluxes are computed using a least-square fitting approach as described by Anderson [2] and Haselbacher [34]. The flow quantities at the grid points surrounding the cell for which the gradients are to be computed are approximated using a second order Taylor expansion and the gradients in this expansion are chosen such that the resulting estimate provides an optimum least-square fit to the actual computed cell averages. In structured regions with aligned cells of large aspect ratio (e.g. meshes close to viscous walls consisting of hexahedra and prisms) the cell boundaries form grid lines with minor change of direction. Those lines are identified and the gradients along these grid lines are computed using a second order finite difference approach. The van-Leer limiter [88] is used for the correction of these gradients.

The viscous flux vector, $\underline{\underline{F}}_i^{NS}\,\underline{n}_i$, across a cell face, *i*, is computed according to the equations given above (e.g. equation (47) for the viscous fluxes in the continuity, momentum and total energy equation). The flow quantities, ϕ, and the gradients of the flow quantities, ∇ϕ, at the cell faces which are needed in these equations (see also Figure 24) are computed from the averaged quantities of the dual grid cells adjacent to the considered face using a central scheme:

$$\phi^{face} = \frac{1}{2}\left(\phi_L + \phi_R\right),\ \underline{\nabla}\phi^{face} = \frac{1}{2}\left(\underline{\nabla}\phi_L + \underline{\nabla}\phi_R\right) \tag{71}$$

The accuracy of the gradient reconstruction for the computation of the viscous fluxes is improved by applying the following correction procedure:

$$\underline{\nabla}\phi^{face,corrected} = \underline{\nabla}\phi^{face} + \left(\frac{\phi_L - \phi_R}{\left|\underline{\Delta x}_{LR}\right|} - \frac{\underline{\nabla}\phi^{face}\,\underline{\Delta x}_{LR}}{\left|\underline{\Delta x}_{LR}\right|}\right)\frac{\underline{\Delta x}_{LR}}{\left|\underline{\Delta x}_{LR}\right|}, \tag{72}$$

with $\underline{\Delta x}_{LR}$ denoting the spatial difference vector between the left and right dual cell centres belonging to the face at which the gradient needs to be evaluated. This procedure corrects the component of the vector

tangential to the spatial difference vector to the central difference value while preserving the normal components.

To enhance the convergence rate of the iterative solution of equation (69), explicit smoothing of the residuals or multigrid schemes can be applied.

Temporal discretization of equation (69) is achieved by applying multi-stage Runge Kutta schemes as described e.g. by Jameson et al. [40] or an implicit approximate factorization scheme (Lower-Upper Symmetric Gauss-Seidel). For steady state problems, equation (69) reduces to $R$=0 because $\mathrm{d}\underline{U}/\mathrm{d}t$ vanishes. The iterative solution is performed in a pseudo time, $t$*:

$$\frac{\mathrm{d}\underline{U}}{\mathrm{d}t^*} + \underline{R} = 0 \tag{73}$$

When explicit Runge-Kutta time integration is applied, the computation of the chemical source term vector is done in a point implicit manner as described by Sheffer [80]. The vector of the chemical sources is linearized to obtain an estimate for the new time step ($n$+1):

$$\underline{Q}^{n+1} \approx \underline{Q}^{n} + \frac{\partial \underline{Q}^{n}}{\partial \underline{U}} \frac{d}{dt} \underline{U} \Delta t^* \tag{74}$$

Substitution into the governing equation yields:

$$\frac{\partial}{\partial t}\int_V \underline{U} dV = \left[ \underline{\underline{I}} - \Delta t^* \frac{\partial \underline{Q}^{n}}{\partial \underline{U}} \right]^{-1} \left[ \int_S \underline{\underline{F}}^{Eu} \underline{n} dS + \int_S \underline{\underline{F}}^{NS} \underline{n} dS + \int_V \underline{Q} dV \right], \tag{75}$$

which is evaluated entirely at the current time level and is thus fully explicit. This treatment necessitates the inversion of the source term Jacobian matrix with dimension $N$x$N$ where $N$ is the number of species. The dependency of the source term on the temperature is neglected and no stability penalties from this approximation are observed.

Time accurate computations are performed using a dual-time stepping technique as described by Jameson [39]. The computational time span [0; $t$] is subdivided into intervals $\Delta t$ ("physical time step"). The application of second order backward differencing in time to the vector of conservative variables in equation (69) yields:

$$\frac{3\underline{U}^{n+1}}{2\Delta t} - \frac{2\underline{U}^{n}}{\Delta t} + \frac{\underline{U}^{n-1}}{2\Delta t} = -\underline{R} \tag{76}$$

If the solutions at the time steps $n$ and $n$-1 are known, equation (76) can be rearranged to:

$$\begin{aligned} &\frac{\mathrm{d}\underline{U}^{n+1}}{\mathrm{d}t^*} + \underline{R}^{dual} = 0 \\ &R^{dual} = R^{n+1} + \frac{3\underline{U}^{n+1}}{2\Delta t} - \frac{2\underline{U}^{n}}{\Delta t} + \frac{\underline{U}^{n-1}}{2\Delta t} \end{aligned} \tag{77}$$

The standard solution procedure for steady state problems including all means for convergence acceleration can then be used to solve equation (77) in pseudo time, $t$*, to advance the solution to the physical time step $n$+1.

The computational time step, $\Delta t^*$, is computed locally for each cell ("local time stepping") using the minimum of the convective and viscous time steps:

$$\Delta t^* = \min\left(\Delta t^c\,,\,\Delta t^v\right) \tag{78}$$

Both time steps are determined by adding the contributions from the respective convective and viscous Eigenvalues from all cell faces, *i*.

$$\Delta t^c = CFL \cdot 2V \frac{1}{\sum_i \lambda_c^i}\;,\;\; \Delta t^v = CFL \cdot 2V^2 \frac{1}{4} \frac{1}{\sum_i \lambda_v^i} \tag{79}$$

The contribution from the maximum convective Eigenvalue evaluated at each cell face, *i*, is:

$$\lambda_c^i = \underline{u}_i \underline{n}_i + a_i \left|\underline{n}_i\right| \tag{80}$$

The contribution from the viscous Eigenvalues is estimated as:

$$\lambda_v^i = \left(\lambda_{v1}^i + \lambda_{v2}^i\right)\left|n_i\right|^2 \tag{81}$$

The Eigenvalues $\lambda_{v1}$ and $\lambda_{v1}$ correspond to the contributions from viscous momentum transport and the heat conductivity:

$$\lambda_{v1}^i = \frac{4}{3}\left(\frac{\mu + \mu_T}{\bar{\rho}}\right)\,,\; \lambda_{v2}^i = \frac{c_p}{c_v \bar{\rho}}\left(\frac{\mu}{Pr} + \frac{\mu_T}{Pr_T}\right) \tag{82}$$

The contribution from species diffusion to the viscous time step is neglected because it is usually (for moderate Schmidt numbers greater than 0.6) smaller than the contribution from heat conductivity:

$$\lambda_{v3} = \frac{\mu}{\bar{\rho} Sc} + \frac{\mu_T}{\bar{\rho} Sc_T} < \lambda_{v2} \tag{83}$$

# 5.0 EXAMPLES OF COMBINED EXPERIMENTAL AND NUMERICAL FLOW FIELD INVESTIGATIONS

## 5.1 Calibration of HEG Free Stream Flow

The high enthalpy, high pressure flows generated in free piston driven shock tunnels are well suited for the investigation of chemically reacting flows occurring during the (re-)entry flight of space vehicles or in combustors of hypersonic airbreathing propulsion system. The proper utilisation of such ground based impulse facilities requires a detailed knowledge of the test section flow. However, due to the flow conditions generated in high enthalpy tunnels, the calibration process is much more complex than in cold hypersonic facilities. One reason for this is that the behaviour of the test gas deviates from that of a calorically perfect gas. With increasing total enthalpy, the excitation of internal degrees of freedom such as the vibrational excitation of molecules and subsequently chemical reactions must be considered. Additional difficulties arise from the fact that some parts of the HEG facility, such as the nozzle reservoir, are not accessible with modern optical measurement techniques due to limitations caused by their

structural design. These result from temperatures of up to 10000 K and pressures of up to 2000 bar which are reached at the highest total enthalpy and total pressure conditions. Therefore, the evaluation of the free stream conditions in the test section of the HEG free piston driven shock tunnel is performed by numerical analysis using a suitable set of measured input and reference parameters. The general iterative procedure established to determine HEG free stream conditions is outlined in Figure 25. The numerical determination of the HEG free stream consists of two steps which require a suitable set of input parameters. First, the nozzle reservoir temperature is computed with a one-dimensional analysis of the shock tube. The relevant input parameters are the measured values of the initial shock tube filling pressure and temperature, the shock speed and the nozzle reservoir pressure. Based on these nozzle reservoir conditions, the free stream is subsequently determined by numerical simulation of the nozzle flow.

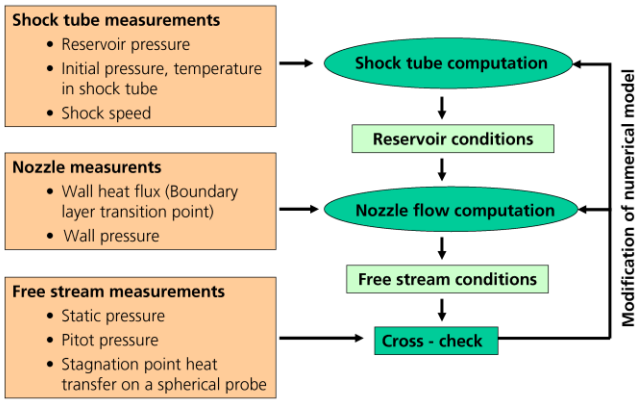


**Figure 25: Combined experimental and numerical iterative procedure to determine HEG free stream conditions**

The close cooperation between experiment and CFD is an interactive process which helps to validate new measurement techniques as well as the physico-chemical model used in the CFD tools such providing step by step an improved understanding of the facility performance. In free piston shock tunnels the available test time is in the order of milliseconds. In order to be able to select the useful test time, the starting process of the nozzle flow and the flow past the model and the arrival of either the expansion wave which reflects off the piston face or the helium driver gas in the test section must be known. In HEG the determination of the test time window - in particular for the high enthalpy conditions - is based on the evaluation of the measured time resolved nozzle reservoir pressure as well as the Pitot pressure and the static pressure in the test section.

### 5.1.1 High Enthalpy Operating Conditions I-IV

For the high enthalpy (12 – 23 MJ/kg) operating conditions of HEG, nozzle 2 is utilised. This conical nozzle has an expansion half-angle of approximately 6.5°, a total length of 3.75 m, a throat radius of 0.011 m and an exit radius of 0.44 m. The area ratio of the nozzle is 1600. The throat section was designed using fourth and third order polynomials in order to obtain a smooth nozzle contour, i.e. a contour whereby the radius as a function of the longitudinal coordinate has continuous first and second derivatives.

The evaluation of the heat transfer measurements along the nozzle wall indicates that a transition region exists between 0.5 - 1.0 m downstream of the nozzle throat [30]. In order to investigate the influence of the location of the transition point on the shape of the computed Pitot pressure profiles at the nozzle exit, the normalised measured and computed Pitot pressure profiles are plotted for operating condition I in Figure 26. It should be noted that these numerical results were obtained using the CEVCATS-N code. The measured Pitot pressure was evaluated in two different test time windows and no significant change of the

shape was found. The computed Pitot pressure profile shapes depend strongly on the modelling of the boundary layer flow. A fully laminar and two turbulent computations with different locations of the laminar-turbulent transition point were performed. For condition I, the best agreement between the measured and computed shape could be obtained when assuming that transition occurs at the downstream end of the transition region found experimentally.

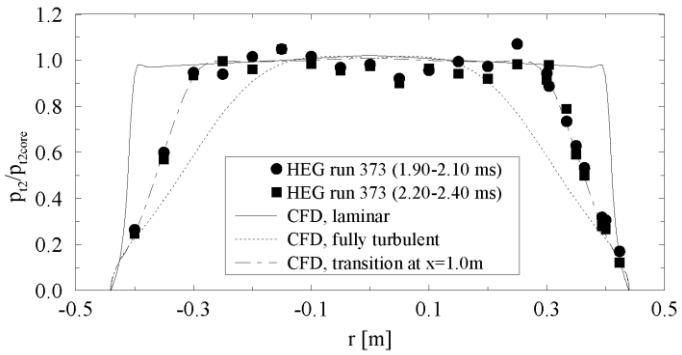


**Figure 26: Comparison between measured and computed Pitot pressure profiles showing the influence of the location of the laminar to turbulent transition point; HEG condition I**

The numerical sensitivity analyses included computations assuming a chemical / thermal nonequilibrium, chemical nonequilibrium / thermal equilibrium and chemical / thermal equilibrium nozzel expansion. The chemical / thermal nonequilibrium computations were additionally performed applying different sets of chemical reaction rates. The chemical / thermal nonequilibrium computation using the reaction rate data given by Park [65] was chosen as the reference computation. Compared to this computation, the results obtained using the reaction rates published by Dunn and Kang [18] and Gupta et al. [26] tend to slow down the chemical relaxation process during the expansion. This results in a reduction of the exit translational temperature by 5% and 23%, respectively (Figure 27).

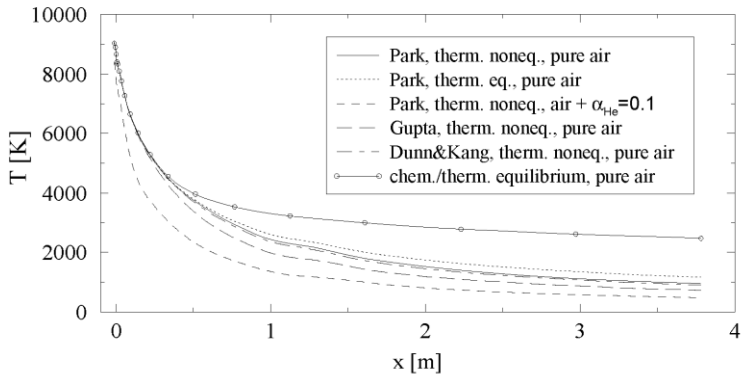


**Figure 27: Sensitivity analysis concerning the computed temperature distribution along the nozzle centerline, HEG condition I; transition location at x=0.75m**

While the Pitot pressure remains approximately constant, the static pressure decreases by 4% and 16% and the density increases by 0.5% and 3.5%. When comparing the chemical / thermal nonequilibrium and the chemical nonequilibrium / thermal equilibrium computations, the exit temperature is increased by 22%, the Pitot pressure is reduced by 4%, the static pressure is increased by 17% and the density is reduced by 5%. This trend is further intensified when comparing the chemical / thermal nonequilibrium computation

with the one assuming an expansion in chemical / thermal equilibrium. Here the temperature is increased by 160%, the Pitot pressure is reduced by 17%, the static pressure is increased by 83% and the density is reduced by 20%.

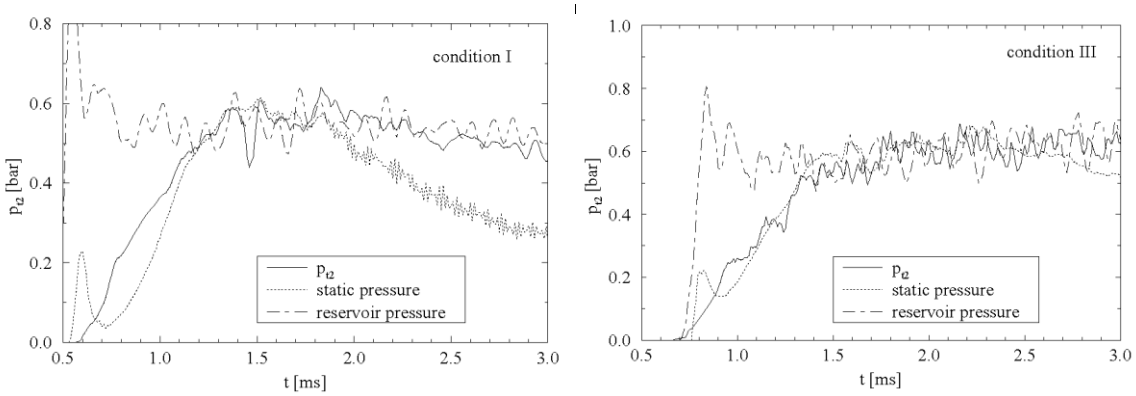


**Figure 28: Temporal development of the reservoir pressure, static pressure and Pitot pressure in the test section for HEG condition I (left) and condition III (right)**

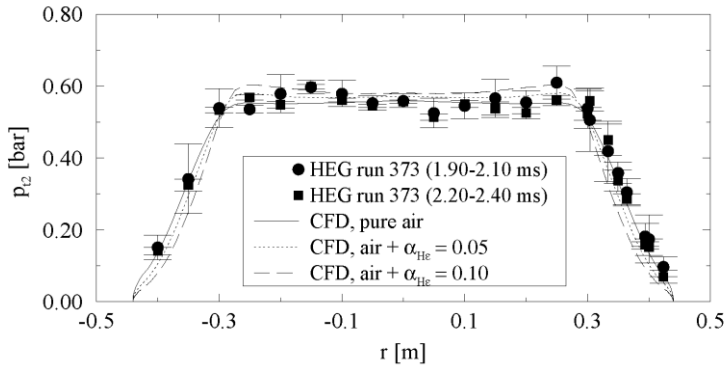


**Figure 29: Comparison of measured and computed Pitot pressure profiles at the nozzle exit. The nozzle flow of pure air as well as of air plus 5% and 10% mass fraction helium was computed; HEG condition I**

The temporal development of the reservoir pressure, the Pitot pressure and the static pressure in the test section for operating conditions I and III are plotted in Figure 28. In order to allow a direct comparison of the temporal development of these three quantities, the reservoir pressure and the static pressure were scaled. Therefore, the unit of the ordinate in Figure 28 is only related to the Pitot pressure signal. The time scale on the abscissa starts when the incident shock in the shock tube reflects off the end wall. The reservoir pressure signal was shifted by approximately 0.5 ms for conditions I and 0.7 ms for conditions III in order to account for the delay of the flow start-up in the test section. A period of time of approximately 1.3 - 1.5 ms is necessary to establish a steady nozzle flow. After the nozzle starting process, the Pitot pressure and static pressure development in the test section is clearly driven by the reservoir pressure. For condition I, however, the static pressure decreases relative to the development of the reservoir pressure and the Pitot pressure after about 1.8 ms. This drop of the static pressure is much less pronounced for condition III. Here it starts after approximately 2.7 ms. For condition IV and condition II (not shown here) this effect can not be observed. One possible explanation of this behaviour could be the arrival of helium driver gas in the test section.

In order to study the effect of driver gas contamination in more detail, steady state nozzle flow computations were performed for condition I using a test gas mixture of air and helium. For these computations a homogeneous mixture of air and helium is used. The nozzle reservoir conditions are determined by assuming that the helium has the same enthalpy as at the end of the compression tube at main diaphragm rupture. This results in approximately the same reservoir enthalpy as given in Table 1. In Figure 29, the computed Pitot pressure profiles at the nozzle exit for pure air, air plus 5% mass fraction helium and air plus 10% mass fraction helium are compared with the measured profiles. The changes of the Pitot pressure profiles due to the addition of helium are small when compared with the fluctuations of the measured data. In contrast to the Pitot pressure, the static pressure is significantly reduced when helium is added to the test gas air. The averaged free stream static pressure at the nozzle exit resulting from nozzle flow computations using pure air and air plus helium is plotted in Figure 30 together with the measured temporal development of the static pressure for different condition I runs. The computed static pressure for pure air agrees well with the measured value at about 1.5 ms, i.e. after the nozzle flow starting process has finished. After a period of time of approximately 0.2 - 0.3 ms the static pressure drops and the addition of helium in the computations has the same effect. A concentration of 5% mass fraction of helium reduces the static pressure by approximately 20%.

The trends provided by the sensitivity analyses, described above, allow to choose the physico-chemical modelling which is best suited to reproduce the whole set of measured data. In general, the best agreement with the experimental data was obtained assuming the nozzle flow to be in chemical nonequilibrium and thermal equilibrium. This assumption is further supported by LIF measurements in HEG which indicate that the vibrational temperature of NO is in equilibrium with the translational / rotational temperature (Wollenhaupt et al. [96]).

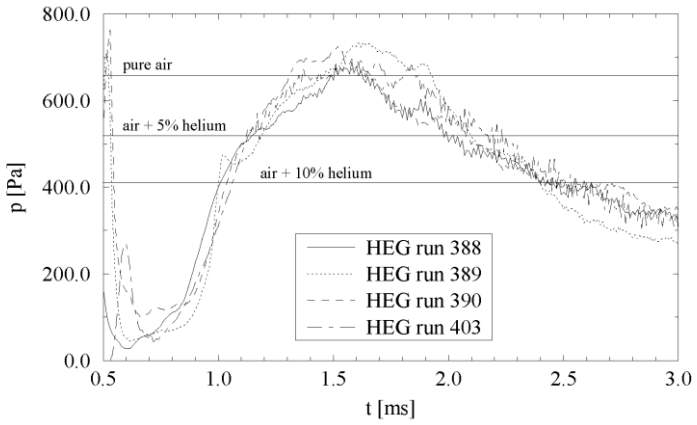


**Figure 30: Comparison between the measured temporal development of static pressure and computed averaged static pressure in the test section core flow resulting from steady state nozzle flow computations using pure air and air plus 5% and 10% mass fraction helium; HEG condition I**

In addition to the computation of test section free stream conditions and comparison with corresponding measurements, the investigation of the flow past basic aerodynamic configurations is well suited to study fundamental aspects of high enthalpy flow fields as well as to validate the facility performance, measurement techniques and CFD codes. A transverse cylinder with a diameter of $D_{cyl}$ = 90 mm was chosen in order to further investigate the influence of early driver gas contamination on the considered flow.

For HEG condition I, computational flow field analyses were first performed. In order to carry out an assessment of the physico-chemical model used in the CFD code, computations were again performed

assuming a chemical nonequilibrium / thermal equilibrium, chemical / thermal nonequilibrium and a frozen flow. For the chemical nonequilibrium computations, the reaction rates of Park, Dunn & Kang and Gupta were again used. The chemical / thermal nonequilibrium computation showed that for HEG condition I the flow reaches a thermal equilibrium state a short distance behind the bow shock. Compared to a chemical nonequilibrium / thermal equilibrium computation, the resulting difference in shock stand-off distance amounts to less than 2% and is, therefore, significantly smaller than the difference obtained by using different chemical models. The computed density distributions along the stagnation streamline in Figure 31 show that the addition of 10% helium also causes a larger shift of the shock stand off distance than obtained by using different chemical models. Clearly, when helium is added, the flow field characteristics change from a nonequilibrium flow with chemical relaxation behind the bow shock, causing an increase of density, towards a frozen flow. As a reference, the density distribution corresponding to a frozen shock layer flow is also shown in Figure 31.

The temporal development of the shock stand-off distance, which was obtained by the evaluation of time resolved shadowgraphs, is plotted in Figure 32 together with the development of the static pressure and the Pitot pressure. The increase of the shock stand-off distance between approximately 1.8 ms and 2.2 ms coincides with the drop of the static pressure. It is interesting to note that for t > 2.8 ms the drop of the static pressure is significantly reduced and the shock stand-off distance remains approximately constant. This would imply that after an initial amount of driver gas has reached the test section, its concentration stays approximately constant and is not continuously increased at the same rate. This observation is consistent with the numerical results of Chue and Eitelberg [12], who computed the transient flow at the end of the HEG shock tube. They found that the interaction of the reflected shock with the contact surface immediately results in a stream of driver gas towards the shock tube end wall. However, further leakage of driver gas is retarded due to vortical structures generated at the contact surface. They conclude that the initial jetting of the driver gas into the test gas is not necessarily sustained and that the subsequent events could be more associated with the mixing of the initial leakage gas than with additional contaminant.

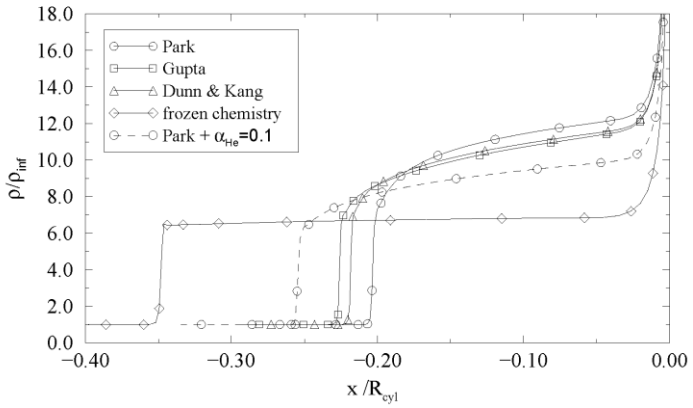


**Figure 31: Normalised computed density distribution along the stagnation streamline of a cylinder flow in HEG condition I; comparison of different sets of chemical reaction rates**

The shock stand off distance and the shock shape resulting from a schlieren image and CFD are compared in Figure 33. The measurement was taken at 3.75 ms after shock reflection, i.e. after the helium contamination took place. Good agreement between computed and measured shock stand-off distance and shock shape could be found for the computation using an air / 10% helium mixture.

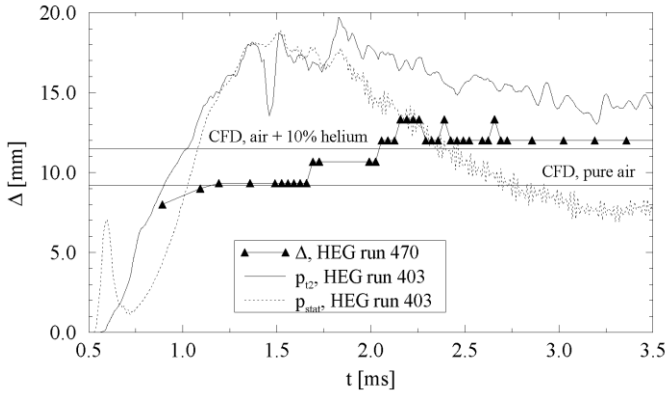


**Figure 32: Temporal development of the shock stand-off distance in comparison with the development of the Pitot pressure and the static pressure; condition I, air**

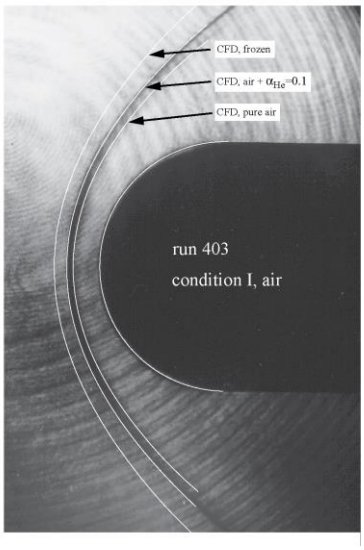


**Figure 33: Comparison of measured and computed shock shapes, HEG operating condition I**

In order to delay the early driver gas contamination, a method which was proposed by Sudani et al. [87] was implemented in HEG. In [87] it was demonstrated that a sleeve, mounted at the end of the shock tube of the T5 Hypervelocity Shock Tunnel of GALCIT is very efficient in delaying the early driver gas contamination. This device was designed in such a way that it captures the driver gas jet along the wall upstream of the shock tube end wall before it mixes with the test gas. For HEG a similar device was designed (see Figure 23) based on computations of the shock reflection process in HEG by Chue and Eitelberg [12]. As shown in Figure 34, a sleeve length of 150 mm was chosen. The gap between the shock tube wall and the sleeve was set to 2 mm. Six 110 mm long and 4 mm thick struts which are evenly distributed along the circumference were used to connect the sleeve with the shock tube wall. Due to the design of the downstream closure of HEG, it is not possible to suck the driver gas into a driver gas removal chamber as was done successfully in T5. The experiments with the sleeve were, therefore, performed by only using the volume between the sleeve and the shock tube plus the additional volume above the shock tube end plate (see Figure 34) to capture the helium.

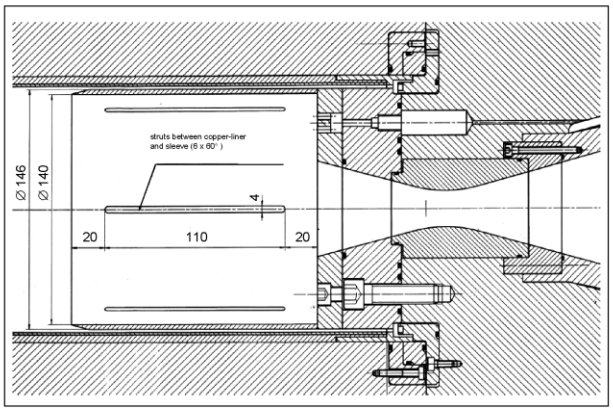


**Figure 34: Sleeve mounted at the end of the HEG shock tube; measures in mm**

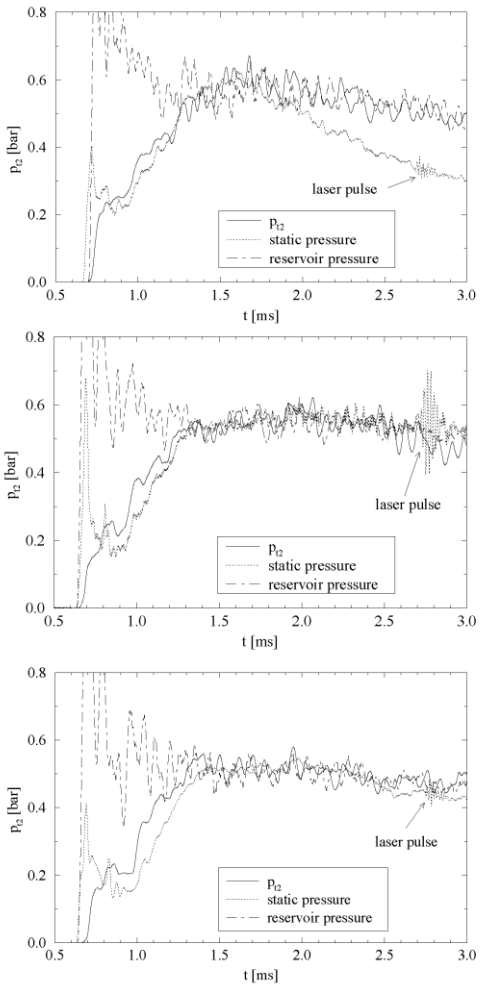


**Figure 35: Temporal development of the reservoir pressure, the static pressure and the Pitot pressure in the test section for condition I; run 513 without sleeve (upper) and run 514 and 515 with sleeve (middle and lower)**

In Figure 35, the temporal development of the reservoir pressure and the Pitot pressure and static pressure in the test section are plotted in the same way as in Figure 28. The oscillations of the static pressure signal at approximately 2.8 ms is caused by electromagnetic interference caused by a laser pulse used for LIF measurements. The results of three subsequent runs are plotted. The upper plot refers to a run without sleeve and the data plotted in the middle and lower diagram were obtained with the sleeve mounted in the shock tube. It is obvious, that the early drop of the static pressure relative to the reservoir and Pitot pressure does not occur during the runs with sleeve. Based on the investigations discussed in the previous sections, it is concluded from these results, that the early driver gas contamination is successfully prevented by the sleeve.

### 5.1.2 Low Enthalpy Operating Condition XIII

As an additional example of the calibration process of HEG operating conditions, the calibration of condition XIII is discussed here. Compared to the conditions considered in section 5.1.1., this condition is termed a low enthalpy condition ($h_0$ = 3.3 MJ/kg). For the calibration measurements the rake shown in Figure 10 was utilised allowing to determine static pressure profiles in addition to Pitot pressure and stagnation point heat transfer profiles. For the nozzle flow computations using the TAU code, different RANS turbulence models were applied along with thermal equilibrium and non-equilibrium computations to determine the influence of different modelling assumptions on the computed free stream conditions. It should be noted that for condition XIII, the chemical relaxation process is in equilibrium and no free stream dissociation exists. The computational grid consisting of about 20,000 grid points and the Mach number contours resulting from the thermal non-equilibrium computation are shown in Figure 36.

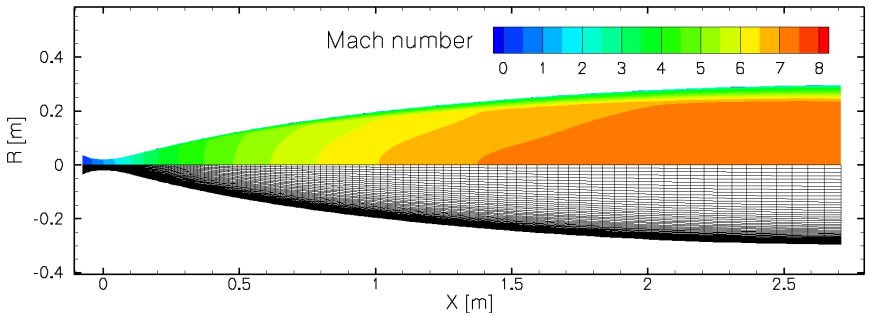


**Figure 36: CFD grid and Mach number contours for the HEG nozzle flow (operating condition XIII)**

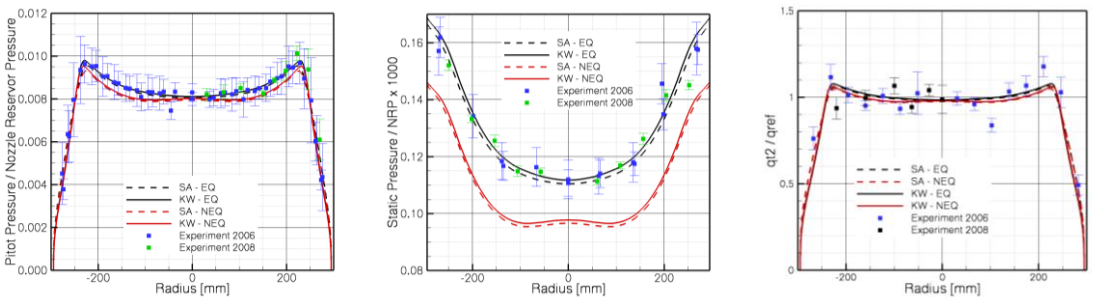


**Figure 37: Comparison of measured and computed normalised Pitot pressure (left), static pressure (middle) and stagnation point heat flux distributions at the nozzle exit plane; NEQ: thermal non-equilibrium, EQ: thermal equilibrium, SA: Spalart-Allmaras turbulence model, KW: Wilcox k-ω turbulence model, NRP: Nozzle reservoir pressure (HEG operating condition XIII)**

A reservoir-pressure inflow boundary condition is used at the subsonic inflow of the nozzle. The thermodynamic conditions at the inflow are computed using isentropic expansion from prescribed nozzle stagnation conditions using the inflow velocity vector which is part of the CFD solution. The nozzle supply conditions for the considered HEG operating conditions are given in Table 1. The chemical non-equilibrium 5 species and 17 reactions rate set for air proposed by Gupta ([26]) was applied. The considered species are molecular and atomic nitrogen and oxygen (N2, O2, N, O) and nitric oxide (NO). The CFD results are subsequently compared with Pitot pressure and stagnation point heat flux measurements on spherical probes and static pressure measurements obtained with the HEG calibration rake. The comparison between numerical and experimental calibration data also included the computation of the flow past the probes used in HEG [42].

In Figure 37, the comparison of measured and computed normalised Pitot pressure, static pressure and stagnation point heat transfer profiles at the nozzle exit plane are shown. The data is normalised using the nozzle reservoir pressure and a heat flux reference value derived from the stagnation point heat flux measurements on the spherical calibration probes. Regarding the Pitot pressure, the computed data resulting from computations assuming a thermal equilibrium or thermal non-equilibrium nozzle expansion lie within the experimental scatter bars. For the present operating condition, the wall boundary layer is assumed to be fully turbulent and the difference due to the application of different turbulence models is negligible. The excellent reproduction of the measured Pitot pressure profile shape confirms the assumption regarding the state of the boundary layer. The best agreement between computed and average measured Pitot pressure profiles is obtained with the thermal equilibrium assumption.

The computed static pressure profiles reveal pronounced deviations resulting from the application of different thermal relaxation models. Excellent agreement of the numerical and experimental results was achieved using the thermal equilibrium assumption. This result highlights the importance of the static pressure measurements since they help to select the most suitable numerical model to determine the free stream pressure and consequently the free stream temperature.

The right plot of Figure 37 shows the comparison of the numerical and experimental normalised stagnation point heat flux profiles. Similar to the Pitot pressure, the computed values of this quantity reveal only slight variations when the assumption of a thermal equilibrium or thermal non-equilibrium nozzle expansion is used. The obtained differences lie within the experimental scatter bars.

## 5.2 High Enthalpy Cylinder Shock Layer Investigations

When considering the re-entry trajectory of a space vehicle returning from low earth orbit into the atmosphere, the most critical point concerning the heating loads on the vehicle is found in the continuum flow region in approximately 70 km altitude. In this region of the re-entry path, the velocity of the vehicle is approximately 6 km/s and the flow past the vehicle is accompanied by strong shock waves, leading to high temperatures ensuing dissociation reactions. The fundamental influence of the thermal and chemical relaxation processes caused by these high temperature effects on the external aerodynamics, i.e. the pressure distribution, flap efficiency, shock/shock and shock/boundary layer interactions and on the heating loads can be investigated by looking at the flow past basic generic flow configurations which are especially designed in order to focus on one of these effects. Additionally, these studies are well suited to validate the ground based facility performance, measurement techniques and computational fluid dynamics (CFD) codes.

A test campaign was performed in HEG to study the relaxation processes in the shock layer of a cylinder placed with its axis transverse to the flow [42]. This configuration was chosen because of the large shock stand-off distance that permits optical measurement techniques to investigate gas properties in the shock layer. The diameter of the cylinder is 90 mm and its length amounts to 380 mm. The cylinder model is equipped with 17 pressure transducers to measure surface pressure distributions and 17 thermocouples to

measure surface heat flux distributions. These transducers were distributed along six rows located in the plane of symmetry at midspan location and 10, 20 and 30 mm to the left and the right of the plane of symmetry. The model was mounted on the nozzle centreline (Figure 38).

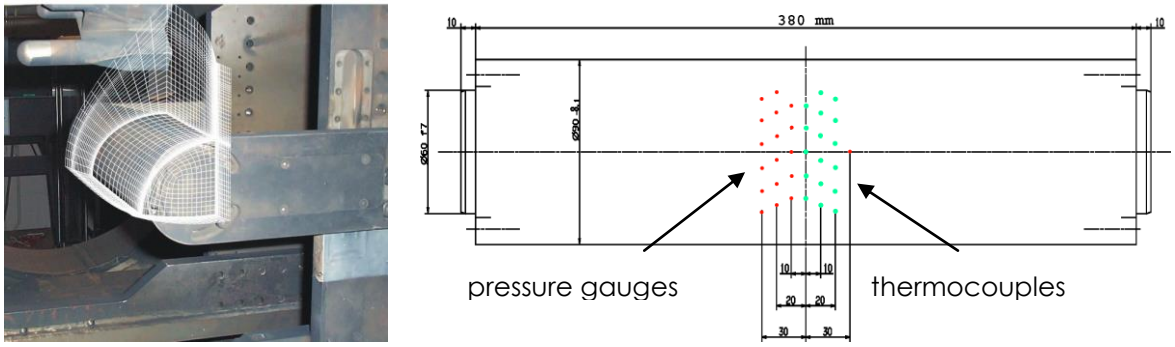


**Figure 38: Cylinder model in the HEG test section including the grid used for the three-dimensional flow field computations (left) and model dimensions and gauge positions (right)**

Surface pressure and surface heat flux measurements and the determination of two dimensional shock layer density distributions by phase step holographic interferometry were performed. The results which will be discussed here were obtained using HEG operating condition III ($h_0$ = 12 MJ/kg, see Table 1). Two and three-dimensional computations of the flow past the cylinder model were performed assuming laminar flow, chemical nonequilibrium, thermal equilibrium and a fully catalytic cylinder wall. The computational grid used for the 3D simulations is shown in the left part of Figure 38. It consists of 33x81x101 grid points. The symmetry plane of the 3D grid was also used for the 2D computations in order to avoid discrepancies caused by different resolutions.

Two dimensional simulations were carried out using the reaction rate models by Park [65], Dunn and Kang [18] and Gupta et al. [26]. The different free stream conditions used for this study result from nozzle computations, each performed with one of the reaction rate models mentioned above. The resulting shock standoff distances were compared with the experimental values and a summary of the results is given in Figure 39.

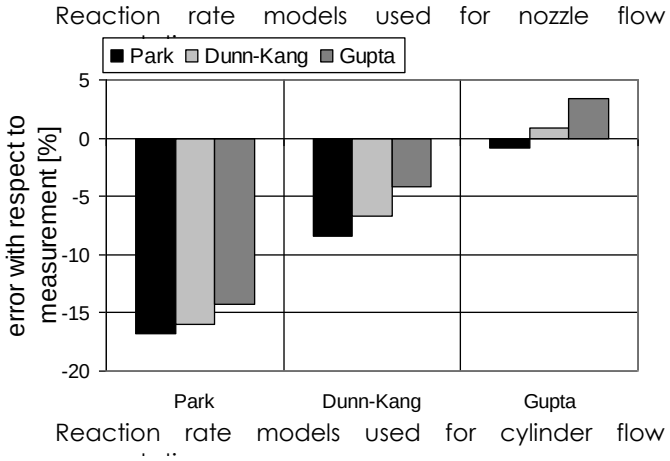


**Figure 39: Comparison of the computed shock stand-off distance resulting from 2D flow field analyses with the values obtained in HEG**

It can be seen that using the reaction rate model of Gupta et al. results in the smallest deviation between computed and measured shock stand-off distance. For that reason this chemistry model was also chosen for further 2D and 3D cylinder flow field computations. In order to investigate the influence of the flow past the edges of the cylinder on the flow in the central part of the model, 3D flow field computations were performed. A comparison between 2D and 3D results for surface pressure and heat flux along the stagnation line in span wise direction is shown in Figure 40. The centre plane of the cylinder is located at z/R=0. Two different sets of inflow conditions were used for the 3D simulations. The first set is referred to as "parallel" and represents a parallel inflow with averaged free stream conditions in the plane of the cylinder position. The second set is referred to as "conical". Here the diverging flow resulting from the conical nozzle computation is used to interpolate inflow conditions on the CFD grid around the cylinder. A comparison of the computed surface pressure and heat flux distributions in the centre plane is given in Figure 41. It is clear from these plots that the surface data in the centre plane resulting from 3D computations compares well with the data obtained from the 2D computation. The heat flux and pressure distributions along the stagnation line of the cylinder obtained with the 3D computations show the influence of the cylinder edge effects on the surface pressure and heat flux. From the centre plane up to about z/R=2.5, no significant impact of the edge effects exists. It can also be seen from Figure 40 that compared to the “parallel” inflow condition, the utilisation of the “conical” condition results in only a small difference of the obtained surface pressure and heat flux in the centre plane.

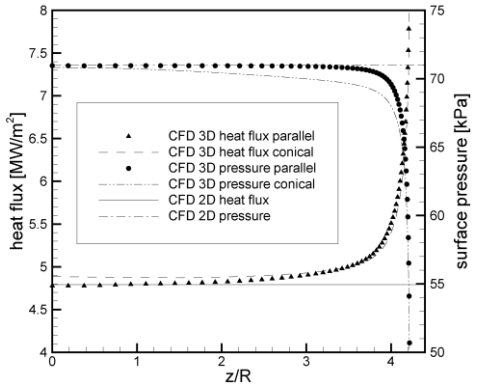


**Figure 40: Comparison of surface pressure and heat flux along the stagnation line in spanwise direction resulting from 2D and 3D computations**

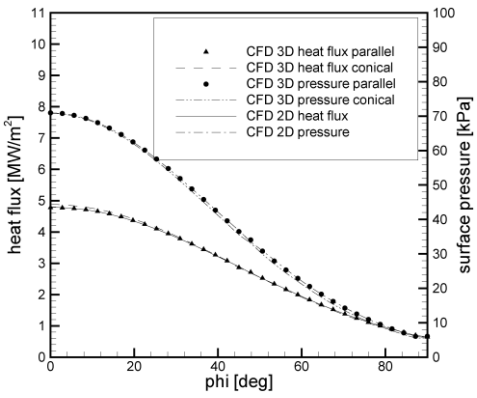


**Figure 41: Comparison of surface pressure and heat flux in the center-plane resulting from 2D and 3D computations**

The comparison between computed and measured surface pressure and surface heat flux measurements for HEG run 627 is shown in Figure 42. Good agreement between the 2D predictions and the measurements was obtained (4% deviation for stagnation pressure and 1% deviation for stagnation heat flux). Based on previous investigations it is obvious that the surface pressure is not very sensitive with respect to the physico-chemical modelling in CFD tools. Therefore the potential of this quantity for code validation can be regarded as low. For the present flow and surface property conditions, this insensitivity was also observed for the surface heat flux. However, shock stand-off distance, density distribution in the shock layer and static free stream pressure are sensitive to variations in the physico-chemical modelling and are therefore well suited for validation purposes.

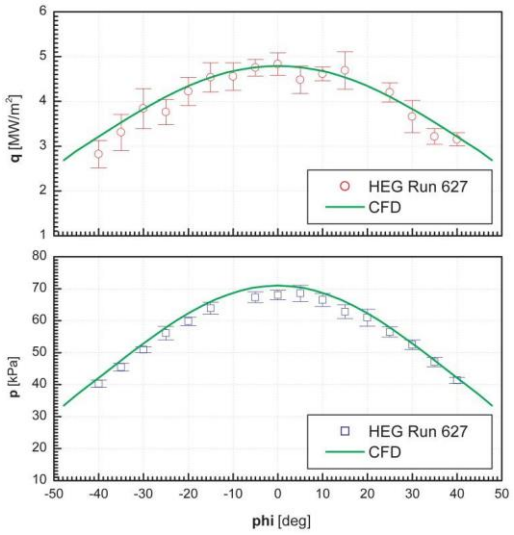


**Figure 42: Comparison of measured and computed surface pressure and heat flux**

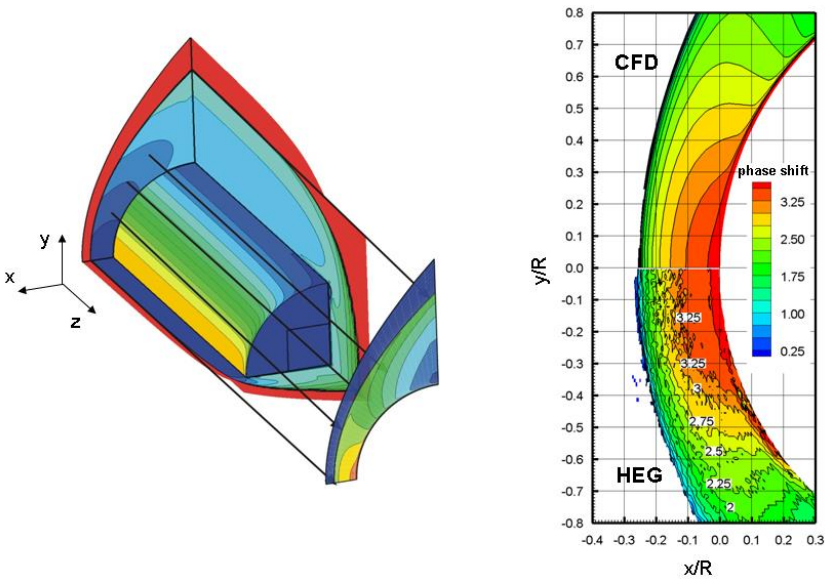


**Figure 43: Sketch of the line of sight phase shift distribution reconstruction based on the computed 3D flow fields (left) and comparison of computed and measured phase shift distribution (right); HEG operating condition III (run 627)**

It was shown through the comparison of the results of the two and three dimensional computations, that the flow in the symmetry plane of the cylinder can be regarded as two dimensional. However 3D effects become important for optical line of sight methods. Therefore, numerical phase shift distributions were obtained from the CFD solutions by using a procedure as described by [31]. A computational ray tracing algorithm was implemented (see Figure 43) and numerical phase shifts were obtained for the 2D computations and the 3D computations with both "parallel" and "conical" free stream conditions. The comparison of the computed and measured phase shift along the stagnation line is given in Figure 44. These Figures show clearly that the result obtained from the 3D computations by ray tracing along a set of lines of sight differ from the 2D CFD results. It should be emphasized that these differences are only due to the contributions of the outer flow regions past the cylinder edges. The use of the "conical" free stream condition for the 3D computation results in a shock stand-off distance which is reduced by about 3%.

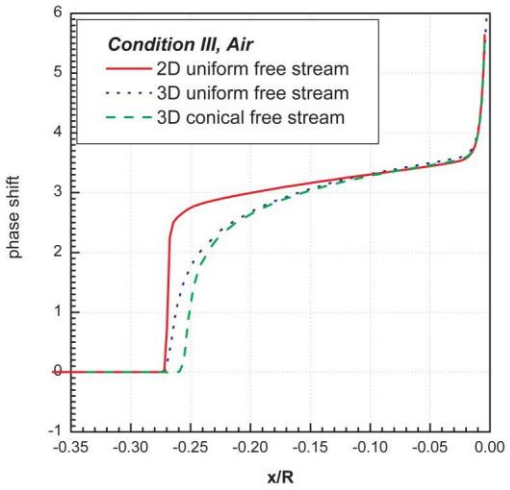


**Figure 44: Comparison of computed phase shift distributions along the stagnation line. The phase shift values are normalized by 2π**

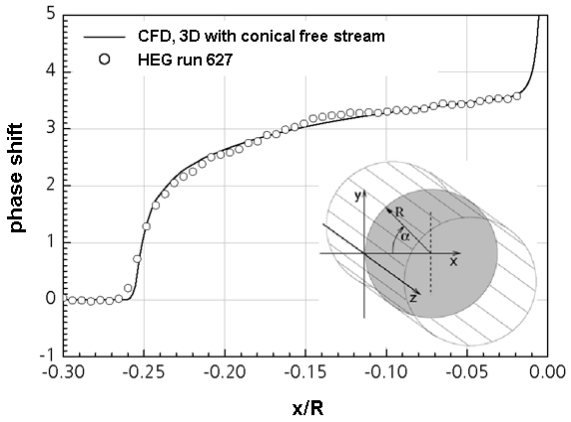


**Figure 45: Comparison of computed and measured phase shift distributions along the stagnation streamline for HEG operating condition III [54]**

Figure 45 shows the computed and measured phase shift distributions along the stagnation streamline. Using the result of the 3D computation with "conical" free stream condition, very good agreement was obtained with the considered experimental phase shift distribution [54]. The corresponding two-dimensional phase shift distributions are plotted in the right part of Figure 43.

## 5.3 Free Jet Testing and CFD Analysis of the HyShot II Scramjet Flight Experiment

In the framework of the European Commission co-funded LAPCAT (Long term Advanced Propulsion Concepts and Technologies) project [86], the methodology of a combined ground based testing and numerical modelling analysis of supersonic combustion flow paths was established. The approach is based on free jet testing of complete supersonic combustion ramjet (scramjet) configurations consisting of intake, combustor and nozzle in the HEG and CFD studies utilising the DLR TAU code [43], [53]).

To demonstrate the capability of this methodology, the HyShot II flight test configuration ([66], [82]) was selected. This generic scramjet consisting of intake, combustor and nozzle was designed such that it contains all necessary components of a scramjet but still generates an overall flow field which is as simple as possible with a well defined combustor inflow. Therefore, it was considered to be a configuration well suited for basic investigations and tool validation purposes.

The HyShot II wind tunnel model installed in the HEG test section is shown in Figure 46. Apart from a wider intake, the geometry of this model is a 1:1 scale representation of the fuelled flow path of the HyShot II scramjet flight test configuration. Compared to the flight configuration, the width of the present intake ramp was extended from 100 mm to 196 mm. The reason for this is to avoid detrimental effects on the flow visualization of the combustor flow by the presence of external shocks close to the outer surface of the glass windows.

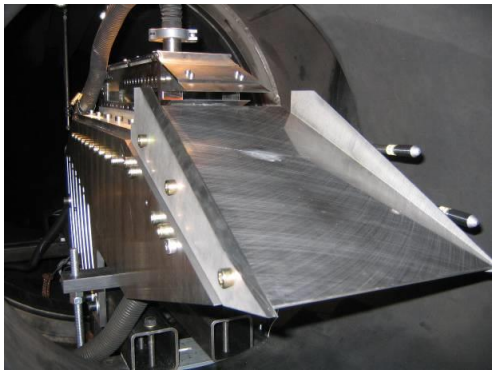

**Figure 46: HyShot wind tunnel model installed in the HEG test section**

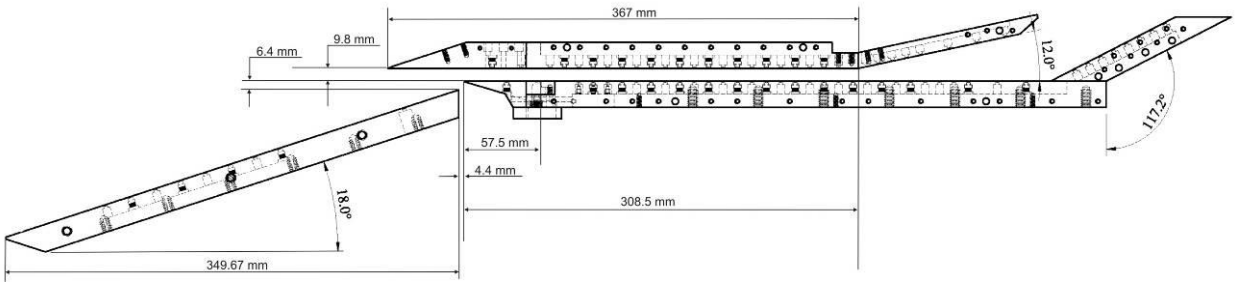


**Figure 47: HyShot II model configuration assembly**

A cut along the symmetry plane of the HyShot II model configuration assembly is shown in Figure 47. The cross sectional shape of the intake and the internal flow path of the wind tunnel model is defined by five parts, the intake ramp, the upper and lower combustion chamber walls and the upper and lower thrust surfaces. The intake is a simple $18^{o}$ wedge. Between the intake and the combustion chamber, a bleed

channel is used such that the boundary layer and entropy layer of the intake ramp do not enter the combustor. Further, the bleed allows the shock generated by the leading edge of the cowl to pass outside the combustion chamber. The combustion chamber is parallel and the cross sectional dimensions are 9.8 x 75 mm. The length of the constant area combustor is 308.5 mm. Fuel is injected into the combustion chamber by a series of four holes, with radius of 1 mm, equally spaced along one line in cross flow direction in the lower combustor wall, 57.5 mm downstream of its leading edge.

Pressures on the model were measured using KULITE pressure transducers. Wall heat transfer was determined from the measured surface temperature histories. MedTherm coaxial thermocouples were utilized. On the intake ramp, 5 pressure gauges and 4 thermocouples were integrated along the symmetry line. The upper combustion chamber wall was instrumented with 23 pressure gauges and 11 thermocouples. The pressure transducers were positioned along the symmetry line and the thermocouples along a line 9 mm off the symmetry line. In the lower combustion chamber wall, 31 pressure transducers and 15 thermocouples were integrated. The pressure gauges were positioned along the symmetry line and the thermocouples downstream of a hydrogen injector along a line 10 mm off the symmetry line. The upper and lower thrust surfaces were instrumented with 5 and 6 pressure transducers, respectively. The origin of the coordinate system used to plot the measured and computed combustion chamber wall pressure and wall heat flux data in the subsequent paragraphs is the leading edge of the lower combustor wall.

The computational domains and the applied boundary conditions used to study the intake and the combustor / nozzle flow fields of the HyShot II configuration are sketched in Figure 48 in a plane cutting through an injector. During the short test time in HEG, no significant heating of the model walls occurs. Therefore, the walls were assumed to be isothermal at a temperature of 300 K and fully catalytic. The HEG free stream (condition XIII, see Table 1) used for the present studies is related to a flight trajectory point of HyShot II in an altitude of 28 km. From the flight data [63], an angle of attack of $\alpha = 3.6^{o}$ was derived and used for the present studies.

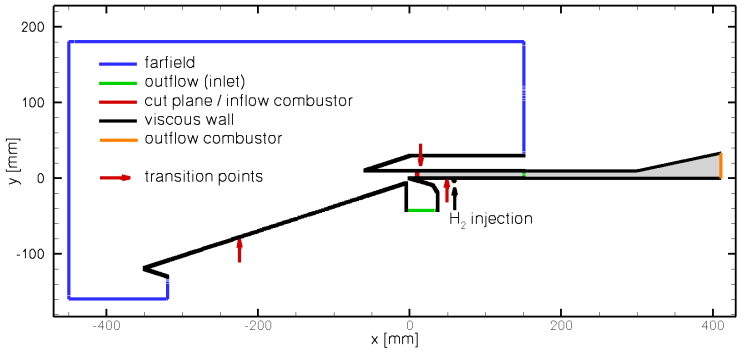


**Figure 48: Computational domains and boundary conditions used for the intake and combustor / nozzle investigations**

In a first step, a three-dimensional (2,500,000 grid points) and a two dimensional computation (440,000 grid points) of the HyShot II fuel off combustor flow were performed. The three-dimensional computational domain covered half of the combustor duct width applying a symmetry boundary condition along the centre line. The inflow conditions were derived from three-dimensional intake computations. The computed and measured normalised surface pressure distributions obtained on the lower combustor wall are compared in Figure 49. The profiles resulting from the computations and from the measurements agree very well. The experimental data shown here represent mean values obtained from multiple runs. In addition to the computed surface pressure data obtained on the centreline, streamwise pressure profiles along lines of 25%, 50% and 75% combustor half width are plotted in Figure 49 revealing only slight

variations in cross flow direction. Consequently, the influence of the combustor side walls on the flow properties in the vicinity of the symmetry plane can be regarded as small.

Based on this result, the three-dimensional computational domain shown in Figure 50 was selected for the fuel on combustor computations. In order to minimize the computational cost all existing flow symmetries were exploited. The combustor inflow conditions result from intake computation. At the outflow plane the major part of the flow is supersonic and consequently the conservative variables are extrapolated. Symmetry boundary conditions are used at the span wise boundary planes. One is located at z = 0 mm cutting through the centre of a porthole injector. The second symmetry plane is located at z = 9.375 mm representing half the distance between two injectors. Therefore, only one eighth of the original span width of the HyShot II configuration needs to be modelled. At the bottom and top wall, viscous no-slip boundary conditions are applied. Transition from laminar to turbulent boundary layer flow at the top and bottom combustor wall is modelled using the criterion $\left[Re_\theta / M_e\right]_{crit} = 200$. Here, $Re_\theta = \rho_e u_e \theta / \mu_e$ denotes the

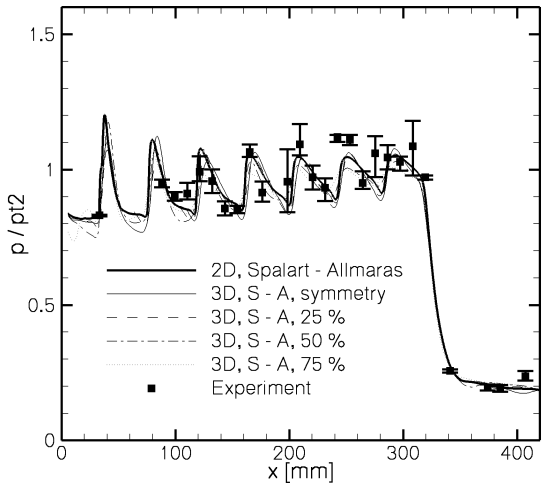


**Figure 49: Normalised computed and measured surface pressure distributions on the lower HyShot II combustor wall; fuel off condition**

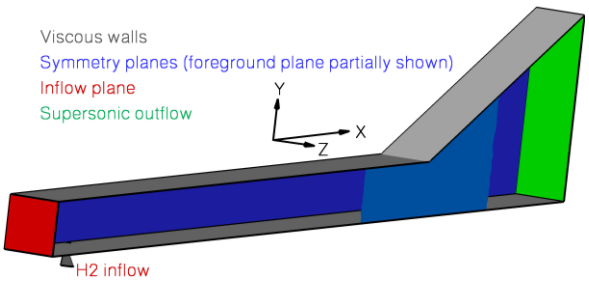


**Figure 50: Computational domain and boundary conditions used for the three-dimensional combustor fuel on computations (x,y,z scaled with 1:2:2)**

Reynolds number based on the boundary layer momentum thickness and $M_e$ the Mach number at the boundary layer edge. The sonic hydrogen injection was modelled by partially including the injector in the computational domain. A reservoir inflow condition as used for the HEG nozzle computations was applied at the hydrogen inflow boundary. A total hydrogen pressure of 4.6 bar and a total temperature of 300 K were prescribed resulting in a fuel equivalence ratio of $\phi = 0.295$. The fuel equivalence ratio $\phi$ is defined as the ratio of the fuel-to-oxidizer ratio to the stoichiometric fuel-to-oxidizer ratio: $\phi = 8 \cdot \dot{m}_{H_2} / \dot{m}_{O_2}$.

The computational grid consists of about 850,000 grid points. Structured prismatic sub layers were used at the viscous walls. A dimensionless wall spacing of y+ = O(1) was used to ensure sufficient resolution for the low Reynolds number turbulence models and for the computation of the wall heat flux. The normalised wall pressure and heat flux distributions generated by hydrogen combustion in the HyShot II combustor on the lower wall are plotted in Figure 51. The fuel equivalence ratio was chosen such that a steady state combustor flow was obtained. According to the design of the HyShot II flight experiment, the combustor is expected to show a steady state supersonic combustion flow up to an equivalence ratio of $\phi \approx 0.3$ [66]. For clarity, the experimental data are subdivided into three groups with different ranges of fuel equivalence ratio, $0.266 < \phi < 0.288$, $0.315 < \phi < 0.329$ and $0.341 < \phi < 0.351$. The computed normalised pressure and heat flux distributions were obtained with the DLR TAU code using the Spalart-Allmaras and the Wilcox k-ω turbulence model. For all equivalence ratios, the measured wall pressure distributions are characterized by a continuous increase along the combustor indicating supersonic combustion. Good agreement between the measured and the computed pressure distributions is achieved. Further, the computed normalised pressure distributions depend only weakly on the applied turbulence model.

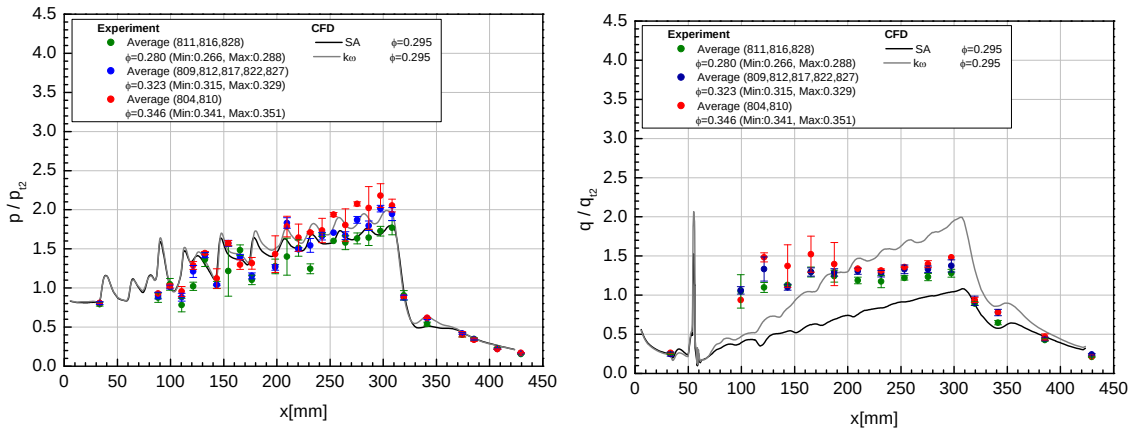


**Figure 51: Normalised computed and measured surface pressure (left) and wall heat flux (right) distributions on the lower HyShot II combustor wall; fuel on conditions; the numbers in parenthesis denote the HEG run numbers**

Regarding the comparison of measured and computed wall heat flux distributions, significant differences occur between experimental and numerical results. While the computed heat flux increases continuously downstream of the fuel injection location, the measured values remain approximately constant after an initial stepwise increase. A possible reason for this discrepancy between measured and computed heat flux values could be the strong span wise heat flux gradients obtained downstream of the hydrogen injectors. The heat flux gauges are positioned downstream of a fuel injector and even a small flow misalignment could cause the observed discrepancy.

In general, the comparison of measured and computed pressure and heat flux distributions shows that the pressure generated by supersonic combustion can be predicted numerically with satisfactory accuracy. However, apart from the qualitative difference between the measured and computed heat flux distributions on the lower combustor wall, the CFD data depends strongly on the applied turbulence model. The computed peak values on the lower combustor wall differ by a factor of almost two. This result points out that further research is required regarding the modelling of turbulence in scramjet combustors in order to reduce the uncertainties of numerical wall heat flux predictions. This should include the utilisation of RANS, DES and LES models to compute the fuel/air mixing as well as combustion including detailed chemistry. Corresponding activities are planned in the framework of the currently running LAPCAT II project and the experiments performed as part of LAPCAT I will serve as validation data base.

## 5.4 Ground Based Testing of the DLR SHEFEX-I Flight Experiment

The SHarp Edge Flight EXperiment (SHEFEX) program of the German Aerospace Center (DLR) is primarily focused on the investigation of the potential to utilise improved shapes for space vehicles by considering sharp edges and facetted surfaces. The goal is to set up a future sky based test facility to gain knowledge of the physics of hypersonic flow, complemented by numerical analysis and ground based testing. Further, the series of SHEFEX flight experiments offers an excellent test bed for new technological concepts and in-flight experimental sensors and it is a source of motivation for young scientist and engineers providing an excellent school for future space-program managers. After the successful first SHEFEX flight in October 2005, a second is scheduled later this year and additional flights are planned for 2015 ff. A detailed discussion of the present results and future challenges of the DLR SHEFEX program is given by Longo [52].

**Figure 52: SHEFEX-I flight hardware**

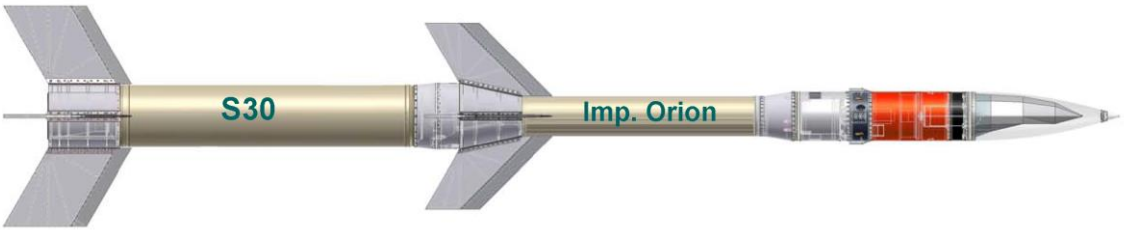


**Figure 53: SHEFEX-I launch vehicle**

In the context to identify and evaluate new technologies to advance hypersonic space transportation, a major goal of the SHEFEX-I flight experiment was to exploit the enhancement of aerodynamic vehicle performance by using sharp edge configurations. Simultaneously, the utilisation of facetted thermal protection systems (TPS) can significantly reduce the manufacturing and maintenance cost compared to a conventional TPS system consisting of thousands of individually shaped tiles [51]. Driven by the facetted concept, two main criteria were used to define the aerodynamic shape of the SHEFEX-I fore body. To have as many as possible facetted panels and to represent as many as possible configuration details of space vehicles, such as concave and convex chamfers, wedged compression corners to simulate control surfaces and sharp unswept leading edges. As a consequence, the SHEFEX-I configuration became non-symmetric as is shown in Figure 52.

The launcher was a two-stage solid propellant sounding rocket system conceived primarily for ballistic microgravity experiments. The launch vehicle consisted of a Brazilian S30 motor as first stage and an Improved Orion motor as second stage (Figure 53). Between the facetted SHEFEX-I experiment and the second stage, two cylindrical modules were positioned which housed the recovery system, the main electronics, the data acquisition devices, the power supply and the cold gas attitude control system. Since

the facetted body has no aerodynamic control devices, the second stage remained attached to the fore body until the end of the experiment to provide flight stability through its fins. The asymmetry of the payload imposed severe trim conditions for the re-entry, requiring new launcher fins, stage-adapters and ballast [52].

The SHEFEX-I flight was launched from the Norwegian Andoya rocket range in October 2005. The mission profile of the SHEFEX-I flight and a picture taken from the onboard camera are given in Figure 54. After separation from the first stage, the second stage was ignited in approximately 20 km flight altitude. The burn-out of the second stage was followed by the separation of the nose cone at an altitude of 100 km. The nose cone protected the payload during the launch phase of the experiment. Due to the asymmetric shape of SHEFEX-I this was also needed in order to stabilise the complete configuration during launch. After the apogee in approximately 211 km altitude was reached, the vehicle started its decent towards the earth. Experimental data was gathered between 60 km and 20 km altitude. The total flight time was 500 seconds, including 45 seconds of test time [90]. The reconstruction of the flight included the post processing of the radar data and based on this the determination of the atmospheric conditions during the flight. The reconstruction of the angle of attack $\alpha$ and angle of yaw $\beta$ of the spinning vehicle was performed with the help of onboard sensors. This assessment of the free stream vector was performed by using the flight mechanic data obtained with the Digital Miniature Attitude Reference System (DMARS) platform. The vehicle started re-entering the atmosphere with an oscillation in pitch and yaw which damped out over time [55]. The vehicle finally achieved a stable flight attitude with a decreasing precession around the flight vector. Details about the flight analysis are given in [4] and [5]. In order to gain additional confidence in the flight reconstruction and analysis, the cross-check with data obtained during the ground based testing post flight analysis and accompanying CFD investigations is of large interest. With the SHEFEX-I flight and the subsequent numerical and experimental post flight analysis, DLR could for the first time close the loop between the three major disciplines of aerothermodynamic research – CFD, ground based testing and flight – using own data.

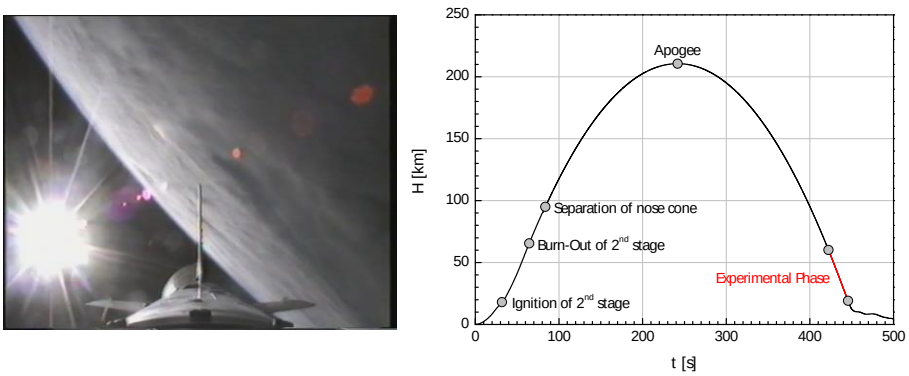


**Figure 54: Image taken from the onboard camera during the SHEFEX-I flight (left) and mission profile (right)**

The flight reconstruction in HEG was performed for an altitude of 20.3 km. This trajectory point was reached close to the end of the experimental phase where the oscillatory motion of the vehicle became small. HEG operating condition XXI (see Table 1) was used to match the flight Mach and Reynolds number as closely as possible. From Figure 55 it can be seen that the Reynolds number based on the vehicle length agrees to 2.5% and the Mach number to 6% with the selected flight point data.

The HEG stainless steel wind tunnel model of the SHEFEX-I configuration has a total length of 280 mm (see right part of Figure 56). The scaling factor to the flight configuration is 1:2.964. It is instrumented with a total number of 152 thermocouples and pressure transducers. The model was installed in the HEG

test section on a support system which allows to vary the angle of attack (± 12°) and angle of yaw (±5°) (Figure 56).

For each run in HEG, a numerical analysis was performed applying the DLR TAU code. In order to judge the state of the boundary layer, computations were performed assuming a laminar and a fully turbulent wall boundary layer. The Spallart Allmares (SAE), Wilcox k-ω (WIL), the linear explicit algebraic stress model by Rung (LEA) [74] and the shear stress transport model by Menter (MEN) were applied. The abbreviations in parenthesis denote the labels used in the figure legends below.

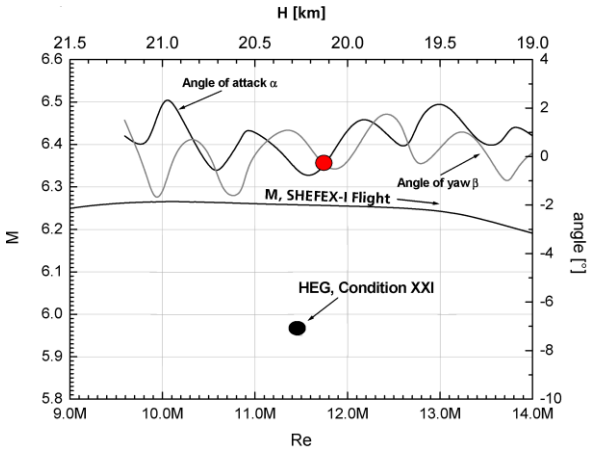


**Figure 55: Flight Mach number and Reynolds number compared to the corresponding values of HEG operating condition XXI; the angle of attack, yaw angle and altitude of the selected flight trajectory point are also given**

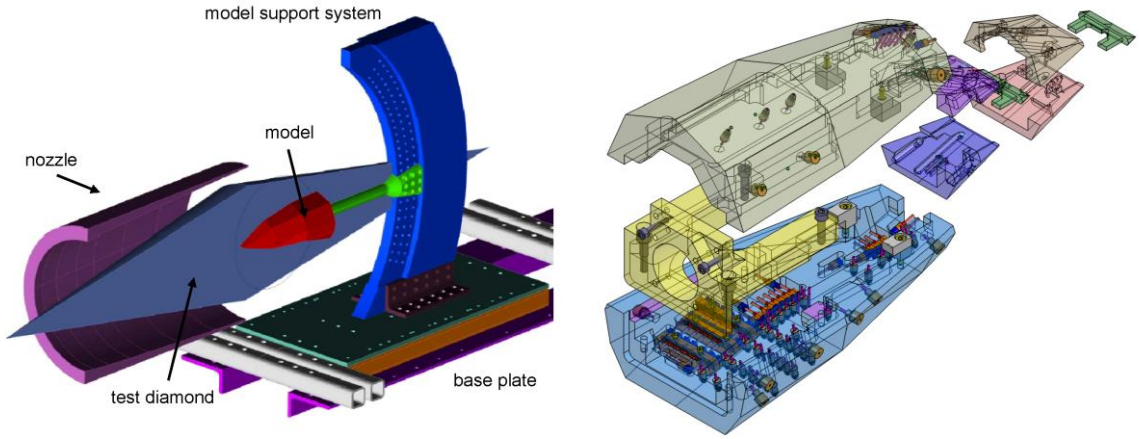


**Figure 56: Sketch of the SHEFEX-I model integration in the HEG test section (left) and model design drawings (right)**

The comparison of measured and computed normalised surface pressure (left) and wall heat flux (right) distributions along the lower SHEFEX-I symmetry line (SYMMB) are plotted Figure 57. The pressure data is normalised by the HEG reservoir pressure $p_0$ and the surface heat flux data is normalised with a reference value measured in the stagnation point of a spherical probe installed in the HEG test section. The diameter of this sphere is 20 mm.

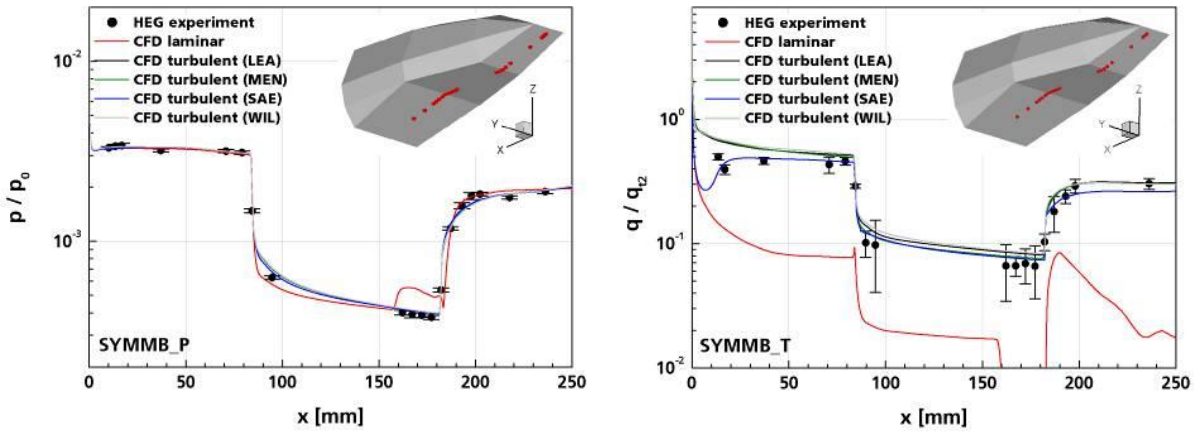


**Figure 57: Comparison of measured and computed normalised surface pressure (left) and wall heat flux (right) distributions along the lower SHEFEX-I symmetry line**

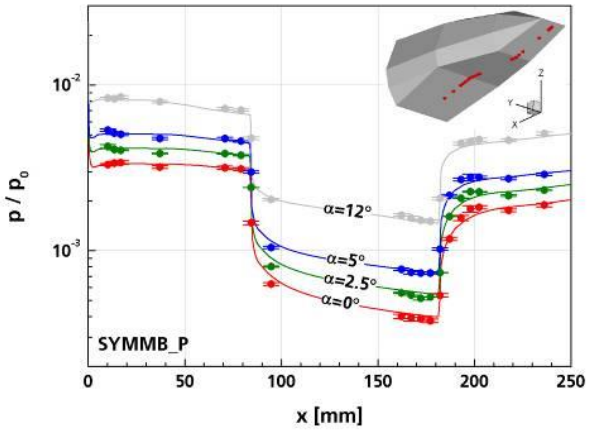


**Figure 58: Comparison of measured and computed normalised surface pressure distributions along the lower SHEFEX-I symmetry line for varying angle of attack**

The error bars given in the plots incorporate the measurement error as well as the fluctuation of the signal during the test time. The measured and computed normalised surface pressure distributions assuming a fully turbulent flow agree well. The major difference between the surface pressure distributions resulting from the laminar and turbulent flow field computations is a separated flow region at the ramp hinge line (x=182 mm) occurring in the laminar flow solution. This can not be identified in the measured data indicating that the boundary layer on the SHEFEX-I wind tunnel model is turbulent. While the difference between the pressure distributions obtained with different turbulence models is small, the predicted heat flux distributions resulting from the Spallart Allmares and the Wilcox k-ω, Rung and Menter SST model show distinct differences (Figure 57). In general, the best agreement with the measured data was obtained with the Spallart Allmares turbulence model. The heat flux predicted by assuming laminar boundary layer flow is significantly lower and the distribution also differs qualitatively due to the flow separation at the ramp hinge line. In Figure 58, the measured and compute normalised wall pressure distributions along the lower symmetry line are compared for varying angle of attack. Again good agreement was obtained between the measured and computed data and even at the highest angle of attack no flow separation at the ramp hinge line was detected.

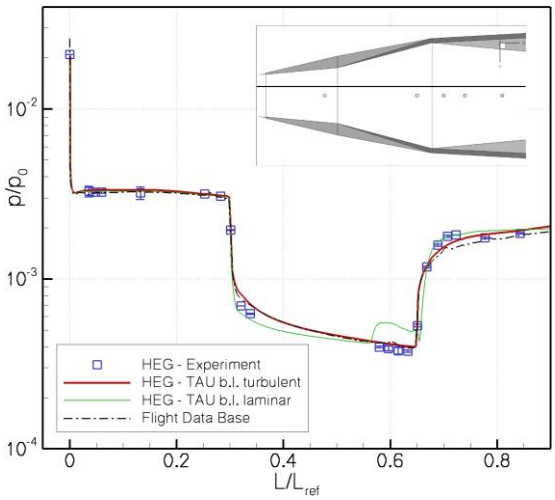


**Figure 59: Comparison of the HEG post flight analysis normalised surface pressure data with the SHEFEX-I flight data base ($\alpha$=0°)**

From Figure 59 it can be seen that very good agreement between the normalised surface pressure distribution along the lower symmetry line resulting from the HEG post flight analysis and the SHEFEX-I flight data base was obtained.

## 6.0 ACKNOWLEDGEMENT

The work presented in chapter 5.3 was performed within the "Long-Term Advanced Propulsion Concepts and Technologies" project investigating high-speed airbreathing propulsion. LAPCAT, coordinated by ESA-ESTEC, was supported by the EU within the 6th Framework Programme Priority 1.4, Aeronautic and Space, Contract no.: AST4-CT-2005-012282. Further info on LAPCAT can be found on http://www.esa.int/techresources/lapcat.

## 7.0 REFERENCES

[1] Anderson, J. D., Hypersonic and High Temperature Gas Dynamics. McGraw Hill, 1989

[2] Anderson, W.K., Bonhaus D.L.: An Implicit Upwind Algorithm for Computing Turbulent Flows on Unstructured Grids. Computers Fluids Vol. 23, No. 1, pp 1-21, 1994

[3] Barth, T. J., Jespersen, D. C., The Design and Application of Upwind Schemes on Unstructured Meshes. AIAA-89-0366, AIAA 27th AIAA Aerospace Sciences Meeting, Reno, 1989

[4] Barth, T., Eggers, Th., SHEFEX - A First Aerodynamic Post-Flight Analysis, New Results in Numerical and Experimental Fluid Mechanics VI, Springer Verlag, 2006

[5] Barth, T., Aero- and Thermodynamic Analysis to SHEFEX I, Engineering Applications of Computational Fluid Mechanics, Vol. 1, 2007

[6] Bottin, B., Aerothermodynamic Model of an Inductively-Coupled Plasma Wind Tunnel. PhD-Thesis University of Liege, 1999

[7] Brenner, G., Numerische Simulation von Wechselwirkungen zwischen Stößen und Grenzschichten in chemisch reagierenden Hyperschallströmungen, DLR Forschungsbericht 94-04, 1994

[8] Brenner, G., Prinz, U., Numerical Simulation of Chemical and Thermal Nonequilibrium Flows after Compression shocks, AIAA 92-2879, 1992

[9] Brenner, G., Gerhold, T., Hannemann, K., Rues, D., Numerical Simulation of Shock/Shock and Shock-Wave/Boundary Layer Interactions in Hypersonic Flows, Computers Fluids Vol. 22, No.4/5, p.427, 1993

[10] Brück, S., Investigation of Shock-Shock Interactions in Hypersonic Reentry Flows, In: Sturtevant, B., Sheperd, J.E., Hornung, H.G. (Eds.), Proceedings of the 20th International Symposium on Shock Waves, Pasadena, CA, USA, July 1995, pp.215-220, World Scientific, 1996

[11] Brück, S., Radespiel, R., Longo, J. M. A., Comparison of Nonequilibrium Flows past a Simplified Space-Shuttle Configuration, AIAA 97-0275, 35th Aerospace Sciences Meeting & Exhibit, Reno, NV, January 6-10, 1997

[12] Chue, R.S.M., Eitelberg, G., Studies of the transient flows in high enthalpy shock tunnels, Experiments in Fluids 25, pp. 474 – 486, 1998

[13] Cook, W.J., Felderman, E.J., Reduction of Data from Thin-Film Heat Transfer Gauges: A Concise Numerical Technique, AIAA Journal, 4(3); pp 561-562, 1966

[14] Eaton, W.P., Smith, J.H., Micromachined pressure sensors: review and recent development, Smart Mater. Struct., 6, 530-539, 1997

[15] Eaves, R.H., Kidd, C.T., Miniature Co-axial Surface Thermocouples for Heat Transfer Rate Measurements in Hypersonic Wind Tunnels, 41st Supersonic Tunnel Association Meeting, LA, USA, 1974

[16] Eucken, A., Über das Wärmeleitvermögen, die spezifische Wärme und die innere Reibung der Gase. Physik. Zeitschrift 14(8), pp. 324-332, 1913

[17] Ewald, B.F.R., Review Article Multi-component force balances for conventional and cryogenic wind tunnels, Meas. Sci. Technol., 11, R81–R94, 2000

[18] Dunn, M.G., Kang, S.W., Theoretical and experimental studies of reentry plasmas, NASA CR-2232, 1973

[19] Gaffney, R.L., White, J.A., Girimaji, S.S., Drummond, J.P., Modeling Turbulent Chemistry Interactions using Assumed PDF Methods. 28th AIAA/SAE/ASME/ASEE Joint Propulsion Conference and Exhibit, 1992

[20] Galle, M., Ein Verfahren zur numerischen Simulation kompressibler reibungsbehafteter Strömungen auf hybriden Netzen. DLR/FB-99/04 German Aerospace Center, DLR, 1999

[21] Gerhold, T., Friedrich, O., Evans, J., Galle, M., Calculation of Complex Three-Dimensional Configurations Employing the DLR-TAU-Code. AIAA-Paper 97-0167, 1997

[22] Gerlinger, P., Investigation of an Assumed PDF Approach for Finite Rate Chemistry. Combustion Science and Technology, Vol. 175: 841-872, 2003

[23] Gerlinger, P., Numerische Verbrennungssimulation., Springer 2005

[24] Gerlinger, P., An Implicit Multigrid Method for Turbulent Combustion. Journal of Computational Physics, Vol. 167: 247-276, 2001

[25] Gosse, R., Candler, G., Diffusion Flux Modeling: Application to Direct Entry Problems, AIAA-Paper 2005-389, 2005

[26] Gupta, R.N., Yos, J.M., Thompson, R.A., Lee, K.P., A Review of Reaction Rates and Thermodynamic and Transport Properties for an 11-Species Air Model for Chemical and Thermal Nonequilibrium Calculations to 30000 K. NASA Reference Publication, No. 1232, 1990

[27] Gurvich, I. V., Thermodynamic Properties of Individual Substances, Hemisphere Publishing, 1989

[28] Hannemann, K, Krek, R., Eitelberg, G., Latest Calibration Results of the HEG Contoured Nozzle, In: Sturtevant, B., Sheperd, J.E., Hornung, H.G. (Eds.), Proceedings of the 20th International Symposium on Shock Waves, Pasadena, CA, USA, July 1995, pp. 1575-1580, World Scientific, 1996

[29] Hannemann, K., Computation of High Enthalpy Flow Past the Electre Standard Model in HEG Conditions (TC2.b), ESA Manned Space Transportation Programme, Proc. Aerothermodynamics Workshop, ESTEC, Noordwijk, NL, 25 - 27 March, 1996

[30] Hannemann, K., Schnieder, M., Reimann, B., Martinez Schramm, J., The influence and delay of driver gas contamination in HEG, AIAA 2000-2593, 21st AIAA Aerodynamic Measurement Technology and Ground Testing Conference, Denver, CO, 19-22 June, 2000

[31] Hannemann, K., Martinez Schramm, J., Karl, S., Beck, W.H., Cylinder Shock Layer Density Profiles Measured in High Enthalpy Flows in HEG, AIAA 2002-2913, 22nd AIAA Aerodynamic Measurement Technology and Ground Testing Conference, St. Louis, MO, June 24-28, 2002

[32] Hannemann, K., High Enthalpy Flows in the HEG Shock Tunnel: Experiment and Numerical Rebuilding, AIAA 2003-0978, 41st AIAA Aerospace Sciences Meeting and Exhibit, 6-9 Jan, Reno, Nevada, 2003

[33] Hänel, D., Schwane, R., An Implicit Flux-Vector Splitting Scheme for the Computation of Viscous Hypersonic Flows. AIAA-89-0274, AIAA 27th AIAA Aerospace Sciences Meeting, Reno, 1989

[34] Haselbacher, A.; Blazek, J., On the Accurate and Efficient Discretisation of the Navier-Stokes Equations on Mixed Grids. AIAA Journal Vol. 38(11), 2000

[35] Herning, F., Zipperer, L., Beitrag zur Berechnung der Zähigkeit technischer Gasgemische aus den Zähigkeitswerten der Einzelbestandteile, Gas- und Wasserfach 79, 1936

[36] Hirschfelder, J.O., Generalization of the Eucken Approximation fort he Heat Conductivity of Polyatoomic or Chemically Reacting Gas Mixtures. Conference on Thermodynamics and Transport Properties of Fluids, 1957

[37] Hornung, H.G., Non-equilibrium dissociating nitrogen flow over spheres and circular cylinders.J. Fluid Mech. vol 53, part 1, pp. 149-176, 1972

[38] Hornung, H.G., Experimental Hypervelocity Flow Simulation, Needs, Achievements and Limitations, First Pacific International Conference on Aerospace Science and Technology, PICAST'1, Tainan, Taiwan, 1993

[39] Jameson, A., Time dependent calculations using multigrid, with application to unsteady flows past airfoils and wings. AIAA paper 91-1596, 1991

[40] Jameson, A., Schmidt, W., Turkel, E., Numerical Solution of the Euler Equations by Finite Volume Methods Using Runge-Kutta Time-Stepping Schemes. AIAA 81-1259, AIAA 14th Fluid and Plasma Dynamic Conference, Palo Alto, 1981

[41] Jessen, C., Grönig, H., A Six-Component Balance for Short Duration Hypersonic Facilities, in: New Trends in Instrumentation for Hypersonic Research, pp 295-305, Boutier A (Ed.), Kluwer Academic Publishers, The Netherlands, 1993

[42] Karl, S., Martinez Schramm, J., Hannemann, K., High enthalpy shock tunnel flow past a cylinder : A basis for CFD validation New Results in Numerical and Experimental Fluid Mechanics IV, Vol. 87, Springer, 2004

[43] Karl, S., Hannemann, K., Mack, A., Steelant. J., CFD Analysis of the HyShot II Scramjet Experiments in the HEG Shock Tunnel, AIAA 2008-2548, 15th AIAA International Space Planes and Hypersonic Systems and Technologies Conference, 28 April – 1 May 2008, Dayton, Ohio, USA

[44] Kendall, D.N., Dixon, W.P., Schulte, E.H., Semi-conductor Surface Thermocouples for Determining Heat Transfer Rates, IEEE Transactions on Aerospace and Electronic Systems, AES-3, No 4., 1967

[45] Kroll, N., Radespiel, R., An Improved Flux Split Discretization Scheme for Viscous Flows, DLR Forschungsbericht 93-53, 1994

[46] Kroll, N., Radespiel, R., Rossow, C.-C., Accurate and Efficient Flow Solvers for 3D Applications on Structured Meshes, in "Computational Fluid Dynamics", VKI-LS 1994-05, Von Karman Institute for Fluid Dynamics, Rhode-Saint-Genèse, Belgium, 1994

[47] Landau, L.D., Teller, E., Zur Theorie der Schalldispersion (Theory of Sound Dispersion). Phys. Z. Sowjetunion, Vol. 10(34), 1936

[48] Lieneweg, F., Handbuch Technische Temperaturmessung, Friedr. Vieweg und Sohn Verlagsgesellschaft mbH Braunschweig, 1976

[49] Lu, F.K., Marren, D.E. (Eds.), Advanced Hypersonic Test Facilities, Progress in Astronautics and Aeronautics, Volume 198, 2002

[50] Lukasiewicz, J., Experimental Methods of Hypersonics, Marcel Dekker, Inc., New York, 1973

[51] Longo, J.M.A., Eggers, Th., Gülhan, A., Turner, J., Weihs, H., Designing Flight Experiments for Hypersonic Flow Physics, Proceedings of RTO / AVT / VKI Lecture Series "Flight Experiments for Hypersonic Vehicle Development", Brussels, Belgium, 2005

[52] Longo, J., Present Results and Future Challenges of the DLR SHEFEX Program, AIAA 2009-7226, 16th AIAA International Space Planes and Hypersonic Systems and Technologies Conference, Bremen, Germany, 19 – 22 October 2009

[53] Martinez Schramm, J., Karl, S., Hannemann, K., Steelant. J., Ground Testing of the HyShot II Scramjet Configuration in HEG, AIAA 2008-2547, 15th AIAA International Space Planes and Hypersonic Systems and Technologies Conference, Dayton, Ohio, USA, 28 April – 1 May 2008

[54] Martinez Schramm, J., Aerothermodynamische Untersuchung einer Wiedereintrittskonfiguration und ihrer Komponenten in einem impulsbetriebenen Hochenthalpie-Stoßkanal, Dissertation Universität Göttingen, 2008

[55] Martinez Schramm, J., Wagner, A., Wolfram, J., Hannemann, K., Barth, T., Mulot, J.-D., Post Flight Analysis of SHEFEX I: Shock Tunnel Testing and Related CFD Analysis, AIAA 2009-7216, 16th AIAA International Space Planes and Hypersonic Systems and Technologies Conference, Bremen, Germany, 19 – 22 October 2009

[56] Medtherm Corporation, Coaxial Thermocouple Probes, Bulletin 500, 10-00, Post Office Box 412, Huntsville, Alabama 35804, USA, 2000

[57] Mee, D.J., Daniel, W.J.T., Simmons, J.M., Three-Component Force Balance for Flows of Millisecond Duration, AIAA Journal, Vol. 34, No. 3, pp 590-595, 1996

[58] Menter, F., Two-Equation Eddy-Viscosity Turbulence Models for Engineering Applications. AIAA-Jounal, Vol. 32, No. 8, 1994

[59] Merzkirch, W., Flow Visualization, Academic Press, 1974

[60] Miller, C.G., Comparison of Thin-film Resistance Heat-Transfer Gages with Thin-Skin Calorimeter Gages in Conventional Hypersonic Wind Tunnels, NASA TM 83197, 1981

[61] Millikan, R.C., White, D.R., Systematics of Vibrational Relaxation. Journal of Chemical Physics, Vol. 39(12):3209-3213, 1963

[62] Oertel, H., Wärmeübergangsmessungen, Kurzzeitphysik, Springer Verlag, 1967

[63] Owen, R. Cain, T., Reconstruction of the Hyshot-2 Flight from onboard sensors, Proceedings of the Fifth European Symposium on Aerothermodynamics for Space Vehicles, Cologne, Germany, 8-11 November 2004

[64] Palmer, G.E., Wright, M.J., Comparison of Methods to Compute High-Temperature Gas Viscosity. Journal of Thermophysics and Heat Transfer, Vol. 17, 2003

[65] Park, C., On convergence of computation of chemically reacting flows, AIAA-85-0247, AIAA 23rd Aerospace Sciences Meeting, Reno, NV, 1985

[66] Paull, A., Alesi, H., Anderson, S., The HyShot flight program and how it was developed, AIAA 2002-5248, AIAA/AAAF 11th International Space Planes and Hypersonic Systems and Technologies Conference, Orleans, France, 2002

[67] Quirk, J.J., A Contribution to the Great Riemann Solver Debate. Int. Journal in Numerical Methods in Fluids, Vol. 18:555–574, 1994

[68] Radespiel, R., Longo, J. M. A., Brück, S., Schwamborn, D., Efficient Numerical Simulation of Complex 3D Flows with Large Contrast, in: 77th AGARD Fluid Dynamics Panel Meeting and Symposium on Progress and Changes in CFD Methods and Algorithms, AGARD-CP-578, pp.33-1 - 33-11, Sevilla, October 1995

[69] Ramshaw, J.D., Self Consistent Effective Binary Diffusion in Multicomponent Gas Mixtures, Journal of Non-Equilibrium Thermodynamics, Vol. 15, 1990

[70] Ramshaw, J.D., Chang, C.H., Computational Fluid Dynamics Modeling of Multicomponent Thermal Plasmas, Plasma Chemistry and Plasma Processing, Vol. 12, No.3, 1992

[71] Reimann, B., Johnston, I., Hannemann, V., The DLR TAU-Code for High Enthalpy Flows, Notes on Numerical Fluid Mechanics and Multidisciplinary Design, Vol.87, Springer, 2004

[72] Robinson, M., Simultaneous Lift, Moment and Thrust Measurements on a Scramjet in Hypervelocity Flow, PhD Thesis, The University of Queensland, Australia, 2003

[73] Robinson, M., Hannemann, K., Short Duration Force Measurements in Impulse Facilities, AIAA 2006-3439, 25th AIAA Aerodynamic Measurement Technology and Ground Testing Conference, San Francisco, California, 5 - 8 June, 2006

[74] Rung, T., Lübcke, H., Franke, M., Xue, L., Thiele, F., Fu, S., Assessment of Explicit Algebraic Stress Models in Transonic Flows, Proc. 4th Int. Symposium on Engineering Turbulence Modelling and Measurements, Corsica, France, pp 659-668, Elsevier, Amsterdam, 1999

[75] Sanderson, S.R., Simmons, J.M., Drag Balance for Hypervelocity Impulse Facilities, AIAA Journal, Vol. 29, No. 12, pp 2185-2191, 1991

[76] Sarkar, S., Erlebacher, G., Hussaini, M.Y., Kreiss, H.O., The Analysis and Modeling of Dilatational Terms in Compressible Turbulence, ICASE Report 89-79, NASA-Langley, 1989

[77] Schultz, D.L., Jones, T.V., Heat Transfer Measurements in Short Duration Facilities, AGARD Report 165, 1973

[78] Schwamborn, D., Homepage of the DLR Tau Code. URL: http://tau.dlr.de, German Aerospace Center, DLR, 2008

[79] Schwamborn, D., Gerhold, T., Heinrich, R., The DLR TAU Code: Recent Applications in Research and Industry. Proceedings of the European Conference on Computational Fluid Dynamics ECCOMAS CFD 2006, 2006

[80] Sheffer, S.G, Martinelli, L., Jameson, A., An Efficient Multigrid Algorithm for Compressible Reacting Flows. Journal of Computational Physics Vol. 144:484-516, 1998

[81] Skinner, G.T., A New Method of Calibrating Thin Film Gauge Backing Materials, Cornell Aeronautical Laboratory, Inc. of Cornell University, Buffalo, N.Y. 14221, Report No. CAL-105, 1962

[82] Smart, M.K., Hass, N.E., Paull, A., Flight data analysis of the HyShot 2 scramjet flight experiment, AIAA JOURNAL, Vol. 44, No.10, pp 2366-2375, 2006

[83] Spalart, P.R., Allmaras, S.R., A One-Equation Turbulence Model for Aerodynamic Flows. AIAA-Paper 92-0439, 1992

[84] Stalker, R.J., A Study of the Free-Piston Shock Tunnel, AIAA Journal, Vol. 5, No. 12, 1967

[85] Stalker, R.J., Hypervelocity Aerodynamics with Chemical Nonequilibrium, Ann. Rev. Fluid Mech., 21, 37-50, 1989

[86] Steelant, J., Achievements obtained for sustained hypersonic flight within the LAPCAT project, AIAA 2008-2578, 15th AIAA International Space Planes and Hypersonic Systems and Technologies Conference, Dayton, Ohio, USA, 2008

[87] Sudani, N., Valiferdowsi, B., Hornung, H.G., Test time increase by delaying driver gas contamination for reflected shock tunnels, AIAA 98-2771, 20th AIAA Advanced Measurement and Ground Testing Technology Conference, Albuquerque, NM ,June 15-18, 1998

[88] Toro, E.F., Riemann Solvers and Numerical Methods for Fluid Dynamics: A Practical Introduction. 2nd Edition, Springer, 1999

[89] Tropea, C., Yarin, A.L., Foss, J.F. (Eds.), Springer Handbook of Experimental Fluid Mechanics, Springer, 2007

[90] Turner, J., Hörschgen, M., Stamminger, P., and Turner, P., SHEFEX Hypersonic Reentry Flight Experiment, Vehicle and Subsystem Design, Flight Performances and Prospects, AIAA 2006-8115, 2006

[91] Vincenti, W.G., Krueger, C.H., Introduction to Physical Gas Dynamics, Krieger 1986

[92] Vreman, A.W. Sandham, N.D., Luo K.H., Compressible mixing layer growth rate and turbulence characteristics. Journal of Fluid Mechanics, Vol. 320, 1995

[93] Watson, S., MacPherson, W.N., Barton, J.S., Jones, J.D.C., Tyas, A., Pichugin, A.V., Hindle, A., Parkes, W., Dunare, C., Stevenson, T., Investigation of Shock Waves in Explosive Blasts Using Fibre Optic Pressure Sensors, Meas. Sci. Technol., 17, 1337-1342, 2006

[94] Wilcox, D.C., Turbulence Modelling for CFD. DCW Industries, La Canada, California, 1998

[95] Wilke, C.R., A Viscosity Equation for Gas Mixtures. Journal of Chemical Physics, Vol. 18(4), 1950

[96] Wollenhaupt, M., Rosenhauer, M., Müller, T., Jourdan, J., Scholz, J., Hartung, S., Beck, W.H., NO laser-induced fluorescence studies for the application of single-shot two-line thermometry to HEG, Proceedings of the 21st International Symposium on Shock Waves, Great Keppe1, Australia, 1997

[97] Zeman, O., Dilatation dissipation: The concept and application in modelling compressible mixing layers. Physics of Fluids A 2(2), 1990